THESIS FOR THE DEGREE OF LICENTIATE OF ENGINEERING

Transport in mesoscopic superconducting devices

KEVIN MARC SEJA

Department of Microtechnology and Nanoscience (MC2)
Applied Quantum Physics Laboratory
CHALMERS UNIVERSITY OF TECHNOLOGY

Göteborg, Sweden 2020

Transport in mesoscopic superconducting devices
KEVIN MARC SEJA

© KEVIN MARC SEJA, 2020

Thesis for the degree of Licentiate of Engineering
ISSN 1652-0769
Technical Report MC2-428

Applied Quantum Physics Laboratory
Department of Microtechnology and Nanoscience (MC2)
Chalmers University of Technology
SE-412 96 Göteborg
Sweden
Telephone: +46 (0)31-772 1000

Cover
Conversion of quasiparticle current into supercurrent in a N-S-N hybrid structure

Printed by Chalmers Reproservice
Göteborg, Sweden 2020

Transport in mesoscopic superconducting devices
Thesis for the degree of Licentiate of Engineering

KEVIN MARC SEJA

Department of Microtechnology and Nanoscience (MC2)
Applied Quantum Physics Laboratory
Chalmers University of Technology

Abstract

A field of growing interest within the last few decades is the study of superconductivity in mesoscopic-scale heterostructures. Mesoscopic refers to sizes between the atomic and macroscopic scales. Here, the size of heterostructures can be comparable to the inherent scale of superconductivity, the superconducting coherence length, and give rise to new physical phenomena.

The focus of this work is on mesoscopic hybrid structures consisting of superconducting, normal-metal, and magnetic regions. The combination of these different types of materials and the competition between interactions such as magnetism and superconductivity can then be used to design structures with novel effects. This is interesting from a fundamental point of view but equally relevant for technological applications. The magnet-superconductor hybrid structures examined in this work, for example, give rise spin-polarized Andreev bound states, a promising ingredient to superconducting spintronics.

We study transport in such hybrid systems under current bias to investigate the effects of such Andreev bound states on nonequilibrium properties. As part of this work, we develop a general calculation scheme for current-bias nonequilibrium within the quasiclassical theory of superconductivity. We use this scheme to study charge and spin imbalance in a normal-metal/superconductor structure with a spin-active interface. Our results show that transport in systems with spatially extended tunnel barriers is more accurately described by this current-bias picture compared to a voltage-bias description traditionally used in the theoretical literature for narrow constrictions. We find that the presence of Andreev bound states at a spin-active interface between normal-metal and superconducting regions strongly influence the charge as well as spin transport in such structures.

Keywords: superconductivity, quasiclassical theory, nonequilibrium superconductivity, mesoscopic physics, superconducting spintronics, Andreev bound states

List of figures

Contents

1 Introduction

This licenciate thesis discusses aspects of transport in mesoscopic hybrid structures consisting of normal metals and superconductors.

The word mesoscopic translates roughly to "middle-sized" and refers to a length scale between the nanometer scale of atoms and the macroscopic scale of bulk materials. In a more rigorous definition, at least one dimension d of a mesoscopic condensed-matter system is large compared to the Fermi wavelength λ_F of the given material, typically ten to one hundred nanometers, but smaller than the so-called phase coherence length l_ϕ of several hundred nanometers at sub-Kelvin temperatures.[1]

In this intermediate regime systems can be described in terms of individual particles that still exhibit quantum-mechanical interference effects. Such effects are both a curse and a blessing for technology development. One the one hand, they impose a natural limit to the size reduction of existing electronic devices, such as field-effect transistors[2]. On the other hand, they can be used to develop new electronic devices that do not have an analogue in classical physics.

The focus of this work is on mesoscopic systems involving superconductivity, a low-temperature phase of matter that allows for dissipationsless charge tranport. Sect. 1.1 gives a brief of review of superconductors and their theoretical description. The natural lengthscale of a superconductor, the superconducting coherence length, is in the mesoscopic regime, ranging from tens to hundreds of nanometers. Pieces of superconducting material are thus ideal building blocks in mesoscopic devices and often used in, e.g., nanoscale Josephson junctions or SQUIDS[3].

In recent years, the combination of superconductors with materials exhibiting competing interactions has been the topic of extensive research. Magnet-superconductor hybrids in particular have been predicted to provide a way to "quantum engineer" a superconductor featuring spin-polarized triplet pairs. These are of key importance to superconducting spintronics[4]. The latter aims to build disspationless logic devices based on spin transport rather than charge transport. Such magnet-superconductor hybrid structures are also expected to provide key ingredients to ultrafast, superconducting high-performance computers based on rapid single-flux quantum (RSFQ) technology[24]. We refer to the discussion in Sect. 1.2 for further details.

Any application of superconducting hybrid structures in electronics, however, requires understanding of their nonequilibrium behaviour. The aim of this work is to provide a framework within the so-called quasiclassical theory to describe

such systems in current-biased nonequilibrium. We then use this scheme to analyze a hybrid structure consisting of normal-metal and superconducting regions, connected via either an insulating barrier or a spin-active interface. Lastly, we compare the results of our approach to existing descriptions in terms of a potential bias, as further explained in Sect. 1.3.

1.1 Superconductivity

For slightly more than a century, superconductivity has been one of the most intriguing and rich phenomenon in condensed matter physics. The term, meaning that a material is "more than (just) conducting", is now used as an umbrella term for a new phase of matter with a multitude of connected physical phenomena.

In a nutshell, superconductivity refers to a phase of matter for solids, typically metals or ceramics, with unique electro-magnetic and thermodynamic properties. The phase transition to this new phase typically occurs below the so-called critical temperature $T_c \lesssim 10$ K, sometimes in combination with very high pressures on the order of a GPa.

Historically, the first discovery of a material becoming superconducting was reported by Heike Kamerlingh Onnes in 1911[5]. He received the Nobel Prize in Physics already two years later, both for this discovery and for being the first to successfully liquify helium[6]. Using liquid helium allowed him to cool down metals to temperatures of less than 4.2 K that were unattainably low before. Kamerlingh Onnes used this to investigate the electrical conductivity of metals, in his case mercury, to answer the question of how the conductivity would behave at such low temperatures. At the time, two different and incompatible hypotheses existed: Either the conductivity should first reach a maximum and then decrease to zero for $T \to 0$, since the electrons would "freeze" in place, or the conductivity should rapidly increase to infinity. His experimental results indicated the latter case, meaning that all resistivity vanished in the material. This was the birth of the field of superconductivity.

Kammerlingh Onnes' surprising discovery was followed by intense experimental research on the new physical phenomenon. This lead to the discovery of the Meissner effect: Not only are superconductors perfect conductors, they are also perfect diamagnets, i.e., they expel an applied magnetic field from their interior[7]. More specifically, the magnetic field only penetrates the superconductor on the scale of the so-called penetration depth λ. About two decades after Kamerlingh Onnes' original discovery, Fritz and Heinz London described this magnetic behaviour in their famous equations[8]. However, it would take another 20 years until a consistent theoretical explanation for the phenomenon was developed. In 1957, John **B**ardeen, Leon **C**ooper, and John Robert **S**chrieffer formulated the first coherent, microscopic theory of superconductivity[9, 10] that today is referred to as BCS theory. For this achievement, they obtained the Nobel Prize in Physics in 1972

[11].

In 1986, another ground-breaking discovery was made when Bednorz and Müller discovered that a ceramic compound consisting of barium, lithium, copper and oxygen ("Ba-Li-Cu-O") also became superconducting, even at temperatures that were substantially higher than what was known from the pure-metal superconductors[12]. They received the Nobel prize in physics in the next year for their discovery of what is accordingly referred to as high-temperature or high-T_c superconductors[13]. Other, similiar materials with even higher critical temperatures on the order of 100 K have been found, which led to, currently still ongoing, research to find a material that is a superconductor even at room temperature.

1.1.1 The BCS theory

This short summary is based on[14], where more details can be found. In terms of quantum-mechanical field operators, the BCS theory uses a minimal Hamiltonian of the form

$$\mathcal{H}_{\text{BCS}} = \sum_{\mathbf{k},\sigma} \xi_{\mathbf{k}} c^{\dagger}_{\mathbf{k},\sigma} c_{\mathbf{k},\sigma} + \sum_{\mathbf{k},\mathbf{k}'} V_{\mathbf{k},\mathbf{k}'} c^{\dagger}_{\mathbf{k},\uparrow} c^{\dagger}_{-\mathbf{k},\downarrow} c_{-\mathbf{k}',\downarrow} c_{\mathbf{k}',\uparrow} \tag{1.1}$$

where $\sigma = \uparrow, \downarrow$ is a spin index and $\xi_{\mathbf{k}}$ is the electronic dispersion relative to the chemical potential, in the simplest model given by

$$\xi_{\mathbf{k}} = \frac{\mathbf{k}^2}{2m} - \mu. \tag{1.2}$$

The second term in Eq. (1.1), describing an electron-electron interaction, is constructed such that the interaction is between electrons of opposite spin and momentum.

In contrast to the purely repulsive Coulomb interaction between electrons, $V_{\mathbf{k},\mathbf{k}'}$ is assumed to be *attractive* interaction below a certain energy scale E_{BCS}. Fröhlich[15] studied electron-phonon interactions at low temperatures and showed that it gives rise to an effectively attractive electron-electron interaction that can overcome the Coulomb interaction for electrons with opposite momentum. The physical picture here is that a travelling electron will "push" some ions in the crystal lattice out of their equilibrium positions by Coulomb attraction. This dislocation of the ion — a quantum-mechanical phonon — will then in turn attract another electron, giving rise to the indirect interaction between the two electrons.

In 1956, Cooper then showed that the Fermi gas becomes unstable below a certain critical temperature T_c as a result of this attractive interaction, a phenomenon referred to as Cooper instability[16], and the system undergoes a phase transition to the superconducting state. The BCS theory then describes this new state of matter: The groundstate consists of a condensate of dynamic electron-pair states, the Cooper pairs, which have a typical spatial extension of ξ_0, the so-called coherence length. To gain further insight into the BCS Hamiltonian in Eq. (1.1), we

diagonalize it by performing a mean-field approximation on the bilinear terms and using a a Boguljubov transformation,

$$\gamma_{\mathbf{k},0} \equiv u_{\mathbf{k}} c_{\mathbf{k}\uparrow} - v_{\mathbf{k}} c^{\dagger}_{\mathbf{k}\downarrow}, \qquad \gamma^{\dagger}_{\mathbf{k},1} \equiv v^{*}_{\mathbf{k}} c_{\mathbf{k}\uparrow} + u^{*}_{\mathbf{k}} c^{\dagger}_{\mathbf{k}\downarrow}, \tag{1.3}$$

which replaces c and $c^{\dagger}$ with the creation and annihilation operators of new quasiparticles, namely those that exist in a superconductor. As can be seen from the definition, these new quasiparticles are coherent superpositions of particles and holes, and the weights $u_{\mathbf{k}}$ and $v_{\mathbf{k}}$ are chosen such that $|u_{\mathbf{k}}|^2 + |v_{\mathbf{k}}|^2 = 1$. Using the definition

$$\Delta_{\mathbf{k}} = \sum_{\mathbf{k}'} V_{\mathbf{k}\mathbf{k}'} \langle c_{-\mathbf{k}'\downarrow} c_{\mathbf{k}'\uparrow} \rangle, \tag{1.4}$$

the diagonalized Hamiltonian then reads

$$\mathcal{H}_{\mathrm{BCS}} \approx \sum_{\mathbf{k}} \left(\varepsilon_{\mathbf{k}} - E_{\mathbf{k}} \ + \Delta_{\mathbf{k}} \langle c^{\dagger}_{\mathbf{k}\uparrow} c^{\dagger}_{-\mathbf{k}\downarrow} \rangle \right) + \sum_{\mathbf{k}} E_{\mathbf{k}} \left(\gamma^{\dagger}_{\mathbf{k},0} \gamma_{\mathbf{k},0} + \gamma^{\dagger}_{\mathbf{k},1} \gamma_{\mathbf{k},1} \right). \tag{1.5}$$

The first term is the superconducting ground-state energy, which has to be lower than the normal-state ground state energy, while the latter is the energy of the quasiparticle excitations in the superconductor, given by

$$E_{\mathbf{k}} \equiv \sqrt{\xi^2_{\mathbf{k}} + |\Delta_{\mathbf{k}}|^2}. \tag{1.6}$$

There is thus a minimal energy $\Delta_{\mathbf{k}}$ required for any excitation above the ground state. This ground state is, in turn, given by the wave function

$$|\psi_{BCS}\rangle = \prod_{\mathbf{k}} \left(u_{\mathbf{k}} + v_{\mathbf{k}} c^{\dagger}_{\mathbf{k},\uparrow} c^{\dagger}_{-\mathbf{k},\downarrow} \right) |\phi_0\rangle, \tag{1.7}$$

where $|\phi_0\rangle$ is the vaccum, describing a coherent superposition of Cooper pairs.

The vanishing resistance in a superconductor can then be explained by the fact that the condensate of Cooper pairs is not sensitive to scattering since single-particle excitations cost too much energy. Differently put, the energy scale of the scattering is less than the minimal excitation energy in Eq. (1.6). Thus, non-magnetic impurities do not affect the thermodynamics of the equilibrium superconducting state as long as the impurity concentration is not so large that the metal becomes insulating above the critical temperature T_c. Impurities can, however, affect transport in superconductors.

The resulting stability of the Cooper pairs against scattering means that the charge carriers can move through the superconductor essentially unhindered, giving rise to perfect conductance.

1.2 Superconducting spintronics

Spintronics, as a field of technology and research, aims to build integrated circuits that rely on manipulating electrons via their *spin* — compared to electronics, where effects based on electron *charge* are being used. One illustrative example for a spintronice device is the so-called spin transistor, originally proposed in [17]. In an electronic transistor, a controllable gate voltage adjusts the current flow from a source electrode to a drain electrode. In contrast, the spin transistor allows or disallows flow of electrons based on the orientation of their spin relative to ferromagnetic source and drain leads. In comparison to a normal transistor, the two source and drain leads are replaced with ferromagnetic electrodes. As a result, only electrons with a certain spin orientation will enter from the left (source) lead. The central region consist a two-dimensional electron gas (2DEG) with a gate-voltage dependent spin-orbit coupling. A simplified illustration of the working principle can be seen in Fig. 1.1.

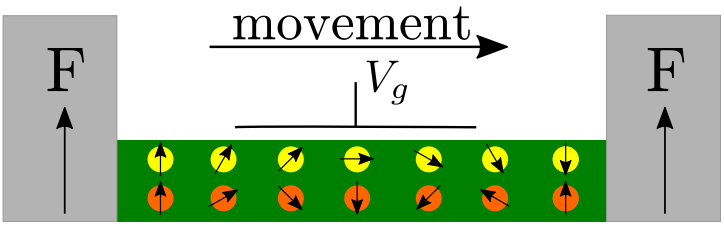

Figure 1.1: *Working principle of a spin transistor, based on Ref.[17]. Depending on the gate-voltage dependent spin-orbit coupling in the central (green) 2DEG, the final spin orientation will be parallel or antiparallel to the right-hand magnetization, allowing or disallowing transport.*

While moving in the 2DEG, the spin-orbit coupling causes a rotation of the electron spin and the final spin orientation upon reaching the right drain lead will be determined by the gate voltage. Dependening on the relative spin orientation, the transport into the ferromagnetic drain will thus be blocked for antiparallel orientation (yellow electrons) or allowed for parallel orientation (orange electrons).

The main idea of spintronics is thus that, in one way or another, the electron spin is used in a controlled manner to affect electronic transport properties through a structure. Superconducting spintronics now seeks to use the same principle in circuits with superconducting currents.

At first glance, that might seem surprising: As discussed in Sect. 1.1, most (conventional) superconductors have a singlet spin structure, meaning that the current-carrying Cooper pairs do not have a net spin component. As an effect of that, simply using ferromagnetic leads or regions, as in the conventional spin transistor, will not work since ferromagnetism will destory the singlet Cooper pairs. As an example, we can consider a "ferromagnetic" Josephson junction, or SFS system, as seen in Fig. 1.2. In a regular Josephon junction, where the central

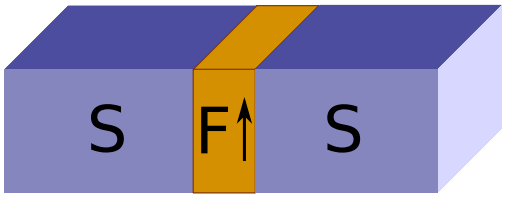

Figure 1.2: *A ferromagnetic Josephson junction.*

region (F in Fig. 1.2) is a normal metal or insulator, the Cooper pairs from the two superconductors can tunnel through the barrier. This gives rise to the dc Josephon effect — the current flow through the barrier, and hence the entire system, will depend on the phase difference in the two superconductors[18]. This is possible since the Cooper pairs can coherently tunnel through the thin, central barrier, as their pair amplitude only slowly decays.

In a ferromagnetic central region, this decay happens on a very short lengthscale since the two spin orientations effectively "feel" different energy landscapes, leading to decoherence. However, this would not be the case if we had *spin-triplet* "Cooper pairs" in one of the two spin-polarized triplet states, $|\uparrow\uparrow\rangle$ or $|\downarrow\downarrow\rangle$. For these equal-spin pairs, there is no pair-breaking effect in the magnetic region since the two electrons constituting a pair have the same spin orientation, allowing the triplet pairs to cross through the ferromagnetic central region[4] .

In 2005, it was suggested that these triplet pairs can be created by combining conventional, s-wave superconductors with so-called "spin-active", magnetic interfaces[19]. In essence, the spin-active interface can transform singlet Cooper pairs into unpolarized triplet pairs, which can subsequently be spin-rotated into polarized triplet pairs[4]. Experimental results are in agreement with this and further theoretical predictions such as the presence of spin-polarized Andreev bound states at the interface of a magnet-superconductor hybrid structure[20].

Returning to the SFS system, once we have supercurrent carried by polarized triplet pairs, it is possible to switch the supercurrent through the ferromagnetic barrier on and off, depending on the relative magnetization in the F layer with respect to the spin orientation of the triplet pairs. This has indeed been experimentally shown, e.g., in Refs. [21, 22], and the main idea and results of the latter paper can be seen in Fig. 1.3.

In short, an unmagnetized, superconducting nickel layer (blue) is separated by copper layers (orange) from a NiFe layer (green). The magnetization in the latter can be switched by relative small magnetic fields, while the copper layers require large fields to change the magnetization. Depending on the magnetization of the top NiFe layer relative to the spin-triplet orientation, the supercurrent is either allowed or blocked from passing through the central, magnetic region (compare Fig. 1.2). As can be seen in Fig. 1.3b, the supercurrent can be controllably turned off if a field perpendicular to the spin-triplet orientation is applied, and turned on

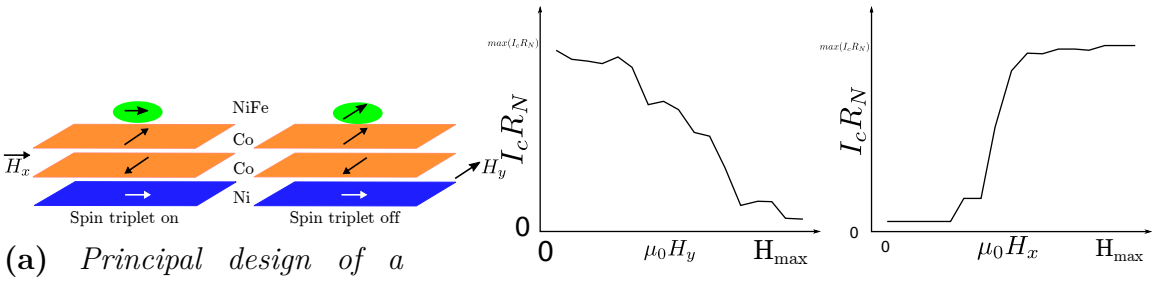

(a) *Principal design of a switchable spin-triplet Josephson junction. Sketch based on Fig. 1 from Ref. [22].*

(b) *Sketch of experimental results for a switchable spin-triplet Josephson junction. Sketch based on Fig. 2 from Ref. [22].*

Figure 1.3: *Design and experimental results for a proof-of-principle spin-triplet Josephson junction.*

again once a parallel orientation is applied.

On one hand, this result is interesting from a fundamental point of view, since it shows that spin-triplet supercurrents can be used to obtain a transport behaviour in hybrid structures that is fundamentally different from conventional spin-singlet currents. The effect is also of interest for technological applications, most importantly in the development of Rapid Single-Flux Quantum (RSFQ) technology. In a nutshell, RSFQ uses superconducting circuits based on Josephson junctions, which are sensitive to changes in the magnetic flux on the scale of the magnetic flux quantum, to build "superconducting transistors".

In contrast to semiconductor transistors, where the logical value 0 and 1 are represented by the presence or absence of current flow, the RFSQ technology uses the absence or presence of magnetic flux quanta, and uses flux changes to perform logical operations. The main advantage is that these flux quanta can be changed on a much shorter timescale than current flow in electronic transistors, allowing for operation speeds on the scale of several hundred gigahertz[23–25].

While the functionality of this type of technology has been proven, it still lacks a key ingredient, namely a "superconducting memory", and this is exactly what the magnetic Josephson junctions discussed above can be used for: Supercurrent flow is either allowed or blocked depending on the magnetization in a persistent control layer, mapping to a logical 0 or 1. Indeed, magnetic Josephson memory cells have been build using similiar physics in so-called switchable π-junctions[26, 27].

The main motivation for this work is, thus, that while some proof-of-principle experiments have been performed, there are still a many unanswered questions. Firstly, there is a lot of only partially understood physics in magnet-superconductor hybrid systems, especially in nonequilibrium situations, for example spin-charge separation[20] or Andreev bound states. Secondly, a deeper understanding is needed to optimize such hybrid systems for practical applications. Our aim is thus to develop tools to study such hybrid systems, which will hopefully allow for a better understanding of the physics involved.

1.3 Mesoscopic superconductors in nonequilibrium

As discussed in Sect. 1.1, one of the main features of a superconductor is the dissipationsless charge transport. For many applications it is thus crucial to understand the properties of superconductors in nonequilibrium where such transport is possible. One common approach, along the lines of the seminal paper [28] by Blonder, Tinkham, and Klapwijk that studied superconducting microconstrictions, is to describe this nonequilibrium in terms of a voltage bias at an interface between a normal metal and a superconductor. We will discuss this approach, that we we refer to as BTK approach in the following, in more detail in Sect. 3.2. In spirit, it is similiar to assuming a Sharvin contact[29], as depicted in Fig. 1.4.

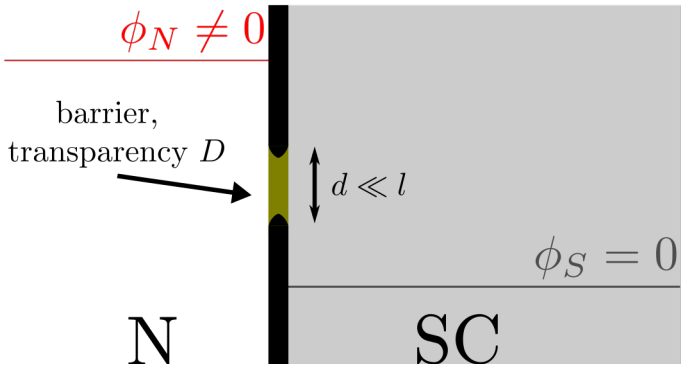

Figure 1.4: *Sketch of a Sharvin contact: Only a contact of size d much smaller than the electron mean free path l is open for particle transmission with probability D. Directly at the contact, the potential drops from the normal-metal "reservoir" value ϕ_N to potential ϕ_S of the (grounded) superconductor.*

A key point of this assumption is then that the potential drops only directly at the interface between the normal metal and superconductor. Part of this work is thus to examine the validity of this assumption in the case of spatially extended interfaces rather than a point contact as described above.

For experimental setups a description in terms of a current bias rather than a voltage bias is also often more appropriate, see also the discussion in Chapter 2 of [14]. We thus develop a current-bias calculation scheme for the quasiclassical theory, discussed in Chap. 2, and compare it to a voltage-bias description in Chap. 3 and 4.

1.4 Organization of this thesis

The remainder of this thesis consists of three chapters. In Chapter 2, we discuss the quasiclassical theory of superconductivity, the main tool used in this thesis. We will discuss the framework of Green's functions in general and their connection to the quasiclassical theory in Sect 2.1. This theory is to be used to per-

form spin-dependent, stationary transport calculations for superconducting hybrid structures. A large part of this work was thus to combine, and partially extend, different parts of this theory. In Sect. 2.2 we discuss the treatment of general, spin-dependent boundary within quasiclassics. Sect. 2.3 is devoted to the operator technique as a way to solve the quasiclassical equations of motion for both spectral functions and distribution functions. Lastly, a description of how to combine all these different elements into a fully self-consistent nonequilbrium calculation, including boundary values in nonequilbrium, is presented in Sect. 2.4.
Following this discussion of mathematical and technical aspects of quasiclassical theory, we present results for both an entirely normal-metal system, henceforth referred to as NIN system, and hybrid systems of normal-metals and superconductors, or NIS system. In Chapter 3, we study spin-degenerate charge transport in these two systems, with a focus on charge imbalance in the superconducting system. We also compare our current-bias approach to the BTK-type potential bias description. In Chapter 4, we study the effects of spin-active interface on transport by considering both charge and spin currents as well as the resulting magnetization in both types of systems.

2 Quasiclassical theory of superconductivity

The main tool used in this thesis to investigate magnet-superconductor hybrid structures is the so-called *quasiclassical theory*, an approach that is based on Green's functions. The Green's function technique is both extremely powerful and widely used in many-body condensed-matter physics. We will only review the fundamental concepts here but refer to the pedagogical presentation in Chapters 8-11 of [30] for further details. A discussion more focused on the connection between Green's functions and quasiclassical theory can be found in [31].

2.1 Green's functions & Gor'kov equation

Assume that we have a many-body system described by a Hamiltonian $\mathcal{H}$. In principle, we could solve the full Schrödinger equation for Ψ and then calculate any desired observables. However, many-body systems typically have untractably many degrees of freedom which prohibit such a complete solution. The Green's function technique circumvents this problem by constructing auxiliary mathematical objects — the Green's functions — that contain less information, while still allowing for the calculation of any desired observable[32].
A possible starting point of the theory, following [33, 34], are the retarded, advanced, and Keldysh single-particle Green's functions, for fermions defined as

$$G^R_{\sigma,\sigma'}(\vec{r}t;\vec{r}\,'t') \equiv -i\theta(t-t')\left\langle\left[\Psi_\sigma(\vec{r},t),\Psi^\dagger_{\sigma'}(\vec{r}\,',t')\right]\right\rangle, \tag{2.1}$$

$$G^A_{\sigma,\sigma'}(\vec{r}t;\vec{r}\,'t') \equiv \;\; i\theta(t'-t)\left\langle\left[\Psi_\sigma(\vec{r},t),\Psi^\dagger_{\sigma'}(\vec{r}\,',t')\right]\right\rangle. \tag{2.2}$$

$$G^K_{\sigma,\sigma'}(\vec{r}t;\vec{r}\,'t') \equiv \; -i\left\langle\left[\Psi_\sigma(\vec{r},t),\Psi^\dagger_{\sigma'}(\vec{r}\,',t')\right]\right\rangle. \tag{2.3}$$

Here, $\Psi(\vec{r},t)$ and $\Psi^\dagger(\vec{r},t)$ are the quantum-mechanical field operators in the Heisenberg picture, e.g.,

$$\Psi(\vec{r},t) \equiv e^{-i\mathcal{H}t}\psi(\vec{r})e^{i\mathcal{H}t}, \tag{2.4}$$

and the brackets indicate a statistical average, in equilbrium for finite temperature

$$\langle\hat{A}\rangle \equiv \frac{\mathrm{Tr}\; e^{-\beta\mathcal{H}}A}{\mathrm{Tr}\; e^{-\beta\mathcal{H}}}, \tag{2.5}$$

where $\beta = 1/k_BT$.

The physical interpretation for the quantities in Eqs. (2.1) and (2.2) is the probability of finding a single particle with spin σ', inserted into the system at time t' at position $\vec{r}'$, at the position $\vec{r}$ at time t with spin σ. From the above definitions, we see that for the retarded function we have $t > t'$, while for the advanced $t' > t$ holds. Hence, the functions describe forward-in-time (retarded) and backward-in-time (advanced) propagation of a particle. The last quantity, G^K in Eq. (2.3), does not contain propagation propabilities but rather the propagation of the occupation of a given particle state. Although the above functions are referred to as "single-particle" objects, the time evolution for $\Psi(\vec{r}, t)$ and hence $G^{R,A,K}$ is determined by the full Hamiltonian, including all many-body effects.

Once we have calculated the single-particle Green's functions, we can calculate any single-particle observables. As an example, the charge current is determined by an energy integral of the so-called current density, which can be written as

$$\vec{j}(\varepsilon) \equiv -\frac{e}{2m}\left(\vec{\nabla}_{\vec{r}} - \vec{\nabla}_{\vec{r}\,'}\right)\left[G^K(\vec{r};\vec{r}\,') - \left(G^R(\vec{r};\vec{r}\,') - G^A(\vec{r};\vec{r}\,')\right)\right]\Big|_{\vec{r}=\vec{r}'}, \qquad (2.6)$$

see also [34]. We note here that the single-particle functions can also be used as "buiding blocks" to construct many-body Green's functions, for example by the equation-of-motion technique [30].
When used in equilibrium, the time argument t in Eqs. (2.1) - (2.4) can be moved to the imaginary axis by the transformation $t = -i\tau$, which turns the unitary time evolution into a Boltzmann-like statistical weight[32].
The equilibrium, imaginary-time Green's functions is then given by

$$G_{\sigma,\sigma'}(\vec{r}\tau;\vec{r}\,'\tau') \equiv -\left\langle \mathcal{T}_\tau \Psi_\sigma(\vec{r},\tau), \Psi^\dagger_{\sigma'}(\vec{r}\,',\tau')\right\rangle, \qquad (2.7)$$

where $\mathcal{T}_\tau$ is the "time"-ordering operator. As mentioned in Sect. 1.1, the excitations in a superconductor are no longer electrons or holes, as they would be in a normal metal, but rather mixtures of the two. Hence, in the theory of superconductivity we have two additional Green's functions, also referred to as anomalous Green's functions or Gor'kov functions. Analogously to Eq. (2.7), they are defined as

$$F^\dagger_{\sigma\sigma'}(\vec{r}\tau;\vec{r}\,'\tau') \equiv \left\langle \mathcal{T}_\tau \Psi^\dagger_\sigma(\vec{r},\tau), \Psi^\dagger_{\sigma'}(\vec{r}\,',\tau')\right\rangle, \qquad (2.8)$$

$$F_{\sigma\sigma'}(\vec{r}\tau;\vec{r}\,'\tau') \equiv \left\langle \mathcal{T}_\tau \Psi_\sigma(\vec{r},\tau), \Psi_{\sigma'}(\vec{r}\,',\tau')\right\rangle. \qquad (2.9)$$

The label "anomalous" refers to the fact that they can only be nonzero if the particle number is not conserved. Physically, they describe the propagation of an inserted Cooper pair, similiar to the electron propagation discussed earlier. The two functions F and $F^\dagger$ are therefore also referred to as superconducting correlations. In fact, from the additional definition

$$\Delta_{\sigma\sigma'}(\vec{r}) \equiv |\lambda| F_{\sigma\sigma'}(\vec{r},\vec{r}), \qquad (2.10)$$

we see that the existence of superconducting order parameter Δ is equivalent to the presence of these superconducting correlations. One can now define a Nambu (particle-hole) space matrix $\check{G}$ as

$$\check{G}(\vec{r}\tau;\vec{r}\,'\tau') \equiv \begin{pmatrix} G(\vec{r}\tau;\vec{r}\,'\tau') & F(\vec{r}\tau;\vec{r}\,'\tau') \\ -F^{\dagger}(\vec{r}\tau;\vec{r}\,'\tau') & \overline{G}(\vec{r}\tau;\vec{r}\,'\tau') \end{pmatrix}, \tag{2.11}$$

where $\overline{G}$ refers to the particle-hole conjugate of G. For this matrix, one can derive an equation of motion, the so-called Gor'kov equation[35], which reads

$$\left(\check{\tau}_3\frac{\partial}{\partial\tau} + \check{\mathcal{H}}\right)\check{G}(\vec{r}\tau;\vec{r}\,'\tau') = \check{1}\delta(\vec{r}-\vec{r}')\delta(\tau-\tau'), \tag{2.12}$$

where

$$\check{\mathcal{H}} = \begin{pmatrix} -\frac{\nabla^2}{2m} - \mu & -\Delta \\ -\Delta^* & -\frac{\nabla^2}{2m} - \mu \end{pmatrix}, \tag{2.13}$$

and $\check{\tau}_3$ is the Pauli z-matrix in Nambu space. In principle, one could solve the Gor'kov equation to obtain the full Green's function for the superconductor and then calculate any observable. Often, however, the full Gor'kov Green's functions still contain information on a too small length scale and calculations can be simplified by the so-called quasiclassical approximation.

2.1.1 Quasiclassical Green's functions

The quasiclassical theory was first introduced in [36] and, independently, in [37]. We follow the presentation in [31]. At the core of the theory lies an expansion in a small parameter, in this case it is assumed that

$$\frac{\Delta}{E_F} \ll 1. \tag{2.14}$$

For conventional superconductors, this ratio is on the order of 10^{-3}. Equivalently, one assumes that excitations relevant for superconductivity have their momentum in a small shell around the Fermi surface. Physical observables, such as the charge current in Eq. (2.6), involve taking the limit of $\vec{r} \to \vec{r}\,'$ after differentiation in real space representation, corresponding to momentum integration in momentum-space representation. The quasiclassical approximation then consists in replacing such momentum integrations in the spirit of

$$\frac{d^3p}{(2\pi\hbar)^3} \approx d\xi_p \frac{d\Omega_{\vec{p}}}{(2\pi\hbar)^3 v_F}, \tag{2.15}$$

where ξ_p is the dispersion relation in the normal state and v_F is the Fermi velocity. The quasiclassical Green's functions are then obtained by integrating the full Green's function G over ξ_p,

$$g(\hat{p}) \equiv \int \frac{d\xi_p}{\pi i} G(\vec{p}), \tag{2.16}$$

such that the resulting function g only depends on the *orientation* of the momentum vector on the Fermi sphere, $\hat{p}$, while the magnitude of the momentum is assumed to be equal to the Fermi momentum p_F. In an analogous way, one defines the quasiclassical anomalous function $f(\hat{p})$. In comparison to the full Green's functions G and F, the quasiclassical functions lose information about processes on the atomic scale. For most superconductors, however, the condition in Eq. (2.14) means that the relevant physics happens on a larger scale, namely the scale of the superconducting coherence length

$$\xi_0 \equiv \frac{\hbar v_F}{2\pi k_B T_c}, \tag{2.17}$$

which, as discussed earlier, is the natural lengthscale of superconducting phenomena. Similiar to before, we can group the different quasiclassical functions in a matrix in Nambu space,

$$\check{g} = \begin{pmatrix} g & f \\ -\tilde{f} & \tilde{g} \end{pmatrix}. \tag{2.18}$$

While the full Green's function $\hat{G}$ can be obtained by solving the Gor'kov equation, Eq. (2.12), the quasiclassical function $\check{g}$ is the solution to a different differential equation, the so-called Eilenberger equation.

2.1.2 Eilenberger equation

The Eilenberger equation[36] reads

$$i\hbar\vec{v}_F\vec{\nabla}\check{g} + \left[\varepsilon\hat{\tau}_3\check{1} - \check{h}, \check{g}\right]_\circ = \check{0}, \tag{2.19}$$

which was derived using the so-called left-right trick for the original equation. Eq. (2.19) can have spurios solutions, which is cured by the normalization condition

$$\check{g} \circ \check{g} = -\pi^2\check{1}. \tag{2.20}$$

The $\circ$ denotes a time-convolution product, which is discussed in more detail in, e.g., [38]. Since we will only deal with stationary, time-independent problems in the following text, all dot products simplify to matrix multiplications and we omit the dot symbol. Note that $\check{g}$ and $\check{h}$ are matrices in Nambu-Keldysh space (denoted

by ˇ) with elements in particle-hole space (denoted by ˆ) and spin space (matrices without a ˇ or ˆ). The Nambu-Keldysh matrices $\check{g}$ and $\check{h}$ are given by

$$\check{g} = \begin{pmatrix} \hat{g}^R & \hat{g}^K \\ 0 & \hat{g}^A \end{pmatrix}, \qquad \check{h} = \begin{pmatrix} \hat{h}^R & \hat{h}^K \\ 0 & \hat{h}^A \end{pmatrix}. \tag{2.21}$$

The matrices $\hat{h}^X$ contain all self energies,

$$\hat{h}^{R,A} = \begin{pmatrix} \Sigma & \Delta \\ \tilde{\Delta} & \tilde{\Sigma} \end{pmatrix}^{R,A} \qquad \hat{h}^K = \begin{pmatrix} \Sigma & \Delta \\ -\tilde{\Delta} & -\tilde{\Sigma} \end{pmatrix}^K, \tag{2.22}$$

and the quasiclassical Green's function $\check{g}$ has the elements

$$\hat{g}^{R,A} = \mp 2\pi i \begin{pmatrix} \mathcal{G} & \mathcal{F} \\ -\tilde{\mathcal{F}} & -\tilde{\mathcal{G}} \end{pmatrix}^{R,A} \pm i\pi\hat{\tau}_3 1, \tag{2.23}$$

$$\hat{g}^K = -2\pi i \begin{pmatrix} \mathcal{X} & \mathcal{Y} \\ \tilde{\mathcal{Y}} & \tilde{\mathcal{X}} \end{pmatrix}^K = \begin{pmatrix} g & f \\ -\tilde{f} & -\tilde{g} \end{pmatrix}^K. \tag{2.24}$$

Note that the latter parametrization of $\hat{g}^K$ is a matter of convention — the one using $\mathcal{X}$ and $\mathcal{Y}$ follows [38], while the one using g and f is commonly found in the literature, e.g., in [39, 40]. In principle, the Eilenberger equation could be solved directly. In most cases, however, a different scheme has proven to be more successful and is thus commonly used, the so-called Ricatti parametrization.

2.1.3 Ricatti parametrization & distribution function x

The Ricatti parametrization uses a projector technique to specify the elements of the quasiclassical Green's function in terms of so-called Ricatti amplitudes or *coherence functions*. Explicitly, the form

$$\mathcal{G}^X \equiv \left(\mathbb{1} - \gamma^X\tilde{\gamma}^X\right)^{-1}, \qquad \mathcal{F}^X = \left(\mathbb{1} - \gamma^X\tilde{\gamma}^X\right)^{-1}\gamma^X, \tag{2.25}$$

where $X = R, A$, is used. Here, $\mathbb{1}$ is the unit matrix in spin space and both γ and $\tilde{\gamma}$ are spin matrices. One can then use the Eilenberger equation to derive the so-called Ricatti equations for γ and $\tilde{\gamma}$, namely

$$i\hbar\vec{v}_F\vec{\nabla}\gamma^{R,A} = \left(\gamma\tilde{\Delta}\gamma - 2\varepsilon\gamma + \Sigma\gamma - \gamma\tilde{\Sigma} - \Delta\right)^{R,A}, \tag{2.26}$$

$$i\hbar\vec{v}_F\vec{\nabla}\tilde{\gamma}^{R,A} = \left(\tilde{\gamma}\Delta\tilde{\gamma} + 2\varepsilon\tilde{\gamma} + \tilde{\Sigma}\tilde{\gamma} - \tilde{\gamma}\Sigma - \tilde{\Delta}\right)^{R,A}. \tag{2.27}$$

The two differential equations are always solved along trajectories, specified by the Fermi-velocity direction $\vec{v}_F$. However, only certain integration directions produce normalizable solutions in the sense of Eq. (2.20). For the retarded functions, γ has

to be integrated in the direction of $\vec{v}_F$ while $\tilde{\gamma}$ has to be integrated in the direction opposite to the Fermi velocity. For the advanced quantities, the integration directions are swapped. In the bulk of an s-wave superconductor, we can solve Eqs. (2.26) - (2.27) analytically. One finds, for the retarded functions,

$$\gamma^R_{\text{bulk}} = \gamma^R_0 i\sigma_2 = \frac{-\Delta^R}{\mathcal{E}^R + i\sqrt{-\Delta^R\tilde{\Delta}^R - (\mathcal{E}^R)^2}} i\sigma_2, \tag{2.28}$$

$$\tilde{\gamma}^R_{\text{bulk}} = \tilde{\gamma}^R_0 i\sigma_2 = \frac{\tilde{\Delta}^R}{\mathcal{E}^R + i\sqrt{-\Delta^R\tilde{\Delta}^R - (\mathcal{E}^R)^2}} i\sigma_2, \tag{2.29}$$

where Δ is the off-diagonal, spin-matrix self-energy in Eq. (2.22), and

$$\mathcal{E}^X \equiv \varepsilon - \frac{\Sigma^X - \tilde{\Sigma}^X}{2}. \tag{2.30}$$

Eqs. (2.26) - (2.27) have the form of a specific diffential equation, the name-giving (mathematical) Ricatti equation. One useful property of this equation is that once we have *one* particular solution γ_p, we can obtain the general solution analytically. In the case of γ^R, chosing γ^R_{bulk} as the particular solution, one can show, see for example Ref. [41], that the general solution is given by

$$\gamma^R(\rho) = \gamma^R_{\text{bulk}} + \frac{2i\Omega^R C e^{-2\Omega^R\rho}}{1 - \tilde{\Delta}^R C e^{-2\Omega^R\rho}}, \tag{2.31}$$

where $\Omega^R \equiv \sqrt{|\Delta^R|^2 - (\mathcal{E}^R)^2}$, ρ parametrizes a trajectory as $\vec{r} = \vec{r}_0 + \rho\vec{v}_F$, and

$$C = \frac{\gamma^R(\rho=0) - \gamma^R_{\text{bulk}}}{2i\Omega^R + \tilde{\Delta^R}\left(\gamma^R(\rho=0) - \gamma^R_{\text{bulk}}\right)}. \tag{2.32}$$

Similiar formulas can be obtained for the $\tilde{\gamma}^R$ and the advanced quantities. We will, however, use a sligthly different method based on operators, discussed in Sect. 2.3.1.

For the Keldysh Green's function, $\hat{g}^K$, a parametrization in terms of a distribution function is used. There is a certain freedom in what function we choose, see also the extended discussion in Appendix D in [38]. Using the distribution function x leads to

$$\hat{g}^K = -2\pi i \begin{pmatrix} \mathcal{G} & \mathcal{F} \\ -\tilde{\mathcal{F}} & -\tilde{\mathcal{G}} \end{pmatrix}^R \begin{pmatrix} x & 0 \\ 0 & \tilde{x} \end{pmatrix} \begin{pmatrix} \mathcal{G} & \mathcal{F} \\ -\tilde{\mathcal{F}} & -\tilde{\mathcal{G}} \end{pmatrix}^A. \tag{2.33}$$

The equations of motion for x and $\tilde{x}$ read

$$\begin{aligned} \left(i\hbar\vec{v}_F\vec{\nabla} + i\hbar\partial_t\right)x - [\gamma\tilde{\Delta} + \Sigma]^{\mathrm{R}}x - x[\Delta\tilde{\gamma} - \Sigma]^{\mathrm{A}} \\ = -\gamma^R\tilde{\Sigma}^K\tilde{\gamma}^A + \Delta^K\tilde{\gamma}^A + \gamma^R\tilde{\Delta}^K - \Sigma^K, \end{aligned} \tag{2.34}$$

$$\begin{aligned} \left(i\hbar\vec{v}_F\vec{\nabla} - i\hbar\partial_t\right)\tilde{x} - [\tilde{\gamma}\Delta + \tilde{\Sigma}]^{\mathrm{R}}\tilde{x} - \tilde{x}[\tilde{\Delta}\gamma - \tilde{\Sigma}]^{\mathrm{A}} \\ = -\tilde{\gamma}^R\Sigma^K\gamma^A + \tilde{\Delta}^K\gamma^A + \tilde{\gamma}^R\Delta^K - \tilde{\Sigma}^K. \end{aligned} \tag{2.35}$$

Note that x and $\tilde{x}$ are, just as the coherence functions, matrices in spin-space. A detailed discussion of the derivation can be found in [38, 42]. We note here that if we are in a normal region where $\Delta^X = 0$ and $\gamma^X = 0$ the equation is identical to a Quantum Boltzmann equation.
The full function x can furthermore be split in different ways. One common method is to split the function according to

$$x = x^{eq} + x^a, \tag{2.36}$$

with the two parts representing the global equilibrium part x^{eq}, given by

$$x^{eq} = \left(\mathbb{1} - \gamma^R \tilde{\gamma}^A\right) \tanh \frac{\varepsilon}{2T}, \tag{2.37}$$

and the 'anomalous' part x^a that contains all nonequilibrium effects. This has several advantages. Firstly, the splitting into pure equilibrium and pure nonequilibrium allows for a similiar splitting of observables into (pure) equilibrium and (pure) nonequilbrium parts. Secondly, since the global equilibrium is independent of spatial position, we can use the splitting to only step the anomalous part x^a using Eqs. (2.34) and (2.35) for x^a only which simplifies calculations. Thirdly, the above global-equilibrium splitting is often used as a starting point for linear repsonse calculations, see also [42].

Another possible choice is the splitting

$$x = x^{le} + x^a, \tag{2.38}$$

meaning a *local* equilibrium part and an anomalous part x^a. This choice will generally not be identical to the global-equilibrium variant. Using

$$F_0 \equiv \tanh \frac{\varepsilon + e\phi(\vec{r}\,)}{2T}, \tag{2.39}$$

the local equilibrium x^{le} is given by

$$x^{le} = F_0 + \gamma^R \tilde{F}_0 \tilde{\gamma}^A \equiv \tanh \frac{\varepsilon + e\phi(\vec{r}\,)}{2T} - \gamma^R \tanh \frac{\varepsilon - e\phi(\vec{r}\,)}{2T} \tilde{\gamma}^A, \tag{2.40}$$

where $\phi(\vec{r})$ is the local electrochemical potential[38]. As discussed in more detail in Sect. 2.4, $\phi(\vec{r})$ is chosen such that charge neutrality is obtained. Note that since we subtract a *local* equilibrium instead of a global equilibrium, this splitting of x does not allow the same distinction into equilibrium and nonequilibrium observables as Eq. (2.36). According to Ref. [38] the main advantages are that we get explicit driving terms in the self-energies, as will be discussed in Sect. 2.4, and more stable numerical results.

2.1.4 Self-consistency equation for the order parameter

In Sect. 2.1.2 and 2.1.3, we have just assumed that there will be an off-diagonal element Δ^X in the self-energies but did not specify how this self-energy is obtained. As described in Eq. (2.10), the superconducting order parameter $\Delta_{\sigma,\sigma'}$ is tightly linked to the presence of spin-singlet superconducting electron-hole correlations. In this thesis, we will only discuss s-wave superconductors, meaning that their order parameter is independent of momentum direction and mixes the two opposite spin directions. We will abbreviate this order parameter as Δ_0 in order to distinguish it from the full Δ^R entering the self-energies in Eq. (2.22). From BCS theory, one can derive the self-consistency equation

$$\Delta_0 = \frac{\lambda N_F}{16\pi i} \int_{-\varepsilon_c}^{\varepsilon_c} \mathrm{d}\varepsilon \int \frac{\mathrm{d}\Omega}{4\pi} \operatorname{Tr}\left[i\sigma_2(\hat{\tau}_1 - i\hat{\tau}_2)\hat{g}^K\right], \tag{2.41}$$

where λ is the spin-singlet pairing interaction and N_F the density of states at the Fermi level[31]. This equation is commonly referred to as the gap equation, since it determines the superconducting order parameter and hence the energy gap. From Eq. (2.24), the trace over particle-hole space simplifies the expression to

$$\Delta_0 = \frac{\lambda N_F}{8\pi i} \int_{-\varepsilon_c}^{\varepsilon_c} \mathrm{d}\varepsilon \int \frac{\mathrm{d}\Omega}{4\pi} \operatorname{Tr}_{\mathrm{spin}}\left[i\sigma_2 f^K\right], \tag{2.42}$$

where f^K is the top-right component of $\hat{g}^K$. Since $\hat{g}^K$ is linear in x, as is evident from Eq. (2.33), the splitting of the distribution function x according to Eq. (2.38) leads to the similiar splitting

$$\hat{g}^K = g^{\mathrm{le}} + g^a, \tag{2.43}$$

and hence

$$f^K = f^{\mathrm{le}} + f^a. \tag{2.44}$$

There will thus be two contributions to the order parameter, one caused only by the local equilibrium and one that is purely due to nonequilbrium effects. The coupling constant λ in Eq. (2.41) and similiarly ε_c, have to be repaced with the experimentally accessible T_c. Care has to be taken with f^{le} that contains a logarithmic divergence. Details on this treatment can be found in, e.g., [43], [44].

After replacing λ and the cutoff energy ε_c, the gap equation in the limit of $\varepsilon_c \to \infty$ reads

$$\Delta_0 \ln\frac{T}{T_c} = \frac{1}{2}\int_{-\infty}^{\infty} \mathrm{d}\varepsilon \left(\frac{1}{(-2\pi i)}\left\langle \operatorname{Tr}_{\mathrm{spin}}\left(i\sigma_2 f^K\right)\right\rangle_{\Omega_{\vec{p}_F}} - \frac{\Delta_0}{\varepsilon}\tanh\frac{\varepsilon}{2T}\right), \tag{2.45}$$

where $\langle \dots \rangle$ denotes the Fermi-surface average over trajectories, and the factor $(-2\pi i)$ cancels the one included in the definition of f^K in Eq. (2.33). We note here that the second term in the integral cancels the divergence in the (local) equilibrium part of the singlet component of f^K, while the anomalous (nonequilibrium) part does not have a high-energy divergence and needs no additional treatment.

2.1.5 Observables

Once we have solved Eqs. (2.26) - (2.27) and Eqs. (2.34) - (2.35), we can calculate the full Green's function and use it to obtain physical observables. An easy example that only requires $\hat{g}^R$, and hence only γ and $\tilde{\gamma}$, is the local density of states,

$$N(\varepsilon, \vec{r}) = -\frac{N_F}{2\pi} \, \mathrm{Im} \int \frac{\mathrm{d}\Omega}{4\pi} \, \mathrm{tr} \, \hat{\tau}_3 \hat{g}^R(\varepsilon, \vec{r}). \tag{2.46}$$

Here, N_F is the normal density of states at the Fermi level. Furthermore, we have the charge density

$$\rho_c = \frac{-eN_F}{8\pi i} \int_{-\varepsilon_c}^{\varepsilon_c} \mathrm{d}\varepsilon \int \frac{\mathrm{d}\Omega}{4\pi} \, \mathrm{tr} \, \hat{g}^K, \tag{2.47}$$

where we use the convention that the natural constant e has a positive sign, so that the electron charge is $-e$. Similiarly, the spin density measures the density of carriers with spin along an (arbitrary) quantization axis z in spin space,

$$\rho_{s_z} = \frac{iN_F}{8\pi} \int_{-\varepsilon_c}^{\varepsilon_c} \mathrm{d}\varepsilon \int \frac{\mathrm{d}\Omega}{4\pi} \, \mathrm{tr} \, \sigma_z \hat{g}^K. \tag{2.48}$$

A nonvanishing spin density is directly linked to the magnetization, given by

$$M_z = -\mu_B \rho_{s_z} = -\frac{i\mu_B N_F}{8\pi} \int_{-\varepsilon_c}^{\varepsilon_c} \mathrm{d}\varepsilon \int \frac{\mathrm{d}\Omega}{4\pi} \, \mathrm{tr} \, \sigma_z \hat{g}^K, \tag{2.49}$$

where $\mu_B = em_e/\hbar$ is the Bohr magneton.
Associated with each of those two densities is a current, the charge current

$$I_c^z \equiv \frac{-eN_F A_c}{8\pi i} \int_{-\varepsilon_c}^{\varepsilon_c} \mathrm{d}\varepsilon \int \frac{\mathrm{d}\Omega}{4\pi} \, \mathrm{tr} \, v_F^z \hat{\tau}_3 \hat{g}^K, \tag{2.50}$$

where A_c is the junction area perpedicular to the current flow, and the spin current,

$$I_{s_z}^z \equiv \frac{i\mu_B N_F A_c}{8\pi} \int_{-\varepsilon_c}^{\varepsilon_c} \mathrm{d}\varepsilon \int \frac{\mathrm{d}\Omega}{4\pi} \, \mathrm{tr} \, v_F^z \sigma_z \hat{\tau}_3 \hat{g}^K. \tag{2.51}$$

With the parametrization

$$\hat{g}^{\mathrm{K}} \equiv -2\pi i \begin{pmatrix} \mathcal{X} & \mathcal{Y} \\ \tilde{\mathcal{Y}} & \tilde{\mathcal{X}} \end{pmatrix}^{K},$$

we see that the currents as well as the densities depend on the diagonal elements of $\hat{g}^{K}$, meaning $\mathcal{X}$ and $\tilde{\mathcal{X}}$ as defined in Eqs. (2.33). Since both quantities will in turn depend on x, we can identify the physical origins of the various contributions to observables at interfaces. This will be discussed in detail in the next chapter on boundary conditions.

2.2 Boundary conditions at an interface

Metal-superconductor hybrid structures will necessarily contain interfaces between these two components. The coherence and distribution functions in the two regions are then connected via boundary conditions. A prototypical interface connecting two regions can be seen in Fig. 2.1.

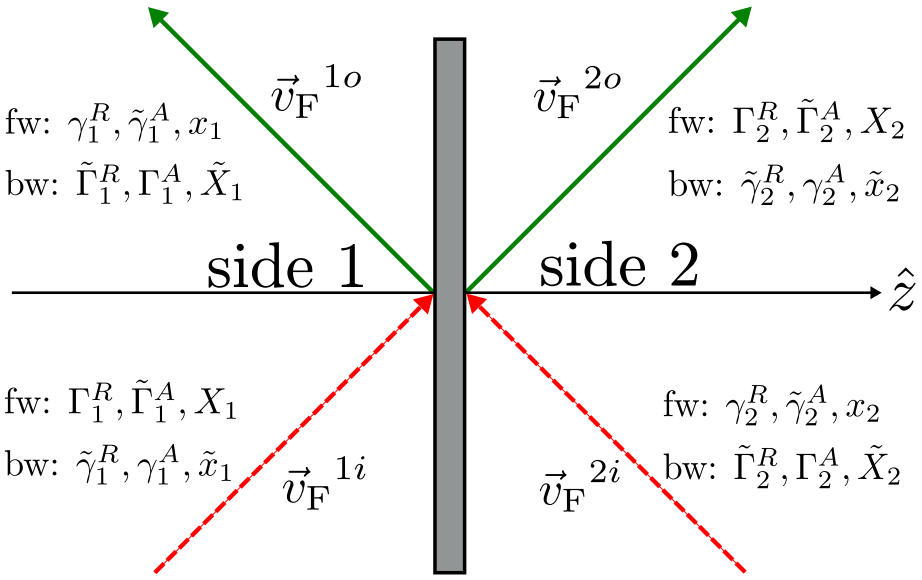

Figure 2.1: *Sketch of an interface connecting two subsystems 1 and 2.*

In the figure, two classes of trajectories for each side are indicated. In stroked red, we have an incoming trajectory, where the momentum points toward the interface, and in solid green an outgoing trajectory, where the momentum points away from the interface. Typically, the momentum orientation is a continous variable and there will be infinitely many trajectories in each subclass, but each individual trajectory belongs to one of the two classes. In the following, we label as + all trajectories going away from the interface, and with − all trajectories going towards the interface.

There are two classes of quantities, namely those with a starting point in the bulk of the respective side, indicated here by small-letter version such as γ or x. In contrast, quantities with their initial condition at the interface use capital letters Γ or X. For a given trajectory, there are six different functions that are stable along the given direction, and they are specified next to the respective direction in Fig. 2.1. To obtain the full Green's function $\check{g}$, we need to obtain all incoming and outgoing functions for all angles and all energies.
Boundaries are typically on the atomic scale, where the quasiclassical approximation does not hold. For our purposes, we assume the scattering matrix to be an external parameter to our model that has to be supplied to quasiclassical theory. We note that it is possible to derive a scattering matrix $\mathcal{S}$ in a microscopic theory, e.g., using a wave-function approach as in [45]. The interface itself is described by a scattering matrix, which in particle-hole space reads

$$S = \begin{pmatrix} S_e & 0 \\ 0 & S_h \end{pmatrix}, \tag{2.52}$$

and there is a symmetry between the particle and hole matrices, namely

$$S_h = \tilde{S}_e^\dagger. \tag{2.53}$$

Each of the two then has four elements

$$S_e \equiv \begin{pmatrix} S_{11} & S_{12} \\ S_{21} & S_{22} \end{pmatrix}, \tag{2.54}$$

and the S_{ij} are spin-space matrices and describe the connection between a particle from side j to one in side i. In all cases,probability current conservation requires the scattering matrix to be unitary, $S^\dagger S = \mathbb{1}$, which implies $S_e^\dagger S_e = \mathbb{1}$.

2.2.1 Analytical expressions

The analytical calculation for the boundary conditions can be done along the lines of [46]. In this thesis, the scattering matrix is always independent of momentum along the interface, so that

$$\underline{S}_{ij}(\vec{p}_{||}) \equiv S_{ij}(-\vec{p}_{||}) = S_{ij}(\vec{p}_{||}), \tag{2.55}$$

and we omit the underbar ($\underline{\ }$) used in the original paper. Using the conventions introduced there, the boundary conditions read

$$\Gamma_2^R = r_{2l}^R \gamma_2^R S_{22}^\dagger + t_{2l}^R \gamma_1^R S_{21}^\dagger, \tag{2.56}$$

$$\tilde{\Gamma}_2^A = S_{22} \tilde{\gamma}_2^A \tilde{r}_{2r}^A + S_{21} \tilde{\gamma}_1^A \tilde{t}_{2r}^A, \tag{2.57}$$

$$X_2^K = r_{2l}^R x_2^K \tilde{r}_{2r}^A + t_{2l}^R x_1^K \tilde{t}_{2r}^A - a_{2l}^R \tilde{x}_1^K \tilde{a}_{2r}^A. \tag{2.58}$$

and similar for their tilde-counterparts. Exchanging the indices $1 \leftrightarrow 2$ gives the quantities on the other side. One very important thing to note here is that the boundary condition for X, Eq. (2.58), is always used for the *full* distribution function x, even when the splitting according to Eq. (2.38) is applied. After applying the boundary condition to the full function, however, only the anomalous part x^a is stepped with the tools discussed in Sect. 2.3.
The amplitudes r_{2l}^R, t_{2l}^R, and a_{2l}^R in the above equations are given by

$$r_{2l}^R = \left[S_{22}^\dagger - \beta_{12}^R \left(\beta_{11}^R\right)^{-1} S_{21}^\dagger\right]^{-1}, \tag{2.59}$$

$$t_{2l}^R = -\left[\beta_{11}^R \left(\beta_{12}^R\right)^{-1} S_{22}^\dagger - S_{21}^\dagger\right]^{-1}, \tag{2.60}$$

$$a_{2l}^R = \left(\Gamma_2^R S_{22} - S_{22}\gamma_2^R\right)\left(\tilde{\beta}_{21}^R\right)^{-1}, \tag{2.61}$$

where Γ^R can be obtained from Eq. (2.56), and the auxilliary quantities β_{ij} used are here

$$\beta_{ij}^R \equiv S_{ij}^R - \gamma_j^R S_{ij}^\dagger \tilde{\gamma}_i^R, \qquad \tilde{\beta}_{ij}^R \equiv S_{ji} - \tilde{\gamma}_j^R S_{ji} \gamma_i^R. \tag{2.62}$$

The diagonal Keldysh amplitudes, which we need to calculate the observables discussed in Sect. 2.1.5, read

$$\mathcal{X}^a \equiv \mathcal{G}^R\left(x^a - \gamma^R \tilde{x}^a \tilde{\gamma}^A\right)\mathcal{G}^A, \qquad \tilde{\mathcal{X}}^a \equiv \tilde{\mathcal{G}}^R\left(\tilde{x}^a - \tilde{\gamma}^R x^a \gamma^A\right)\tilde{\mathcal{G}}^A. \tag{2.63}$$

Starting with the former, we use commutation rules of the form $\tilde{\mathcal{G}}^R\tilde{\gamma} = \tilde{\gamma}^R\mathcal{G}^R$, and find

$$\mathcal{X}_{2,+}^a = \mathcal{G}_+^R\left(X_2^a - \Gamma^R \tilde{x}_2^a \tilde{\Gamma}^A\right)\mathcal{G}_+^A = \mathcal{G}_+^R X_2^a \mathcal{G}_+^A - \Gamma^R \tilde{\mathcal{G}}_+^R \tilde{x}_2^a \tilde{\mathcal{G}}_+^A \tilde{\Gamma}^A, \tag{2.64}$$

$$\tilde{\mathcal{X}}_{2,+}^a = \tilde{\mathcal{G}}_+^R\left(\tilde{x}_2^a - \tilde{\gamma}^R X_2^a \gamma^A\right)\tilde{\mathcal{G}}_+^A = \tilde{\mathcal{G}}_+^R \tilde{x}_2^a \tilde{\mathcal{G}}_+^A - \tilde{\gamma}^R \mathcal{G}_+^R X_2^a \mathcal{G}_+^A \gamma^A \tag{2.65}$$

where $\mathcal{G}_+^X$ labels the Green's functions for the outgoing trajectories. The Keldysh amplitude resulting from using the boundary conditions for X^a is then

$$\mathcal{X}_{2,+}^a = \mathcal{G}_+^R r_{2l}^R x_2^K \tilde{r}_{2r}^A \mathcal{G}_+^A + \mathcal{G}_+^R t_{2l}^R x_1^K \tilde{t}_{2r}^A \mathcal{G}_+^A - \mathcal{G}_+^R a_{2l}^R \tilde{x}_1^K \tilde{a}_{2r}^A \mathcal{G}_+^A - \mathcal{G}_+^R \Gamma^R \tilde{x}_2^a \tilde{\Gamma}^A \mathcal{G}_+^A, \tag{2.66}$$

which allows us to define the "physical" scattering amplitudes

$$\begin{aligned} \bar{r}_{ee}^R &= \mathcal{G}_+^R r_{2l}^R, & \bar{r}_{ee}^A &= \tilde{r}_{2r}^A \mathcal{G}_+^A, & t_{ee}^R &= \mathcal{G}_+^R t_{2l}^R, & t_{ee}^A &= \tilde{t}_{2r}^A \mathcal{G}_+^A, \\ \bar{r}_{eh}^R &= \mathcal{G}_+^R \Gamma^R, & \bar{r}_{eh}^A &= \tilde{\Gamma}^A \mathcal{G}_+^A, & t_{eh}^R &= \mathcal{G}_+^R a_{2l}^R, & t_{eh}^A &= \tilde{a}_{2r}^A \mathcal{G}_+^A. \end{aligned} \tag{2.67}$$

These four amplitudes describe reflection of an electron ($\bar{r}_{ee}^R$), transmission of an electron (t_{ee}^R), Andreev reflection of a hole ($\bar{r}_{he}^R$) and transmission of a hole with branch conversion to an electron (t_{eh}^R). Here, the presence (absence) of a bar

denotes that the respective amplitude is originates from an excitation coming in from the right (left). Analogous amplitudes are found for the other side of the interface by swapping the indices $1 \leftrightarrow 2$ and inserting the respective $\mathcal{G}^R$. Using the above definitions, the boundary condition for $\mathcal{X}_2^a$ can be written as

$$\mathcal{X}_{2,+}^a = \bar{r}_{ee}^R x_2^K \bar{r}_{ee}^A + t_{ee}^R x_1^K t_{ee}^A - t_{eh}^R \tilde{x}_1^K t_{eh}^A - \bar{r}_{eh}^R \tilde{x}_2^a \bar{r}_{eh}^A, \tag{2.68}$$

For $\tilde{\mathcal{X}}^A$, we find

$$\begin{aligned}\tilde{\mathcal{X}}_{2,+}^a &= \tilde{\mathcal{G}}_+^R \tilde{x}_2^a \tilde{\mathcal{G}}_+^A - \tilde{\gamma}^R \mathcal{G}_+^R X_2^a \mathcal{G}_+^A \gamma^A \\ &= \tilde{\mathcal{G}}_+^R \tilde{x}_2^a \tilde{\mathcal{G}}_+^A - \tilde{\gamma}^R \left(\bar{r}_{ee}^R x_2^K \bar{r}_{ee}^A + t_{ee}^R x_1^K t_{ee}^A - t_{eh}^R \tilde{x}_1^K t_{eh}^A \right) \gamma^A. \end{aligned} \tag{2.69}$$

For the incoming trajectories, we have

$$\mathcal{X}_{2,-}^a = \mathcal{G}_-^R \left(x_2^a - \gamma^R \tilde{X}_2^a \tilde{\gamma}^A \right) \mathcal{G}_-^A = \mathcal{G}_-^R x_2^a \mathcal{G}_-^A - \gamma^R \tilde{\mathcal{G}}_-^R \tilde{X}_2^a \tilde{\mathcal{G}}_-^A \tilde{\gamma}^A, \tag{2.70}$$

$$\tilde{\mathcal{X}}_{2,-}^a = \tilde{\mathcal{G}}_-^R \left(\tilde{X}_2^a - \tilde{\Gamma}^R x_2^a \Gamma^A \right) \tilde{\mathcal{G}}_-^A = \tilde{\mathcal{G}}_-^R \tilde{X}_2^a \tilde{\mathcal{G}}_-^A - \tilde{\Gamma}^R \mathcal{G}_-^R x_2^a \mathcal{G}_-^A \Gamma^A, \tag{2.71}$$

which can be rewritten as

$$\mathcal{X}_{2,-}^a = \mathcal{G}_-^R x_2^K \tilde{\mathcal{G}}_-^A - \gamma^R \left(\bar{r}_{hh}^R \tilde{x}_2^K \bar{r}_{hh}^A + t_{hh}^R \tilde{x}_1^K t_{hh}^A - t_{he}^R x_1^K t_{he}^A \right) \tilde{\gamma}^A, \tag{2.72}$$

$$\tilde{\mathcal{X}}_{2,-}^a = \bar{r}_{hh}^R \tilde{x}_2^K \bar{r}_{hh}^A + t_{hh}^R \tilde{x}_1^K t_{hh}^A - t_{he}^R x_1^K t_{he}^A - \bar{r}_{he}^R x_2^a \bar{r}_{he}^A. \tag{2.73}$$

Here, we have used the additional amplitudes

$$\begin{aligned} \bar{r}_{hh}^R &= \tilde{\mathcal{G}}_-^R \tilde{r}_{2l}^R, & \bar{r}_{hh}^A &= r_{2r}^A \mathcal{G}_-^A, & t_{hh}^R &= \tilde{\mathcal{G}}_-^R \tilde{t}_{2l}^R, & t_{hh}^A &= t_{2r}^A \mathcal{G}_-^A, \\ \bar{r}_{he}^R &= \tilde{\mathcal{G}}_-^R \tilde{\Gamma}^R, & \bar{r}_{he}^A &= \Gamma^A \tilde{\mathcal{G}}_-^A, & t_{he}^R &= \tilde{\mathcal{G}}_-^R \tilde{a}_{2l}^R, & t_{he}^A &= a_{2r}^A \mathcal{G}_-^A. \end{aligned} \tag{2.74}$$

For the time-independent case, one can show from these definitions that the retarded and advanced scattering amplitudes are related via

$$r_{\alpha\beta}^A = \left[r_{\alpha\beta}^R \right]^\dagger, t_{\alpha\beta}^A = \left[t_{\alpha\beta}^R \right]^\dagger, \tag{2.75}$$

where α, β is any combination of e, h[46]. From the amplitudes, we obtain scattering *probabilities* via

$$T_{\alpha\beta} \equiv |t_{\alpha\beta}^R|^2, \qquad R_{\alpha\beta} \equiv |r_{\alpha\beta}^R|^2. \tag{2.76}$$

Note that both amplitudes and probabilities are still matrices in spin-space. In an impurity-free system, the probabilities on the normal side of the interface satisfy the relation

$$R_{ee,\sigma} + R_{he,\sigma} + T_{ee,\sigma} \left(1 - |\tilde{\gamma}_\sigma^R|^2 \right) + T_{he,\sigma} \left(1 - |\gamma_\sigma^R|^2 \right) = 1, \tag{2.77}$$

which guarantees probability and charge conservation[28]. A similiar relation be derived in the case of a system with impurities or at superconductor-superconductor interface. Note that the transmission "probabilities" $T_{\alpha\beta}$ only become actual probabilities, in the sense of normalized quantities between zero and one, with the additional factors $(1 - |\gamma_\sigma^R|^2)$. This is a technicality resulting from the way the boundary conditions are derived within quasiclassical theory.

2.2.2 Spin-active interface between clean N-S systems

The main aim of this thesis is to investigate hybrid systems of normal-metal and superconducting regions connected via spin-active interfaces. In the case of an interface between an impurity-free metal and a (possibly dirty) superconductor, the above boundary conditions simplify considerably since there are no incoming coherence functions on the normal side of the interface. Without loss of generality, we assume side one to be a normal metal and side two to be superconducting, hence $\Gamma_1^X = \gamma_1^X = 0$ and we denote $\Gamma_2^X = \Gamma^X, \gamma_2^X = \gamma^X$. The spin-active interface is described by the scattering matrix

$$S_e = \begin{pmatrix} \mathcal{S}_R & \mathcal{S}_D \\ \mathcal{S}_D & -\mathcal{S}_R \end{pmatrix}, \tag{2.78}$$

where the sign in the lower-right element is chosen so that the scattering matrix is unitary, $S_e^\dagger S_e = \mathbb{1}$. The two matrices $\mathcal{S}_R$ and $\mathcal{S}_D$ are in turn spin-space matrices, given by

$$\mathcal{S}_R = \begin{pmatrix} \sqrt{R_\uparrow} e^{i\vartheta/2} & 0 \\ 0 & \sqrt{R_\downarrow} e^{-i\vartheta/2} \end{pmatrix}, \mathcal{S}_D = \begin{pmatrix} \sqrt{D_\uparrow} e^{i\vartheta/2} & 0 \\ 0 & \sqrt{D_\downarrow} e^{-i\vartheta/2} \end{pmatrix}, \tag{2.79}$$

with the so-called spin-mixing angle ϑ, and the spin-dependent transmission and reflection probabilities D_σ and R_σ that satisfy $R_\sigma + D_\sigma = 1$[45, 46].
Out of the twelve quantities needed to obtain all scattering amplitudes it is in fact sufficient to calculate the six quantities

$$r_{1l}^R, t_{1l}^R, a_{1l}^R, \qquad r_{2l}^R, t_{2l}^R, a_{2l}^R, \tag{2.80}$$

and the remaining six can be obtained from the symmetries in Eq. (2.75).

Using Eqs. (2.59)-(2.61), we find

$$r_{2l}^R = -\mathcal{S}_\mathcal{R}, \qquad t_{2l}^R = \mathcal{S}_\mathcal{D}, \qquad a_{2l}^R = \mathcal{S}_\mathcal{R} \gamma_2^R \mathcal{S}_\mathcal{D}^\dagger. \tag{2.81}$$

At the interface, we further find

$$\begin{aligned} \mathcal{G}_+^R &= \begin{pmatrix} 1 + \Gamma_+^R \tilde{\gamma}^R & 0 \\ 0 & 1 + \Gamma_-^R \tilde{\gamma}^R \end{pmatrix} = \begin{pmatrix} 1 + f_\vartheta \gamma^R \tilde{\gamma}^R & 0 \\ 0 & 1 + f_\vartheta^* \gamma^R \tilde{\gamma}^R \end{pmatrix}, \\ \mathcal{G}_-^R &= \begin{pmatrix} 1 + \gamma^R \tilde{\Gamma}_-^R & 0 \\ 0 & 1 + \gamma^R \tilde{\Gamma}_+^R \end{pmatrix} = \begin{pmatrix} 1 + f_\vartheta \gamma^R \tilde{\gamma}^R & 0 \\ 0 & 1 + f_\vartheta^* \gamma^R \tilde{\gamma}^R \end{pmatrix}, \end{aligned} \tag{2.82}$$

and hence $\mathcal{G}_+^R = \mathcal{G}_-^R = \mathcal{G}^R$ does not depend on the momentum direction. The same holds for the remaining three functions $\tilde{\mathcal{G}}^R$, $\mathcal{G}^A$, and $\tilde{\mathcal{G}}^A$. Note futher that $\mathcal{G}^X$, $\mathcal{S}_\mathcal{R}$, and $\mathcal{S}_\mathcal{D}$ are all diagonal matrices, while the coherence functions γ^X are proportional to $i\sigma_2$.

After some rearrangements, we find

$$\bar{r}^R_{ee} = \mathcal{G}^R r^R_{2l} - \mathcal{S}_\mathcal{R}\mathcal{G}^R, \qquad t^R_{ee} = \mathcal{G}^R t^R_{2l} = \mathcal{G}^R\mathcal{S}_\mathcal{D} = \mathcal{S}_\mathcal{D}\mathcal{G}^R, \tag{2.83}$$

$$\bar{r}^R_{eh} = \mathcal{G}^R\Gamma^R = \mathcal{S}_\mathcal{R}\mathcal{G}^R\gamma^R\mathcal{S}^\dagger_\mathcal{R}, \qquad t^R_{eh} = \mathcal{G}^R a^R_{2l} = \mathcal{S}_\mathcal{R}\mathcal{G}^R\gamma^R\mathcal{S}^\dagger_\mathcal{D}, \tag{2.84}$$

Note that all these qualities are still spin matrices.

An analogous calculation can be performed for the quantities on the left-hand side, giving

$$r^R_{1l} = \mathcal{S}_\mathcal{R} - \mathcal{S}_\mathcal{D}\gamma^R_2\mathcal{S}^\dagger_\mathcal{R}\tilde{\gamma}^R_2\mathcal{G}^R\mathcal{S}_\mathcal{D} \tag{2.85}$$

$$t^R_{1l} = \mathcal{S}_\mathcal{D}\left[1 - \mathcal{S}_\mathcal{R}\gamma^R_2\mathcal{S}^\dagger_\mathcal{R}\tilde{\gamma}^R_2\right]^{-1} = \mathcal{S}_\mathcal{D}\mathcal{G}^R, \tag{2.86}$$

$$a^R_{1l} = \mathcal{S}_\mathcal{D}\gamma^R_2\tilde{\mathcal{G}}^R\mathcal{S}^\dagger_\mathcal{R}. \tag{2.87}$$

Having obtained these amplitudes, and noting that $\mathcal{G}^R_1 = 0$ since either the incoming γ^R or the incoming $\tilde{\gamma}^R$ will be vanishing, we obtain the physical amplitudes

$$r^R_{ee} = r^R_{1l} = \mathcal{S}_\mathcal{R} - \mathcal{S}_\mathcal{D}\gamma^R_2\mathcal{S}^\dagger_\mathcal{R}\tilde{\gamma}^R_2\mathcal{G}^R\mathcal{S}_\mathcal{D} \equiv R^R, \qquad \bar{t}^R_{ee} = t^R_{1l} = \mathcal{S}_\mathcal{D}\mathcal{G}^R, \tag{2.88}$$

$$r^R_{eh} = \Gamma^R_1 = \mathcal{S}_\mathcal{D}\mathcal{G}^R\gamma^R\mathcal{S}^\dagger_\mathcal{D}, \qquad \bar{t}^R_{eh} = a^R_{1l} = \mathcal{S}_\mathcal{D}\mathcal{G}^R\gamma^R_2\mathcal{S}^\dagger_\mathcal{R}. \tag{2.89}$$

The general analytic formulas thus provide us with explicit expressions to use for the boundary conditions Eqs. (2.56) and (2.58). The amplitudes can be disentangled into basic scattering processes to gain additional insigth into the physics.

This can also be achieved by an alternative, graphical approach to obtain the physical scattering amplitudes derived above.

2.2.3 Graphical calculation

In addition to the analytical formulas used in the last section, we can also obtain the physical amplitudes using a grahical approach. One big advantage of this method is that it allows for a more intuitive picture of the physics involved.

For the graphical representation, we will use full lines for electron trajectories and dashed ones for hole trajectories. In a superconductor, or in general when we have nonzero coherence functions γ^X and $\tilde{\gamma}^X$, two such trajectories can be connected via these coherence functions, shown in Figure 2.2.

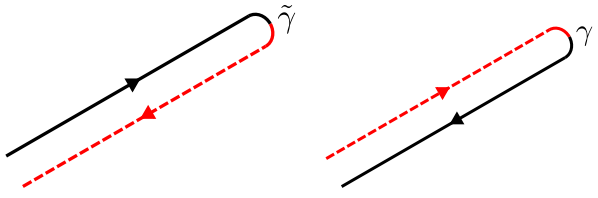

Figure 2.2: *Elementary branch conversion $e \to h$ ($h \to e$) mediated by $\tilde{\gamma}$ (γ).*

In the presence of a superconducting self-energy Δ, all electron-like (hole-like) excitations have a non-vanishing conversion chance to a hole-like (electron-like) excitation, and each conversion has a likelihood given by γ ($\tilde{\gamma}$), as shown on the left (right). The physical scattering amplitudes include these type of processes to infinite order.
As an example, the first two orders of possible processes leading to an electron reflection of an electron originating from the right side, $\bar{r}_{ee}$, can be expressed graphically as shown in Fig. 2.3.

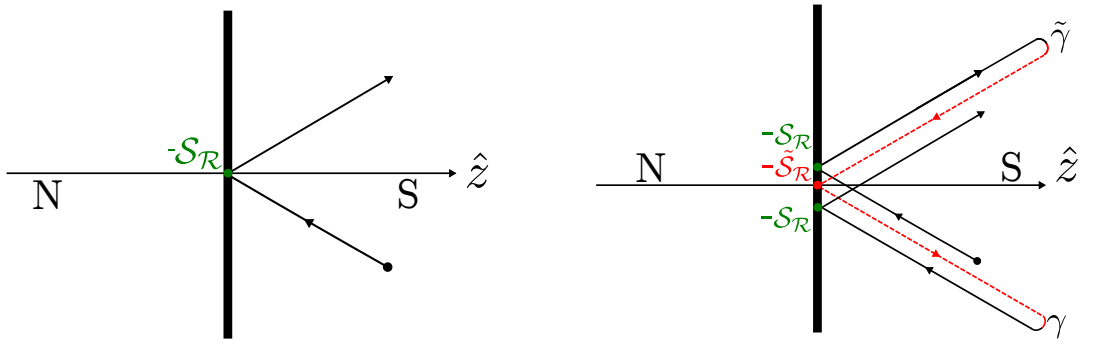

(a) *Zeroth order: no conversion processes, only electron reflection.*

(b) *First order: initial electron reflection, electron-hole conversion, reflection of the hole, hole-electron conversion and again electron reflection.*

Figure 2.3: *First two orders of the electron reflection process* $\bar{r}^R_{ee}$

Note that trajectories with the same momentum orientation would actually overlap and are only shifted for better visibility. In order to get an analytic expression from these pictures, we start at the beginning of the trajectory and write down all scattering matrices and coherence functions we encounter along the path to the final outgoing arrow, starting from the right-hand side. For example, the two diagrams in Fig. 2.3 give

$$\bar{r}^R_{ee,0} = -\mathcal{S}_\mathcal{R}, \qquad \bar{r}^R_{ee,1} = -\mathcal{S}_\mathcal{R}\gamma^R(-\tilde{\mathcal{S}}_\mathcal{R})\tilde{\gamma}^R(-\mathcal{S}_\mathcal{R}), \tag{2.90}$$

from which we see that, for an initial electron-like excitation, a single loop gives a contribution $-\mathcal{S}_\mathcal{R}\gamma^R(-\tilde{\mathcal{S}}_\mathcal{R})\tilde{\gamma}^R = \mathcal{S}_\mathcal{R}\gamma^R\tilde{\mathcal{S}}_\mathcal{R}\tilde{\gamma}^R$, so that further orders read

$$\bar{r}^R_{ee,n} = \left(\mathcal{S}_\mathcal{R}\gamma^R\tilde{\mathcal{S}}_\mathcal{R}\tilde{\gamma}^R\right)^n(-\mathcal{S}_\mathcal{R}). \tag{2.91}$$

Since the resulting amplitude sums all these orders we obtain a geometric series and the final expression reads

$$\bar{r}^R_{ee} = \sum_{n=0}^{\infty}\bar{r}^R_{ee,n} = \sum_{n=0}^{\infty}\left(\gamma^R\tilde{\mathcal{S}}_\mathcal{R}\tilde{\gamma}^R\mathcal{S}_\mathcal{R}\right)^n(-\mathcal{S}_\mathcal{R}) = \frac{1}{1-\gamma^R\tilde{\mathcal{S}}_\mathcal{R}\tilde{\gamma}^R\mathcal{S}_\mathcal{R}}(-\mathcal{S}_\mathcal{R}) = -\mathcal{G}^R\mathcal{S}_\mathcal{R}, \tag{2.92}$$

where we identified $\mathcal{G}^R$ using Eq. (2.82). All other amplitudes can be constructed in the same way. Fig. 2.4 shows all first-order diagrams for the four possible processes

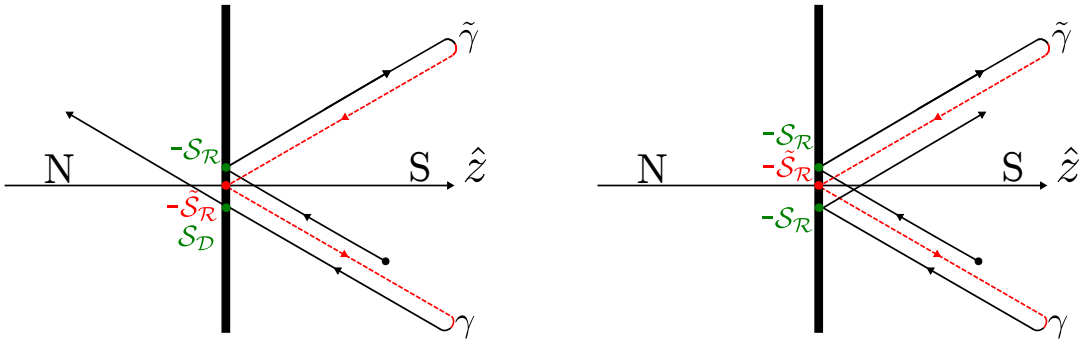

(a) *First-order diagramm for* $\bar{t}^R_{ee}$ **(b)** *First-order diagramm for* $\bar{r}^R_{ee}$

(c) *First-order diagram of* $\bar{t}^R_{he}$ **(d)** *First-order diagramm for* $\bar{r}^R_{he}$

Figure 2.4: *First-order processes for all four amplitudes* $\bar{t}^R_{ee}$, $\bar{r}^R_{ee}$, $\bar{t}^R_{he}$, $\bar{r}^R_{he}$

for an electron-like particle interacting with the interface.
The hole-like amplitudes can be constructed in an analogous way by replacing all particle and hole trajectories, coherence functions, and scattering matrix elements accordingly. Using these diagrams, we can easily obtain the analytical expressions in the same way as for the reflection amplitude. We find

$$\bar{t}^R_{ee} = \sum_{n=0}^{\infty} \mathcal{S}_\mathcal{D} \left(\gamma^R \tilde{\mathcal{S}}_\mathcal{R} \tilde{\gamma}^R \mathcal{S}_\mathcal{R}\right)^n = \sum_{n=0}^{\infty} \mathcal{S}_\mathcal{D} \left(\mathcal{S}_\mathcal{R} \gamma^R \tilde{\mathcal{S}}_\mathcal{R} \tilde{\gamma}^R\right)^n = \mathcal{S}_\mathcal{D} \mathcal{G}^R, \tag{2.93}$$

$$\bar{t}^R_{he} = \sum_{n=0}^{\infty} \tilde{\mathcal{S}}_\mathcal{D} \tilde{\gamma}^R \left(\mathcal{S}_\mathcal{R} \gamma^R \tilde{\mathcal{S}}_\mathcal{R} \tilde{\gamma}^R\right)^n (-\mathcal{S}_\mathcal{R}) = -\tilde{\mathcal{S}}_\mathcal{D} \tilde{\gamma}^R \mathcal{G}^R \mathcal{S}_\mathcal{R}, \tag{2.94}$$

$$\bar{r}^R_{he} = \sum_{n=0}^{\infty} (-\tilde{\mathcal{S}}_\mathcal{R}) \tilde{\gamma}^R \left(\mathcal{S}_\mathcal{R} \gamma^R \tilde{\mathcal{S}}_\mathcal{R} \tilde{\gamma}^R\right)^n (-\mathcal{S}_\mathcal{R}) = \tilde{\mathcal{S}}_\mathcal{R} \tilde{\gamma}^R \mathcal{G}^R \mathcal{S}_\mathcal{R}, \tag{2.95}$$

and by tilde conjugation we can obtain the analogous quantities for hole-like excitations. Similarly, we can draw diagrams for excitations moving in from the left (normal) side. We restrict ourselves to the reflection amplitudes here. The first two diagrams are shown in Fig. 2.5.

Summing the diagrams, we obtain

$$\begin{aligned} r^R_{ee} &= \mathcal{S}_\mathcal{R} - \mathcal{S}_\mathcal{D} \gamma^R \tilde{\mathcal{S}}_\mathcal{R} \tilde{\gamma}^R \mathcal{S}_\mathcal{D} - \mathcal{S}_\mathcal{D} \gamma^R \tilde{\mathcal{S}}_\mathcal{R} \tilde{\gamma}^R \left(\mathcal{S}_\mathcal{R} \gamma^R \tilde{\mathcal{S}}_\mathcal{R} \tilde{\gamma}^R\right) \mathcal{S}_\mathcal{D} + \dots \\ &= \mathcal{S}_\mathcal{R} - \mathcal{S}_\mathcal{D} \gamma^R \tilde{\mathcal{S}}_\mathcal{R} \tilde{\gamma}^R \mathcal{G}^R \mathcal{S}_\mathcal{D} \end{aligned} \tag{2.96}$$

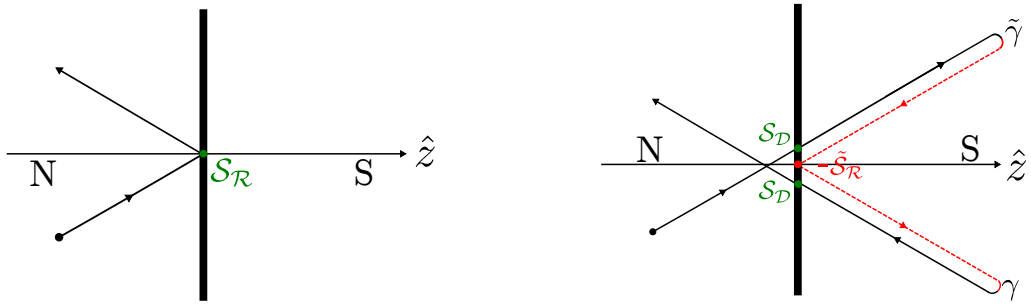

(a) *Zeroth order: direct reflection*

(b) *First order: Transmission, two conversions, transmission*

Figure 2.5: *First two orders of the left-side electron reflection process* r^R_{ee}

Similiar diagrams can be drawn for the remaining three amplitudes, and after summation one finds

$$t^R_{ee} = \sum_{n=0}^{\infty} \left((-\mathcal{S}_\mathcal{R})\gamma^R(-\tilde{\mathcal{S}}_\mathcal{R})\tilde{\gamma}^R\right)^n \mathcal{S}_\mathcal{D} = \mathcal{G}^R\mathcal{S}_\mathcal{D}, \tag{2.97}$$

$$t^R_{he} = \sum_{n=0}^{\infty} (-\tilde{\mathcal{S}}_\mathcal{R})\tilde{\gamma}^R \left((-\mathcal{S}_\mathcal{R})\gamma^R(-\tilde{\mathcal{S}}_\mathcal{R})\tilde{\gamma}^R\right)^n \mathcal{S}_\mathcal{D} = -\tilde{\mathcal{S}}_\mathcal{R}\tilde{\gamma}^R\mathcal{G}^R\mathcal{S}_\mathcal{D}, \tag{2.98}$$

$$r^R_{he} = \sum_{n=0}^{\infty} \tilde{\mathcal{S}}_\mathcal{D}\tilde{\gamma}^R \left((-\mathcal{S}_\mathcal{R})\gamma^R(-\tilde{\mathcal{S}}_\mathcal{R})\tilde{\gamma}^R\right)^n \mathcal{S}_\mathcal{D} = \tilde{\mathcal{S}}_\mathcal{D}\tilde{\gamma}^R\mathcal{G}^R\mathcal{S}_\mathcal{D}. \tag{2.99}$$

Again, all hole-excitation analogues obtained by tilde conjugation. We note here that the amplitudes agree with those obtained in Ref. [47]. From this procedure we see the benefit of the graphical calculations compared to the analytical one. At least if one side of the interface is trivial, they are easier to obtain since it is usually sufficient to write down the first two or three orders of the diagram and induce the final sum. In contrast, the analytical calculation requires us to calculate auxialliary quantities to obtain the interface amplitudes which we then use to obtain the physical scattering amplitudes. Especially the normal-side amplitudes require a lot of analytical manipulation in order to obtain a shape that makes the physics transparent, while the graphical calculation can be directly interpreted.

2.2.4 Spin-active interface between two superconductors

If we have superconductor-superconductor interfaces, or an interface between a superconductor and a normal metal with impurity-induced superconductivity, the above formulas are no longer correct since we have incoming γ from *both* sides of the interface. In this case, we can still use the general, analytic boundary conditions discussed in Subsect. 2.2.1. Similiarly to before, a graphical calculation is equally

possible although lengthy. Using Eqs. (2.59) - (2.61) we find

$$r_{1l}^R = \mathcal{S}_R \frac{1 - \gamma_2^R \mathcal{S}_R^\dagger \tilde{\gamma}_2^R \mathcal{S}_R^{-1}}{1 - \gamma_1^R \mathcal{S}_D^\dagger \tilde{\gamma}_2^R \mathcal{S}_D - \gamma_2^R \mathcal{S}_R^\dagger \tilde{\gamma}_2^R \mathcal{S}_R}, \tag{2.100}$$

$$t_{1l}^R = \mathcal{S}_D \frac{1 - \gamma_1^R \mathcal{S}_D^\dagger \tilde{\gamma}_2^R \mathcal{S}_D^{-1}}{1 - \gamma_1^R \mathcal{S}_D^\dagger \tilde{\gamma}_2^R \mathcal{S}_D - \gamma_2^R \mathcal{S}_R^\dagger \tilde{\gamma}_2^R \mathcal{S}_R}, \tag{2.101}$$

$$a_{1l}^R = -\left(r_{1l}^R \gamma_1^R \mathcal{S}_R^\dagger \mathcal{S}_R + t_{1l}^R \gamma_2^R \mathcal{S}_D^\dagger \mathcal{S}_R + \mathcal{S}_R \gamma_1^R\right) \left(\mathcal{S}_D - \tilde{\gamma}_2^R \mathcal{S}_D \gamma_1^R\right)^{-1}. \tag{2.102}$$

Note that here all quantities are still matrices in spin space, also γ. The remaining amplitudes r_{2l}^R, t_{2l}^R, and a_{2l}^R are, up to a global sign that does not enter the scattering propabilities, obtained by swapping the indices $1 \leftrightarrow 2$. The advanced quantities are in both cases obtained by symmetry. In the case of a spin-degenerate scattering matrix the resulting physical amplitudes, as defined in Eq. (2.67), reduce to the results presented in [39].

2.3 Operator technique

An alternative way of solving the Eilenberger equation relies on three "propagator" functions U, V, W. This section follows the treatment in [38].

2.3.1 Ricatti amplitudes

By using the definitions $E^X = \varepsilon - \Sigma^X$, $\tilde{E}^X = -\varepsilon - \tilde{\Sigma}^X$, $E^K = -\Sigma^K$ and $\tilde{E}^K = -\tilde{\Sigma}^K$, we can rewrite Eq. (2.26) as

$$i\partial\gamma^X - \gamma^X \tilde{\Delta}^X \gamma^X + E^X \gamma^X - \gamma^X \tilde{E}^X + \Delta^X = 0, \quad \text{with } \gamma^X(0) = \gamma_i^X, \tag{2.103}$$

where, here and in the following, $X = R, A$ marks retarded or advanced version of the equation, and $\partial \equiv \hbar \vec{v}_F \vec{\nabla}$.
We parametrize the trajectory by the parameter ρ, defined implicitly by $\vec{R} = \vec{R}_0 + \rho \vec{v}_F$. Then, for any solution to the Eilenberger equation we find three functions $U(\rho), V(\rho),$ and $W(\rho)$, that obey the coupled equations

$$i\partial U^X + \left(E^X - \gamma^X \Delta^X\right) U^X = 0, \quad U^X(0) = \mathbb{1}, \tag{2.104}$$

$$i\partial V^X - V^X \left(\tilde{E}^X + \tilde{\Delta}^X \gamma^X\right) = 0, \quad V^X(0) = \mathbb{1}, \tag{2.105}$$

$$i\partial W^X - V^X \tilde{\Delta}^X U^X = 0, \quad W^X(0) = 0. \tag{2.106}$$

Once we have one solution γ^X and the associated operators we can replace the initial condition and obtain the new functions without having to solve the above equations again.
Assume, for instance, that we solve the Eilenberger equation for the initial condition $\gamma^X(0) = \gamma_0^X$, giving us both the full $\gamma_0^X(\rho)$ and the three functions $U_0^X, V_0^X,$

and W_0^X by explicitly solving Eqs. (2.104) - (2.106). One finds that, for (piecewise) constant potentials in a bulk s-wave superconductor that

$$U_0^X = e^{i\left(E^X - \gamma^X \tilde{\Delta}^X\right)\rho}, \tag{2.107}$$

$$V_0^X = e^{-i\left(\tilde{E}^X + \tilde{\Delta}^X \gamma^X\right)\rho} \tag{2.108}$$

$$W_0^X = \tilde{\Delta}^X D^X \left(e^{i(D^X)^{-1}\rho} - 1\right), \tag{2.109}$$

where all objects are spin-matrices, and we defined $D^X \equiv \mathrm{diag}(D_\uparrow^X, D_\downarrow^X)$ with

$$\mathcal{D}_\sigma^X \equiv \left(E_\sigma^X - \tilde{E}_{\underline{\sigma}}^X + 2\gamma_\sigma^X \tilde{\Delta}_{\underline{\sigma}}^X\right)^{-1}. \tag{2.110}$$

If we now assume a change in the initial condition

$$\gamma^X(0) = \gamma_0^X + \delta^X, \tag{2.111}$$

the "new" functions, associated to the new initial conditions, are given by

$$U^X(\rho) = U_0^X(\rho)\left[\mathbb{1} + \delta^X W_0^X(\rho)\right]^{-1}, \tag{2.112}$$

$$V^X(\rho) = \left[\mathbb{1} + W_0^X(\rho)\delta^X\right]^{-1} V_0^X(\rho), \tag{2.113}$$

$$W^X(\rho) = \left[\mathbb{1} + W_0^X(\rho)\delta^X\right]^{-1} W_0^X(\rho) = W_0^X(\rho)\left[\mathbb{1} + \delta^X W_0^X(\rho)\right]^{-1}. \tag{2.114}$$

Here we see explicitly that all we need to get the three functions is the set of "original" functions U_0^X, V_0^X, W_0^X and the change in initial condition δ^X. The main advantage with these expressions is now that we obtain the full new $\gamma^X(\rho)$ through

$$\gamma^X(\rho) = \gamma_0^X(\rho) + U_0^X(\rho)\delta^X V^X(\rho) = \gamma_0^X(\rho) + U^X(\rho)\delta^X V_0^X(\rho), \tag{2.115}$$

which means we do not have to solve either the Eilenberger equation or the operator equations again if we change the initial condition for γ^X.
The easiest way to use this technique is to use trivial initial conditions for γ_0, namely $\gamma_0^X = \gamma^X(\rho) = \gamma_{\mathrm{bulk}}^X$, which results in U_0, V_0, W_0 as defined in Eqs. (2.112) - (2.114). We can then obtain γ^X for arbitrary boundary conditions, such as the boundary conditions originating from an interface, by setting

$$\delta^X = \gamma^X(0) - \gamma_{\mathrm{bulk}}^X, \tag{2.116}$$

While the possibility to construct the general solution out of a single particular solution of Eq. (2.103) is a general property of the Ricatti equation, see also the discussion in Sect. 2.1.3, the operator technique has the additional benefit of allowing an explicit solution of the equation of motion for the distribution function x, as will be discussed in the next section.

2.3.2 Distribution function

The equation of motion for x, Eq. (2.34), can be rewritten as

$$i\partial x + (E - \gamma\tilde{\Delta})^R x - x(E + \Delta\tilde{\gamma})^A = \gamma^R \tilde{E}^K \tilde{\gamma}^A + \Delta^K \tilde{\gamma}^A + \gamma^R \tilde{\Delta}^K + E^K \equiv I^K, \quad (2.117)$$

which defines the quantity I^K. The solution to this equation is then given by

$$x(\rho) = S_U^R(\rho, 0) x(0) \tilde{S}_V^A(0, \rho) - i \int_0^\rho S_U^R(\rho, \rho') I^K(\rho') \tilde{S}_V^A(\rho', \rho) \mathrm{d}\rho', \quad (2.118)$$

which uses the operators

$$\begin{aligned} S_U^X(\rho, \rho') &\equiv U^X(\rho) \left(U^X(\rho')\right)^{-1}, \\ S_V^X(\rho', \rho) &\equiv \left(V^X(\rho')\right)^{-1} V^X(\rho). \end{aligned} \quad (2.119)$$

Once again, we obtain U_0, V_0, and W_0 for the trivial case of $\gamma^X = \gamma^X_{\mathrm{bulk}}$, and then obtain the full operators for changed boundary conditions using Eqs. (2.112) - (2.114).
In the case that only the spin-orientation along a single quantization axis is relevant to the problem we can evaluate Eq. (2.118), and obtain

$$\begin{aligned} x(\rho) = U^R(\rho) \Bigg[& x(0) - \frac{1 - e^{-i\underline{\underline{\beta_1}}\rho}}{\underline{\underline{\beta_1}}} \left(\mathbb{1} - \delta^R \tilde{\Delta}^R \mathcal{D}^R\right) I_0^K \left(\mathbb{1} - \tilde{\mathcal{D}}^A \Delta^A \tilde{\delta}^A\right) \\ & - \frac{1 - e^{-i\underline{\underline{\beta_2}}\rho}}{\underline{\underline{\beta_2}}} \delta^R \Big(\tilde{\Delta}^R \mathcal{D}^R I_0^K \tilde{\mathcal{D}}^A \Delta^A + \tilde{\Delta}^R \mathcal{D}^R \left(\gamma_0^R \tilde{E}^K + \Delta^K\right) + \left(\tilde{E}^K \tilde{\gamma}_0^A + \tilde{\Delta}^K\right) \tilde{\mathcal{D}}^A \Delta^A + \tilde{E}^K \Big) \tilde{\delta}^A \\ & - \frac{1 - e^{-i\underline{\underline{\beta_3}}\rho}}{\underline{\underline{\beta_3}}} \delta^R \left(\tilde{E}^K \tilde{\gamma}_0^A + \tilde{\Delta}^K + \tilde{\Delta}^R \mathcal{D}^R I_0^K \right) \left(\mathbb{1} - \tilde{\mathcal{D}}^A \Delta^A \tilde{\delta}^A\right) \\ & - \frac{1 - e^{-i\underline{\underline{\beta_4}}\rho}}{\underline{\underline{\beta_4}}} \left(\mathbb{1} - \delta^R \tilde{\Delta}^R \mathcal{D}^R\right) \left(\gamma_0^R \tilde{E}^K + \Delta^K + I_0^K \tilde{\mathcal{D}}^A \Delta^A \right) \tilde{\delta}^A \Bigg] \tilde{V}^A(\rho), \end{aligned} \quad (2.120)$$

where the β_i are diagonal matrices in spin space with elements given by

$$\beta_{1,\sigma} \equiv E_\sigma^R - E_\sigma^A + \gamma_\sigma^R \tilde{\Delta}_{\underline{\sigma}}^R + \tilde{\gamma}_{\underline{\sigma}}^A \Delta_\sigma^A, \quad (2.121)$$

$$\beta_{2,\sigma} \equiv \tilde{E}_{\underline{\sigma}}^R - \tilde{E}_{\underline{\sigma}}^A - \gamma_\sigma^R \tilde{\Delta}_{\underline{\sigma}}^R - \tilde{\gamma}_{\underline{\sigma}}^A \Delta_\sigma^A, \quad (2.122)$$

$$\beta_{3,\sigma} \equiv \tilde{E}_{\underline{\sigma}}^R - E_\sigma^A - \gamma_\sigma^R \tilde{\Delta}_{\underline{\sigma}}^R + \tilde{\gamma}_{\underline{\sigma}}^A \Delta_\sigma^A, \quad (2.123)$$

$$\beta_{4,\sigma} \equiv E_\sigma^R - \tilde{E}_{\underline{\sigma}}^A + \gamma_\sigma^R \tilde{\Delta}_{\underline{\sigma}}^R - \tilde{\gamma}_{\underline{\sigma}}^A \Delta_\sigma^A. \quad (2.124)$$

Here, D^X is defined in Eq. (2.110), and

$$I_0^K \equiv \gamma_0^R \tilde{E}^K \tilde{\gamma}_0^A + \Delta^K \tilde{\gamma}_0^A + \gamma_0^R \tilde{\Delta}^K + E^K. \quad (2.125)$$

A detailed derivation of this formula can be found in Appendix A. Given this formula, we can step the distribution function x from any starting point, either the bulk of a region or an interface, to any point in space. In practice, we will use this formula as a "stepping" formula from a point i to the next gridpoint $i+1$ by setting $\rho = (z_{i+1} - z_i)/v_F$ and assuming all self-energies to be equal to their values at gridpoints $i+1$.

2.4 Self-consistent nonequilibrium calculation

Lastly, we want to discuss how all the previously discussed pieces of the quasiclassical theory can be combined to perform a fully self-consistent calculation in (stationary) nonequilbrium scenarios.

2.4.1 Spin-flip self-energies

As can be seen from Eq. (2.19), self-energies enter our equations via the matrix $\check{h}$. Within the Green's function formalism, self-energies describe the effect of certain interactions on, in our cases, the single-particle Green's functions. While it is in principle possible to include several self-energies in order to include several interactions, we will limit ourselves to a single interaction, spin-flip scattering within the Born approximation. It can be written as

$$\check{h}_{\mathrm{sf}} \equiv \frac{\hbar}{2\pi\tau_{\mathrm{sf}}} \int \frac{\mathrm{d}\Omega}{4\pi} \sum_{i=x,y,z} (\hat{\alpha}_i \check{1}) \check{g} (\hat{\alpha}_i \check{1}), \tag{2.126}$$

where $\hat{\alpha}_i \equiv \mathrm{diag}\left(\sigma_i, \sigma_i^T\right)$, and τ_{sf} is the spin-flip scattering time. Since all three spin matrices are included, this form of the self-energy is also referred to as isotropic spin-flip scattering[48].

The main advantage of this type of self-energy is that it mixes the two spin channels in the diagonal components of the self-energy matrix, which leads to a decay of induced spin-currents and magnetizations, especially in normal-metal regions, and is thus the main relaxation mechanism for spin imbalances. In practice, this means that a spin imbalance induced by the spin-active interface equilibrates on a finite lengthscale on the order of $l_{\mathrm{sf}} = v_{\mathrm{F}}\tau_{\mathrm{sf}}$. We assume that the impurity scattering does not alter the type of superconducting correlations present in the system: If we start from a spin-singulet s-wave superconductor, we do not generate spin-triplet correlations through impurity scattering.

2.4.2 Charge neutrality and chemical potential

Eq. (2.38) describes a splitting of the distribution function x according to

$$x = x^{\mathrm{le}} + x^{a}. \tag{2.127}$$

The first term describes the local equilbrium,

$$x^{le} = F_0 + \gamma^R \tilde{F}_0 \tilde{\gamma}^A \equiv \tanh \frac{\varepsilon + e\phi(\vec{r})}{2T} - \gamma^R \tanh \frac{\varepsilon - e\phi(\vec{r})}{2T} \tilde{\gamma}^A, \tag{2.128}$$

with a spatially varying chemical potential and (possibly) temperature. As discussed in [49], to leading order in Δ/E_F the chemical potential is determined by

$$\phi(\vec{r}) \equiv \frac{-1}{2e} \int_{-\varepsilon_c}^{\varepsilon_c} \mathrm{d}\varepsilon \int \frac{\mathrm{d}\Omega}{4\pi} \frac{1}{8\pi i} \mathrm{Tr}\ \hat{g}^K(\vec{r}), \tag{2.129}$$

where e is the elementary charge and the trace goes over both particle-hole and spin space. This choice for $\phi(\vec{r})$ ensures that the condition

$$-2eN_F\phi(\vec{r}) \stackrel{!}{=} \rho_c(\vec{r}), \tag{2.130}$$

where ρ_c is the charge density defined in Eq. (2.47), holds, guaranteeing local charge neutrality. This choice of ϕ is used throughout all calcuations. We note here that this potential is related to the quasiparticle imbalance, while the superconducting condensate is assumed to be at zero potential. The fact that the quasiparticles potential can be different from the superconducting pair potential in nonequilibrium is also discussed in [50, 51]. It is possible to define in an analogous way

$$\phi_\sigma(\vec{r}) \equiv \frac{-1}{2e} \int_{-\varepsilon_c}^{\varepsilon_c} \mathrm{d}\varepsilon \int \frac{\mathrm{d}\Omega}{4\pi} \frac{1}{4\pi i} \left(\mathrm{Tr}_{\text{p-h}}\ \hat{g}^K(\vec{r})\right)_\sigma. \tag{2.131}$$

Here, the trace $\mathrm{Tr}_{\text{p-h}}$ is only over particle-hole space, and the spin-dependent potential ϕ_σ is determined by the respective spin-component of the remaining spin matrix. By this definition, we see that

$$\phi(\vec{r}) = \frac{1}{2}\Big(\phi_\uparrow(\vec{r}) + \phi_\downarrow(\vec{r})\Big), \tag{2.132}$$

so that the definition of ϕ_σ is consistent with the requirement of charge neutrality. For spin-degenerate problems, we thus find $\phi_\uparrow = \phi_\downarrow$, while in the case of, e.g., different transmission probabilities $D_\uparrow \neq D_\downarrow$ at an interface, the two "spin potentials" will typically be different. By comparison with Eq. (2.48), we see that since

$$M_z = -\mu_B \rho_{\sigma_z} \propto \Big(\phi_\uparrow - \phi_\downarrow\Big), \tag{2.133}$$

the presence of a finite magnetization can be seen as a difference in chemical potential for the two spin orientation for our chosen quantization axis. Note that this spin-dependent potential is only calculated as an observable after selfconsistency has been reached. We note here that the local equilbrium is defined entirely in terms of the local quantities $\phi(\vec{r})$ and T, hence x^{le} does not have to be stepped through the system. Once γ and $\tilde{\gamma}$ have been stepped, we use the stepping formula Eq. (2.120) for the anomalous part x^a only, which requires a change in the Keldysh part of the self-energies.

2.4.3 The anomalous distribution function and self-energies

The splitting of x according to Eq. (2.38) generates additional self-energies terms that enter the stepping formula. In Eq. (2.120), the replacements

$$x \to x^a, \tag{2.134}$$

$$\Delta^K \to \Delta^K + \Delta^R \tilde{F}_0 + F_0 \Delta^A, \tag{2.135}$$

$$E^K \to E^K - \Big(E^R F_0 - F_0 E^A \Big) - i\partial F_0, \tag{2.136}$$

have to be made. Effectively, the subtraction of the retarded and advanced terms means that the respective self-energy should only be computed using $g^{K,a}$ obtained by replacing x with x^a in Eq. (2.33). Here, as before,

$$F_0 \equiv \tanh \frac{\varepsilon + e\phi(\vec{r})}{2T}, \qquad \tilde{F}_0(\vec{r}) \equiv -\tanh \frac{\varepsilon - e\phi(\vec{r})}{2T}, \tag{2.137}$$

which leads to

$$-i\partial F_0 \equiv -i\vec{v}_F \Big(\nabla\mu - \frac{\varepsilon + e\phi(\vec{r})}{T(\vec{r})} \nabla T(\vec{r}) \Big) \hbar \partial_\varepsilon F_0, \tag{2.138}$$

with $\mu = -e\phi(\vec{r})$. Further details on this procedure, as well as generalizations to the time-dependent case can be found in Appendix F of [38].

2.4.4 Linear response for the normal-state distribution function

In a normal-metal region sufficiently far from a superconductor, so that the proximity effect has decayed, Eq. (2.34) simplifies to

$$i\vec{v}_F \cdot \vec{\nabla} x - \Sigma^R x + \Sigma^A x = -\Sigma^K. \tag{2.139}$$

For simplicity, we assume that the chemical potential changes only in one direction, along the z axis. Using the splitting according to Eq. (2.38) and assuming that the local gradient in ϕ is small, we can expand

$$x = x^{le} + \vec{x} \cdot \vec{v}_F = x^{le} + x_z v_F \cos\theta + \mathcal{O}\left(\vec{\nabla}\phi \right)^2, \tag{2.140}$$

where θ is the trajectory angle with respect to the z axis. In a normal region with constant impurity strength Γ, the retarded and advanced self energies in Eq. (2.139) evaluate to

$$\Sigma^R = -i\Gamma, \qquad \Sigma^A = +i\Gamma, \tag{2.141}$$

while for the Keldysh self energy we obtain

$$\Sigma^K = \frac{\Gamma}{\pi} \langle g^K \rangle_{FS} = -2\pi i \frac{\Gamma}{\pi} \langle x^{le} + x_z v_F \cos\theta \rangle_{FS} = -2\pi i \Gamma \; x^{le}. \tag{2.142}$$

Here, the angled brackets $\langle \dots \rangle$ indicte a Fermi-surface averaging. The term proportional to x_z vanishes by the antisymmetry of $\cos\theta$ after averaging over the Fermi surface, while x^{le} is independent of momentum direction. Using the ansats in Eq. (2.140) we obtain from Eq. (2.139)

$$iv_F \cos\theta(\partial_z x^{le} + v_F \cos\theta \underbrace{\partial_z x_z}_{\mathcal{O}(\vec{\nabla}\phi^2)}) + 2i\Gamma v_F \cos\theta x_z + 2i\Gamma x^{le} = 2i\Gamma x^{le}. \tag{2.143}$$

Removing the higher order term, we are left with

$$iv_F \cos\theta \partial_z x^{le} = -2i\Gamma v_F \cos\theta x_z, \tag{2.144}$$

which by Eq. (2.40) gives

$$x_z(z) = -\frac{1}{2\Gamma}\partial_z x^{le} = \frac{-e\partial_z\phi(z)}{2\Gamma}\frac{1}{2T}\frac{1}{\cosh^2\frac{\varepsilon+e\phi(z)}{2T}}. \tag{2.145}$$

In a normal-metal region with a small, constant gradient in ϕ the anomalous distribution is thus a peak of width $4T$ around $\phi(z)$ with a height proportional to $\vec{\nabla}\phi$. The charge current can be explicitly calculated using Eq. (2.50). We note here that the local-equilbrium part of the distribution does not lead to any current, and the Fermi-surface average of the linear-response x_z gives a factor of $1/3$, so that the total current reads

$$j_z = 2eN_F\frac{1}{3}v_F^2\frac{-e\partial_z\phi(z)}{2\Gamma} = 2\frac{e^2v_F^2N_F\tau}{3}\left(-\vec{\nabla}\phi(z)\right) \equiv \sigma\left(-\vec{\nabla}\phi(z)\right) \tag{2.146}$$

where we identified the average time between impurity collisions $\tau = 1/(2\Gamma)$. In linear response, the conductivity is thus given by

$$\sigma = 2\frac{e^2v_F^2N_F\tau}{3}, \tag{2.147}$$

a well-known result for semiclassical transport in three dimensions. This result could be used for a current boundary condition in the normal leads as long as the assumption of linear response is satisfied. We will, however, use a different strategy that does not require this assumption.

2.4.5 Current boundary condition for the distribution function

So far, we have discussed how the distribution function x is split up, how we can step it from one gridpoint to another, and how it behaves at a boundary within the system. However, we are still missing one key ingredient: What are the boundary values for x at the edges of our system?

By definition, x^{leq} is determined by the local chemical potential and temperature. It would thus be possible to force a certain potential (and temperature) at the

edges and assume that $x^a = 0$ there. This would correspond to potential boundary conditions. We find that while possible, this approach does not always give self-consistent solutions with conserved charge current.

What we found to give better results are current boundary conditions, and this requires us to specify a boundary value for x^a at the edge of system. To obtain this starting condition we note that, just as inside the system, the charge current at the edge is given by Eq. (2.50),

$$I^z_{c,\text{edge}} \equiv \frac{-eN_F A_c}{8\pi i} \int_{-\varepsilon_c}^{\varepsilon_c} \mathrm{d}\varepsilon \int \frac{\mathrm{d}\Omega}{4\pi} \operatorname{tr} v_F^z \hat{\tau}_3 \hat{g}^K. \tag{2.148}$$

In our case, we have normal-metal electrodes at the edges of our system. If we are sufficiently far from the central superconducting region, so that the coherence functions γ^X have decayed, $\hat{g}^K$ is simply given by

$$\hat{g}^K_{\text{normal}} = -2\pi i \begin{pmatrix} x & 0 \\ 0 & \tilde{x} \end{pmatrix}. \tag{2.149}$$

At the system edge, any induced magnetization should have decayed, so that $x_\uparrow = x_\downarrow$, and tracing over the spin degree of freedom gives an additional factor of two. For simplicity, we further assume that we only include two trajectories in our calculation, namely $v_F^z = \pm v_F$, the generalization to the full angular integration is straightforward. We can then label the two directions by $+$ and $-$, and obtain

$$I_c^z = \frac{eN_F v_F A}{2} \int_{-\varepsilon_c}^{\varepsilon_c} \mathrm{d}\varepsilon \frac{1}{2} \left[\left(x_+^{\text{leq}} + x_+^a - \tilde{x}_+^{\text{leq}} - \tilde{x}_+^a \right) - \left(x_-^{\text{leq}} + x_-^a - \tilde{x}_-^{\text{leq}} - \tilde{x}_-^a \right) \right]. \tag{2.150}$$

By symmetry, we know that $\tilde{x}_\pm(\varepsilon) = x_\mp(-\varepsilon)$, so we can simplify

$$I_c^z = eN_F v_F A \frac{1}{2} \int_{-\varepsilon_c}^{\varepsilon_c} \mathrm{d}\varepsilon \left[\underbrace{x_+^a + x_+^{\text{leq}}}_{=x_+} - \underbrace{(x_-^a + x_-^{\text{leq}})}_{=x_-} \right] \equiv I_{c,+} + I_{c,-}. \tag{2.151}$$

If we want a certain current to be incoming from the system edge, we want to enforce

$$I_c^z|_{\text{edge}} \equiv I_{c,+} + I_{c,-} \stackrel{!}{=} I_b, \tag{2.152}$$

For illustrational purposes, we assume that we are at the left edge of our system, where x_+ describes the right-flowing and x_- the left-flowing current, see Fig. 2.6.

In our scheme, x_- will be the results of stepping all functions through the entire system, so x_+ has to be changed in each iteration to satisfy Eq. (2.152).

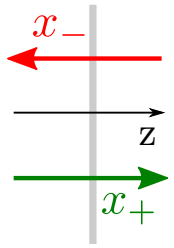

Figure 2.6: *Current flow and distribution functions x.*

In order to proceed further, we need an appropriate shape of x^a as a function of energy ε at the system edge. Our approach is to assume that at the system edge, the normal-metal region is contact-coupled to another normal-metal reservoir which is kept at a potential ϕ_j. A sketch of this is shown in Fig. 2.7.

In the reservoir, we then have

$$x_{\text{reservoir}} = \tanh \frac{\varepsilon + e\phi_j}{2T} = x^{\text{leq}}_{\text{reservoir}}. \tag{2.153}$$

We assume that the system is coupled to this reservoir with a fully transparent, spin-degenerate barrier with $D = 1$. One can show that the boundary condition, Eq. (2.58), gives for the full x_0 at the first gridpoint in the system

$$x_{0,+} = D\ x_{\text{reservoir}} = x^{\text{leq}}_{\text{reservoir}}, \tag{2.154}$$

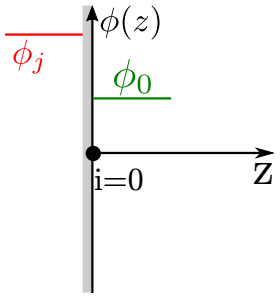

Figure 2.7: *Potentials at the system edge.*

and by the splitting according to Eq. (2.38), we find

$$x^a_{0,+} = x^{\text{leq}}_{\text{reservoir}} - x^{\text{leq}}_0 \equiv \tanh \frac{\varepsilon + e\phi_j}{2T} - \tanh \frac{\varepsilon + e\phi_0}{2T}. \tag{2.155}$$

To see how this result helps us, we can now use this shape of x^a_0 as function of energy to obtain a recipe on how to calculate ϕ_j. Rearranging Eq. (2.152), we have

$$I^z_{c,+} = I_b - I^z_{c,-},$$

and inserting Eq. (2.155) into $I^z_{c,+}$ in Eq. (2.151), we find

$$\begin{aligned} I_b - I^z_{c,-} &= eN_F v_F A \frac{1}{2} \int_{-\varepsilon_c}^{\varepsilon_c} \mathrm{d}\varepsilon\ (x^a_+ + x^{\text{leq}}_+) = eN_F v_F A \frac{1}{2} \int_{-\varepsilon_c}^{\varepsilon_c} \mathrm{d}\varepsilon\ \tanh \frac{\varepsilon + e\phi_j}{2T} \\ &= eN_F v_F A \frac{1}{2} 2T \left(\ln \cosh \frac{\varepsilon + e\phi_j}{2T} \right) \Bigg|_{-\varepsilon_c}^{\varepsilon_c} = eN_F v_F A \frac{1}{2} 2T \left(\frac{2e\phi_j}{2T} \right), \end{aligned} \tag{2.156}$$

where the limit $|\varepsilon_c| \to \infty$ was taken together with the assumption that $\phi_j \ll \varepsilon_c$. Inverting the last relation, we thus arrive at

$$e\phi_j = \frac{I_b - I_{c,-}}{eN_F v_F A}. \tag{2.157}$$

Now, for a given current $I_{c,-}$ that will be a result of the stepping procedure, we have a way of determining ϕ_j for the "incoming" function x^a that will result in a certain boundary current I_b. The same procedure is used on the the right-hand side edge of the system, where the roles of x_+ and x_- are swapped.

If we include several trajectories in the calculation and perform the angular averaging, we obtain

$$e\phi_j = \frac{I_b - I_{c,-}}{eN_F v_F A} \left(\int_0^1 \mathrm{d}\xi_F \xi_F \right)^{-1}, \tag{2.158}$$

from which we can restore Eq. (2.157) by assuming that only a single trajectory at $\xi_F = 1$ contributes to the intergral. Note that in this case we assume that all incoming trajectories contribute equally to the current at the system edges, an assumption that can easily be generalized to, e.g., a tunnel cone.

The potential drop from ϕ_J to ϕ_0 at the system edge can be interpreted in terms of a contact resistance. In our calculations, we obtain the potential profile over the entire structure, and can thus choose our voltage probe to include or exclude this contact resistance. The appropriate potential drop over the system and the corresponding resistance can then be chosen so as to match a given experimental setup.

2.4.6 Calculation scheme

Lastly, we give a short description of how all of the above elements are combined to perform calculations. We discretize our spatial coordinate z on a grid with stepsize $\Delta z = L\xi_0$, where L is a parameter by numerical considerations — finer grids give better results, but result in longer calculations since we need more points to cover the same distances. On every gridpoint, we then have the different retarded, advanced, and Keldysh self-energies Δ^X and Σ^X. Then, the procedure is as follows:

1. Update the self-energies and the chemical potential ϕ everywhere, using the recipes described in Sect. 2.1.4 and Sect. 2.4.1 - 2.4.2. As a starting guess, we assume that Δ has the bulk value everywhere in the superconducting region, and is vanishing in the normal metal. Initially, we also assume that $\phi(\vec{r})$ is identically zero everywhere.

2. Update ϕ_j on the left and right edges using Eq. (2.157). In the first iteration, the current leaving the system, for example $I_{c,-}$ on the left side, will be zero since both γ and x have not yet been stepped through the system.

3. Calculate $\gamma^X = \gamma^X_{bulk}$ and x^a, using Eq. (2.155) with ϕ_j, at the system edges.

4. Step both γ^X and x^a up to the interface separating the normal and superconducting regions. Special care has to be taken with the self-energies at interface points in the superconductor, see also the extended discussion in [43]. Calculate the functions on the respective other side of the interface, using the boundary conditions described in Sect. 2.2.1. Note that the boundary condition for the distribution function is applied to the *full* x.

5. Step all functions back to the system edges.

6. Recalculate new values for all self-energies and ϕ everywhere. If they change less then your desired accuracy, your calculation has converged. Otherwise, go back to step 1.

Throughout this thesis, our desired accuracy was that charge current is conserved to less than 0.5% relative error, meaning that the condition

$$|I(z_i) - I_b| < 5 \cdot 10^{-3}\ I_b, \tag{2.159}$$

is satisfied for all gridpoints i. A higher accuracy is possible but comes at the cost of higher numerical effort.

In our calculation, we do not perform a full Fermi-surface average, but rather include one trajectory in positive and negative direction. For the s-wave superconductors that we consider the inclusion of a larger number of trajectories is expected to have only a small effect. For the most part, the larger available phase space will lead to small quantitative changes, such as a larger critical current in the superconductor, while the qualitative features remain unchanged.

3 Charge imbalance

In this chapter, we study a hybrid system of normal metals and a superconductor that are connected via an insulating interface. The left normal lead and the superconductor are connected via an insulator with transparency D. We will refer to this normal-metal superconductor hybrid as NIS system. Of central interest to us is the transport from the left normal-metal region into the central region and the effect of the barrier.

The right interface between the central and right region is assumed to be spin-independent and fully transparent ($D = 1$). The right interface will thus not provide additional information, yet the second normal metal region is needed for us to have a well-defined problem where our current-bias boundary condition can be applied. A system with two normal "leads" is also closer to experimental setups compared to having an "infinite" superconductor or normal lead only on one side of the system.

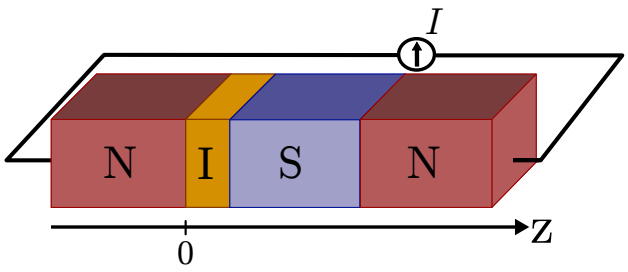

Figure 3.1: *Sketch of an normal-metal/superconductor hybrid system with an insulating barrier, that will be parametrized by a normal-state transparency D. The central S region can also be replaced by a normal conductor, referred to as NIN system.*

Additionally, we consider a system where the central region is a normal metal with the same impurity concentration as the outer two ones, to compare our results to a normal-metal (NIN) system.

As can also be seen in the figure, we impose a certain current I running through the structure. This current I corresponds to the boundary current, and we used the procedure described in Sect. 2.4 in order to enforce a certain current at the left and right edge of our system. We have to solve the Ricatti equation for the coherence function γ and the equation of motion for the distribution function x. Once we reach a self-consistent solution the total charge current across the system will be conserved. The results of our calculations are then γ^X, x, and the self-energies, including the scalar potential ϕ, at all gridpoints. We can then calculate the observables discussed in Sect. 2.1.5.

In the following, we assume a rather larger concentration of magnetic impurities in the normal regions, namely $\Gamma_{\mathrm{sf,normal}} \approx 0.125\hbar$. In the superconductor, a smaller concentration of magnetic impurities on the order of $\Gamma_{sf,SC} = 0.01\hbar$ is assumed,

which determines T_c and hence the superconduting coherence length ξ_0. We express all lengthscales in terms of ξ_0 even in the absense of a superconducting region. The fact that we use a spin-flip scattering according to Eq. (2.126), the effective mean free path gets reduced compared to single-axis spin-flip scattering. Relative to this superconducting coherence length, the mean free path in the normal metal is $l_{\text{sf,normal}} \approx 10\ \xi_0$, while in the superconductor it is on the order of $l_{\text{sf, SC}} \approx 100\ \xi_0$.

A short note on sign conventions: Throughout this thesis, all currents are specified in units of the constants in Eq. (2.50), so that we plot and specify

$$I \equiv \frac{I_c^z}{-eN_F v_F A}. \tag{3.1}$$

By this choice, a positive current, i.e., one that is flowing to the right, corresponds to electrons and Cooper pairs moving to the left and vice versa for negative current. Since we focus on one current direction throughout this thesis, this will only be relevant to the discussion of Fig. 3.13.

Lastly, we discuss some lengtscale estimates. We imagine our system to have an arbitary length along the z-axis, and a certain length w in the other two directions. In order for the quasiclassical theory to be valid, this width needs to be larger than the Fermi wavelength λ_F. Following the discussion in [52], the width should satisfy the relation

$$\lambda_F \ll w \ll \lambda, \tag{3.2}$$

where λ is the penetration depth. This condition ensures that we can neglect the Meissner effect and rather have a uniform current density throughout our system and a uniform order parameter in the transverse direction. For a type I superconductor, we further have by definition that $\lambda < \xi_0$. For a type II superconductor, where $\xi_0 < \lambda$, both the cases $w > \xi_0$ and $w < \xi_0$ are compatible with Eq.(3.2). In the former case, the current densities have to be small enough so that no vortices are created since we do not take the formation of vortices into account. Since vortices are of size ξ_0, in the latter case the system is to small to host vortices and we may in principle allow for large current densities reaching the critical current where superconductivity is destroyed.

3.1 Andreev reflection

One key concept when discussing charge transport through a N-S hybrid structure is the phenomenon of *Andreev reflection*[53]. The process has no analogue in normal metals and is thus a key feature of superconductivity.

An electron moving through a normal metal, upon reaching an perfectly transmitting interface to a superconducting region. Since the barrier is perfectly transmitting the electron cannot simply be reflected by the interface. However, since

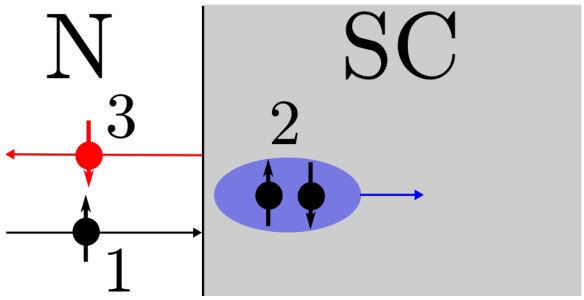

Figure 3.2: *Andreev reflection at an NS interface: When an electron in the normal metal (1) reaches a perfectly transmitting interface to a SC region, an excess Cooper pair (2) is created in the superconductor, while a hole is "reflected" back into the normal metal (3). Note that the hole will have opposite spin compared to the electron so that angular momentum is conserved in the entire process.*

for an electron with energy in the superconducting energy gap there are no single-particle states in the superconductor and it cannot be transmitted either. Instead, the electron will be Andreev-reflected: A Cooper pair will be pushed into the superconductor, while a hole with opposite momentum will be "reflected" back into the normal region. Fig. 4.2 shows a sketch of this Andreev process.

If the transmission probability D at the N-S interface is less than unity there will also be a finite probability for regular electron reflection at the interface and a corresponding reduction in probability for Andreev reflection. Impurities can also lead to regular electron transmission being allowed. We will discuss this in more detail in Sect. 3.2.

3.2 N-S interface: potential-bias description

A common description of the NIS system introduced in Fig. 4.1, which will typically neglect the self-consistency, is in terms of a potential-biased normal metal connected to the superconductor, see for example[40, 46]. This approach was pioneered by Blonder, Tinkham and Klapwijk in [28] and is often referred to as BTK approach. For better comparability of our results, it is illustrative to recap those results in our framework.

We assume that we do not calculate the order parameter self-consistently, and instead have a clean normal-metal region at a potential V, and a superconducting region with constant order parameter up to the interface. As a result, the distribution function x is naturally split into global equilbrium, see Eq. (2.38), and the anomalous part is given by

$$x^a_{1,\sigma} = \tanh \frac{\varepsilon + eV}{2T}, \qquad x^a_{2,\sigma} = 0, \tag{3.3}$$

To obtain further insight into the physics of charge transport across the interface,

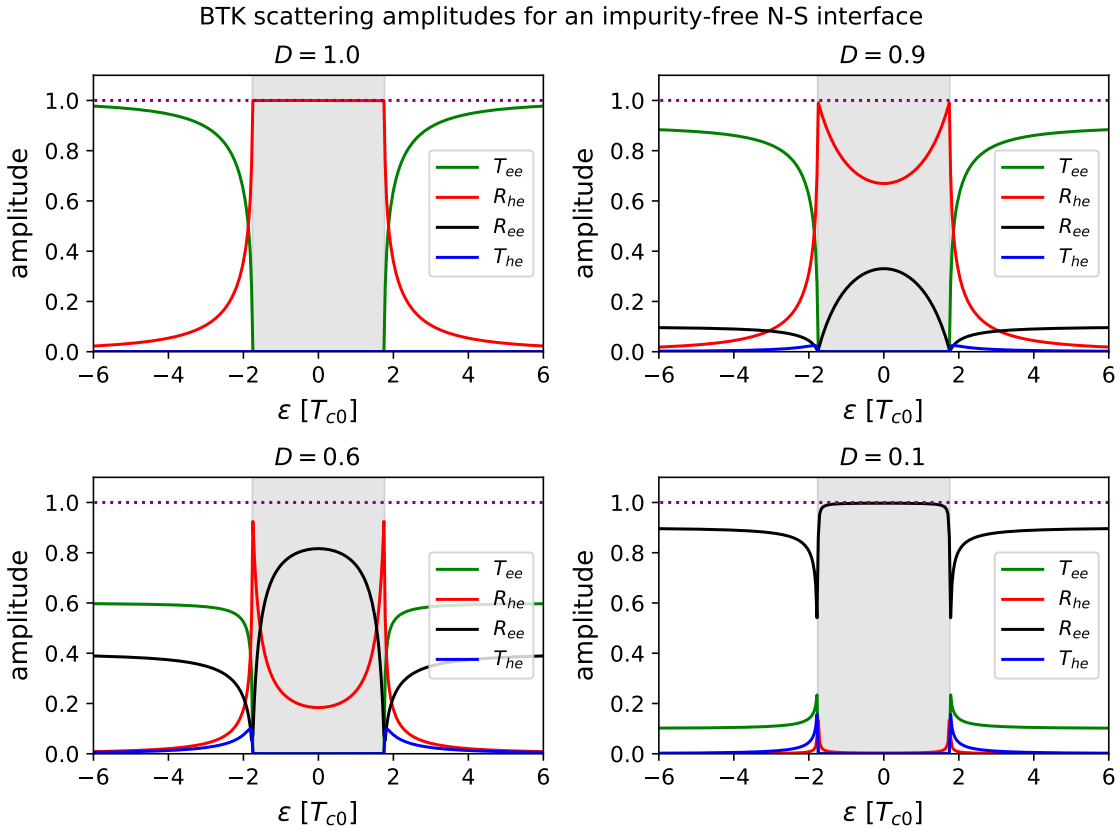

Figure 3.3: *Different physical mechanisms for charge transport at the N-S interface on the normal side. The purple-dotted horizontal line is the sum of all four contributions which has to equal unity according to Eq.* (2.77).

we start from the definition of the charge current, Eq. (2.50), and insert the Keldysh Green's function $\hat{g}^K$ at the interface.

The latter is completely determined by the incoming functions and the boundary conditions in Eqs. (2.56) - (2.58). Using the definitions given in Subsect. 2.2.1, we find for the current on the superconducting side

$$I_c^z = P_c \int_{-\varepsilon_c}^{\varepsilon_c} \mathrm{d}\varepsilon \int_0^1 \mathrm{d}\xi_F \; \xi_F \sum_{\sigma=\uparrow,\downarrow} j_\sigma^{\mathrm{SC}}(\varepsilon), \tag{3.4}$$

where $P_c = eN_F A_c v_F/8$ is the charge-current prefactor, $\xi_\mathrm{F} = \cos\theta_F$ is the z-axis angle in momentum space, and

$$\begin{aligned} j_\sigma^{\mathrm{SC}} = &\left(\bar{R}_{ee,\sigma} x_{2,\sigma}^K + T_{ee,\sigma} x_{1,\sigma}^K - T_{eh,\underline{\sigma}} \tilde{x}_{1,\underline{\sigma}}^K\right)\left(1 - \tilde{\gamma}_b^R \gamma_b^A\right) - |\tilde{\mathcal{G}}_{+,\sigma}^R|^2 \tilde{x}_{2,\sigma}^K - \bar{R}_{eh,\underline{\sigma}} \tilde{x}_{2,\underline{\sigma}}^K \\ &+ \left(\bar{R}_{hh,\sigma} \tilde{x}_{2,\sigma}^K + T_{hh,\sigma} \tilde{x}_{1,\sigma}^K - T_{he,\underline{\sigma}} x_{1,\underline{\sigma}}^K\right)\left(1 - \gamma_b^R \tilde{\gamma}_b^A\right) - |\mathcal{G}_{-,\sigma}^R|^2 x_{2,\sigma}^K - \bar{R}_{he,\underline{\sigma}} x_{2,\underline{\sigma}}^K. \end{aligned} \tag{3.5}$$

The normal-side current can be obtained by swapping the indices 1 and 2, the bar-symbol on all physical amplitudes and setting $\gamma_b^X = 0$, $\mathcal{G}^X = \mathbb{1}$. The current

can be written in a similiar fashion as in Eq. (3.4), with j_σ^{SC} replaced by j_σ^{N}, which can be written as

$$\begin{aligned} j_\sigma^{\mathrm{N}} = &\left(R_{ee,\sigma} x_{1,\sigma}^K + \bar{T}_{ee,\sigma} x_{2,\sigma}^K - \bar{T}_{eh,\underline{\sigma}} \tilde{x}_{2,\underline{\sigma}}^K\right) - \tilde{x}_{1,\sigma}^K - R_{eh,\underline{\sigma}} \tilde{x}_{1,\underline{\sigma}}^K \\ &+ \left(R_{hh,\sigma} \tilde{x}_{1,\sigma}^K + \bar{T}_{hh,\sigma} \tilde{x}_{2,\bar{\sigma}}^K - \bar{T}_{he,\underline{\sigma}} x_{2,\underline{\sigma}}^K\right) - x_{1,\sigma}^K - R_{he,\underline{\sigma}} x_{1,\underline{\sigma}}^K. \end{aligned} \tag{3.6}$$

The current expressions given here are also discussed in [47], and the amplitudes can be related to the coefficients A (=R_{he}), B (= R_{ee}), C (= T_{ee}), D (=T_{he}) in [28]. While the total current is determined by the voltage on the normal side of the interface, the scattering amplitudes thus specify how much each physical mechanism is contributing to the charge transport across the interface. Fig. 3.3 shows the amplitude for spin-up electrons as function of energy.

For full transparency, $D = 1$, the only available transport channel for an incoming electron in the subgap region is Andreev reflection (R_{he}), as discussed in Sect. 3.1, while electron transmission (T_{ee}) and reflection (R_{ee}) are fully suppressed. For finite transparency, regular electron reflection becomes more and more dominant, and approaches unity for $D \to 0$ where transport becomes blocked. For any finite D, electrons incoming with a subgap energy are always able to Andreev-reflect resulting in charge transport across the interface by an Andreev-reflection process.

The scattering amplitudes change in a self-consistent calculation with impurities, shown in Fig. 3.4 for a small impurity concentration in equilibrium.

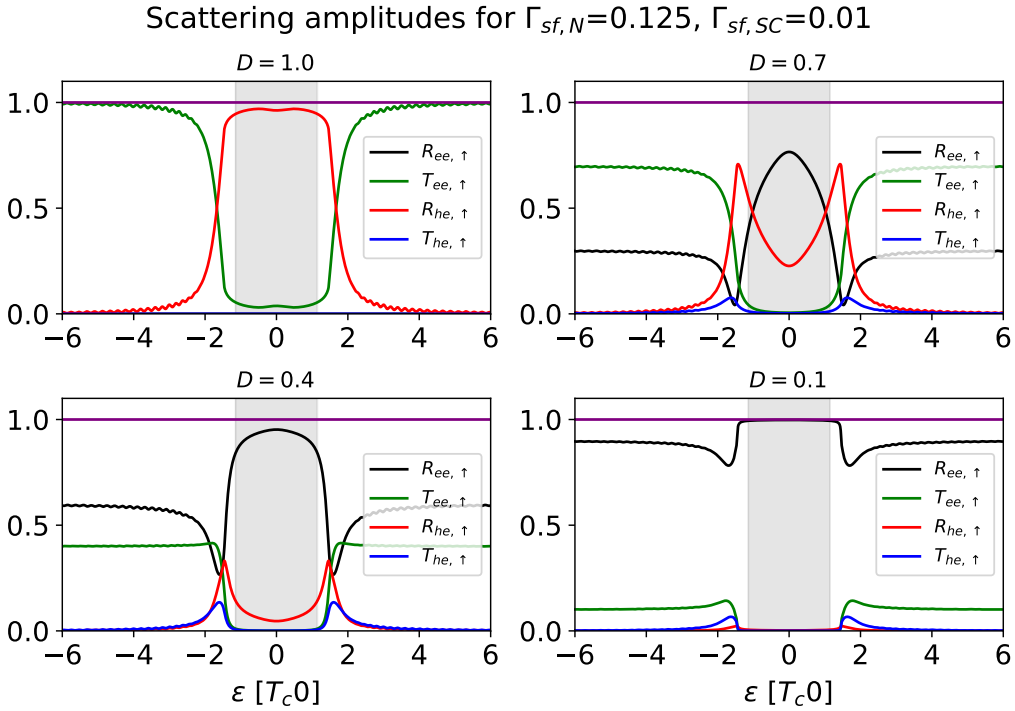

Figure 3.4: *Physical scattering amplitudes on the normal side for a small impurity concentration in the SC. The purple horizontal line is the sum of all four contributions which is equal unity by current conservation.*

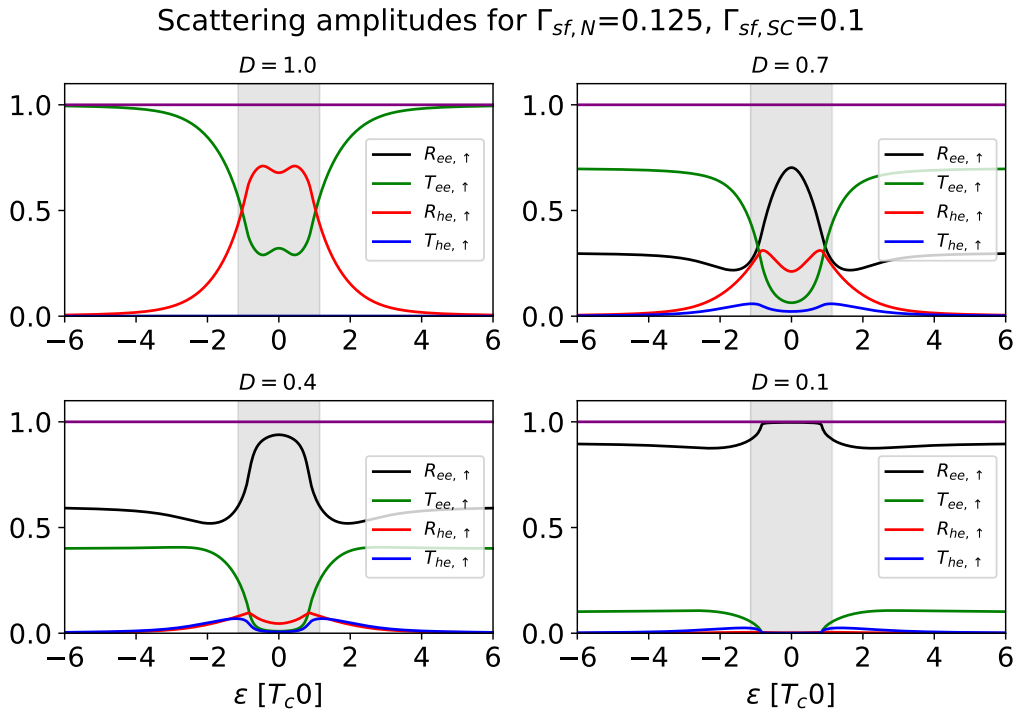

Figure 3.5: *Physical scattering amplitudes on the normal side for a high impurity concentration in the SC. The purple horizontal line is the sum of all four contributions which is equal unity by probability current conservation.*

For large transparencies, the large effect of the regular and inverse proximity effect introduce a finite probability for electron tunneling, T_{ee}, into the superconductor that is forbidden in the impurity-free BTK result shown in Fig. 3.3. In contrast, the scattering amplitudes remain largely unchange for small transparencies where the proximity effect is suppressed. For large impurity concentration, this effect becomes even more pronounced, see Fig. 3.5. For the potential-bias scenario described in Eq. (3.3), only x_1 will depend on the applied voltage V. After removing all hole terms by an energy transformation, we can obtain the normal-side interface conductance

$$G(V) \equiv \left.\frac{dI}{dV}\right|_V = e4P_c \int_0^1 d\xi_F \xi_F \int_{-\varepsilon_c}^{\varepsilon_c} \frac{d\varepsilon}{2T} \Big(1 + R_{he}(\varepsilon) - R_{ee}(\varepsilon)\Big) \cosh^{-2} \frac{\varepsilon + eV}{2T}, \quad (3.7)$$

where the factor 4 captures both the spin-doubling as well as the doubling from hole contributions. By Eq. (2.77), this can be rewritten as

$$\frac{G(V)}{G_0/e} = \int_0^1 d\xi_F \xi_F \int_{-\varepsilon_c}^{\varepsilon_c} \frac{d\varepsilon}{2T} \Big[2R_{he} + T_{ee}(1 - |\tilde{\gamma}^R|^2) + T_{he}(1 - |\gamma^R|^2)\Big] \cosh^{-2} \frac{\varepsilon + eV}{2T}, \quad (3.8)$$

where $G_0 = e^2 N_F v_F A_c$. This result is identical to Eq. (24) in [28].

In the normal state, only T_{ee} is nonzero, and we have $T_{ee} = D$ independent of energy as a consequence of our energy-independent scattering matrix in Eq. (2.79).

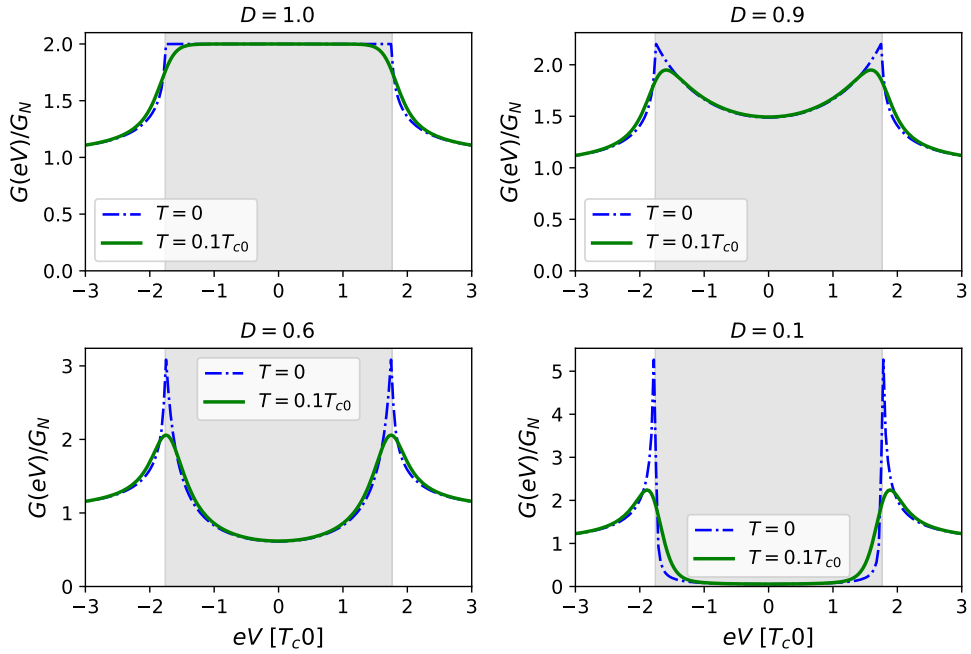

Figure 3.6: *Normalized differential conductance at the NS-interface for $T = 0$ and $T = 0.1\ T_{c0}$. The grey area marks the superconducting energy gap.*

If we only include one trajectory in our Fermi surface average, the normal-state conductance is then $G_N = e^2 N_F v_F A_c D/2$. The voltage-dependent conductance at the interface can be expressed in terms of the normal-state conductance as

$$\frac{G(V)}{G_N/e} = \frac{1}{D}\int_{-\varepsilon_c}^{\varepsilon_c} \frac{d\varepsilon}{2T}\Big[2R_{he} + T_{ee}(1-|\tilde{\gamma}^R|^2) + T_{he}(1-|\gamma^R|^2)\Big]\cosh^{-2}\frac{\varepsilon + eV}{2T}. \quad (3.9)$$

For zero temperature, the function $\cosh^{-2}$ reduces to a δ-distribution around $\varepsilon = eV$ and the integration can be performed analytically, while for finite temperatures an energy window of width $4T$ around eV contributes to the conductance, resulting in a broadening of all zero-temperature features.

A plot of the normalized conductance for zero temperature, reproducing the results in [28], and finite temperature $T = 0.1\ T_{c0}$ are shown in Fig. 3.6. Importantly, the conductance in the subgap region is twice that of the normal state for full transparency as a result of Andreev reflection. In contrast, the supgap conductance gets increasingly suppressed for smaller transparencies.

3.3 Normal metal (NIN system)

In a system consisting only of normal-metal regions, the order parameter Δ, and hence the coherence functions γ, are zero everywhere.

The transport information is thus carried exclusively by the distribution function x. We show the chemical potential ϕ as function of spatial coordinate z for different

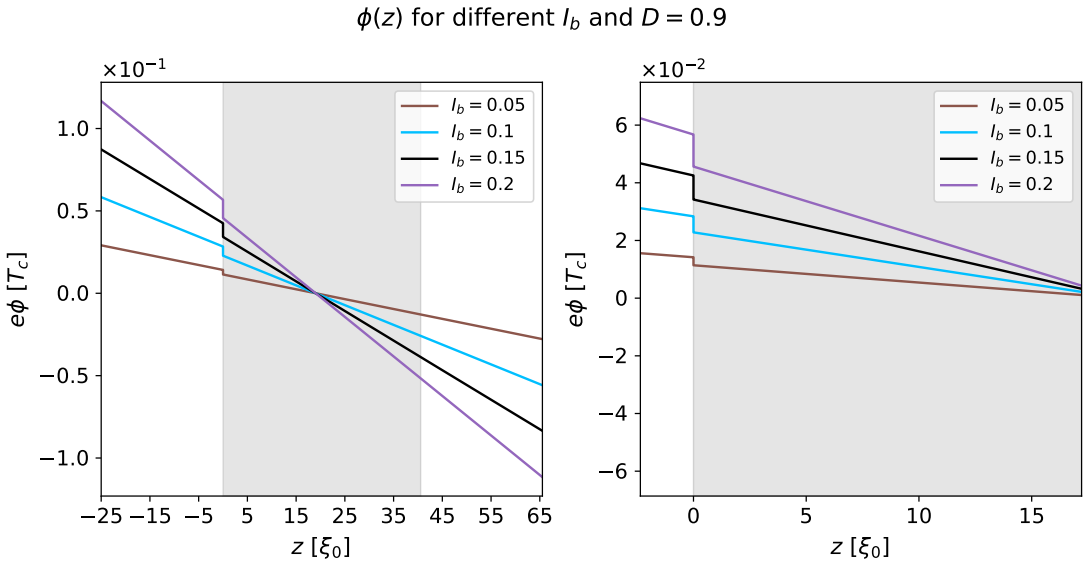

Figure 3.7: *Chemical potential $\phi(z)$ for the normal-metal system with a left-interface transparency $D = 0.9$. Left: $\phi(z)$ over the whole range of the system. Right: Enlargement of the interface region with the potential jump. The grey area marks the "central" region between the interfaces.*

boundary currents I_b at a transparency $D = 0.9$ in Fig. 3.7 and for $D = 0.3$ in Fig. 3.8. Within each normal region, the electrochemical potential ϕ, Eq. (2.129), is typically a linear function with the slope determined by the conductivity that, in turn, is determined by the mean free path. Different transparencies at the barrier lead to jumps in the chemical potential of different magnitude at the interface.

The potential drop $\Delta\phi$ at the interface depends on the boundary current I_b even for constant transparency D of the barrier. However, we can calculate the interface resistance R_I, defined by

$$R_I = \left| \frac{\phi_R - \phi_L}{I_b} \right|, \tag{3.10}$$

where ϕ_L and ϕ_R are the potential to the left and right of the barrier, respectively, and I_b is the boundary current we enforce. We find that R_I is independent of the current since our normal-state scattering matrix in Eq. (2.79) is energy-independent. Fig. 3.9 shows the dependence of R_I on the transparency D of the barrier.

As discussed in Sect. 3.2, the interface conductance is independent of the bias current and proportional to the interface transparency, $G \propto D$. The resistance R_I can be interpreted as an inverse conductance, and shows a corresponding increase $R_I \propto 1/D$. Notice that, in contrast to the potential-bias description in Sect. 3.2, there is no potential drop *at the interface* in the case of full transparency, and hence we have vanishing resistance there. Our results are in agreement with a

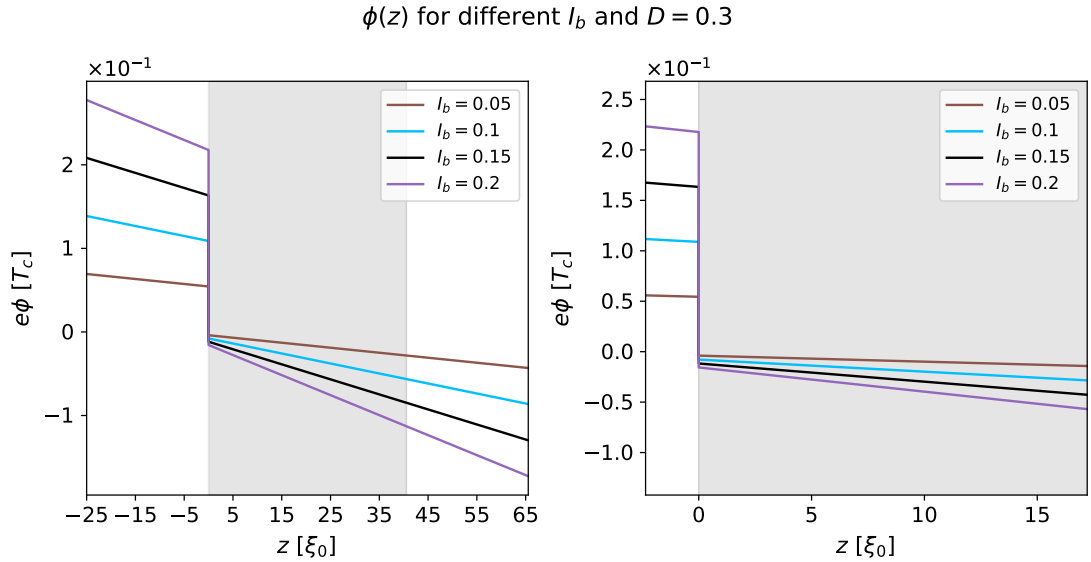

Figure 3.8: *Chemical potential $\phi(z)$ for the normal-metal system with a left-interface transparency $D = 0.3$. Left: $\phi(z)$ over the whole range of the system. Right: Enlargement of the interface region with the potential jump. The grey area marks the "central" region between the interfaces.*

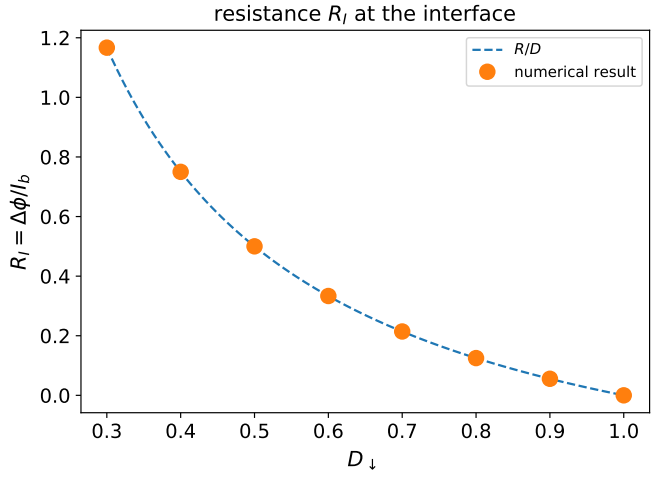

Figure 3.9: *Resistance R_I at the interface for different transparency D.*

conductance of

$$G/G_0 = \frac{D}{R}, \tag{3.11}$$

which gives a resistance of

$$R/R_0 = \frac{R}{D} = \frac{1}{D} - 1. \tag{3.12}$$

A discussion of different possible definitions of conductances can be found in, e.g., [54, 55]. According to [56], our conductance corresponds to a conductance comparing the current to the *momentum-averaged* chemical potential to the left and right of the interface. This is reasonable given our definition of the chemical potential, Eq. (2.129), which averages over the Fermi surface.

3.4 Superconductor (NIS system)

Once the central region of our system becomes superconducting, entirely new physics appear in the calculation. The splitting of the distribution function x according to Eq. (2.38) gives a natural splitting of the current, Eq. (2.50), according to

$$j = j^a + j^{\mathrm{le}}. \tag{3.13}$$

We have seen that in a normal metal the flow of a charge current requires a gradient in the potential ϕ. In a normal-metal region without superconducting correlations, the current is thus entirely determined by the anomalous part of the distribution function, x^a.

This is not the case in the bulk of a superconductor, where the charge current is carried by the superconducting condensate instead. This motion of the condensate is described by the presence of the so-called superflow $\vec{p}_s$, which gives rise to a current that is carried by x^{leq}. In a superconductor to a normal-metal interface both quantities typically coexist, as we will see shortly. First, we study the case of full transparency of the interface, $D = 1.0$, between the left normal region and the superconductor.

In Fig. 3.10, we see the chemical potentials ϕ. In the normal region, the chemical potential is approximately linear since the current is linked to a gradient in ϕ. Note that, caused by the proximity effect, the linear gradient in the entirely normal region starts to bend towards the interfaces.

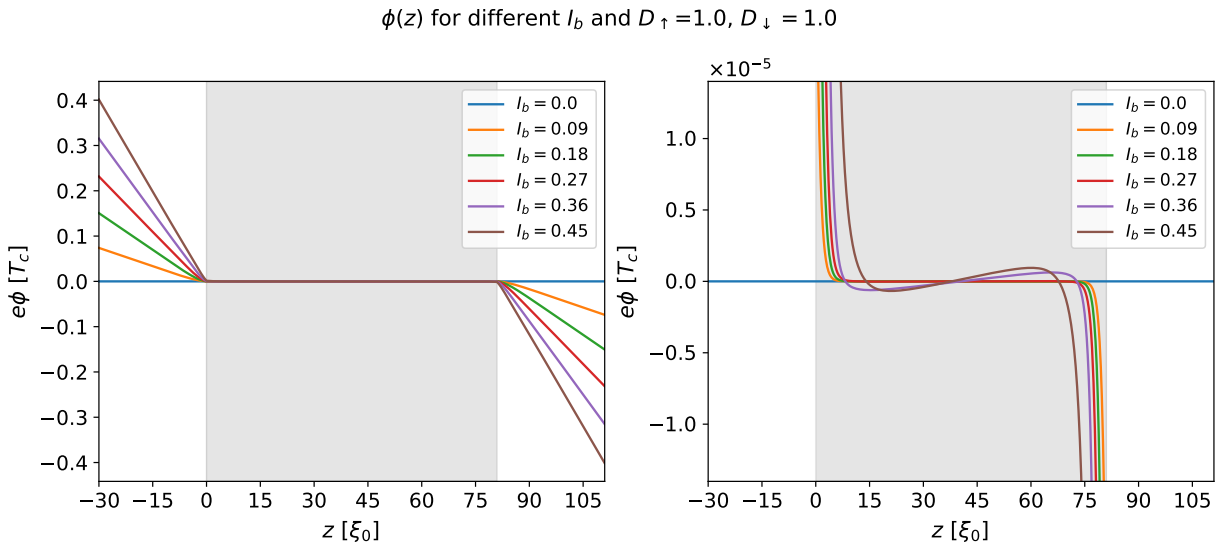

Figure 3.10: *Chemical potential $\phi(z)$ for the spin-degenerate NIS system with a left-interface transparency $D = 1.0$. Left: $\phi(z)$ over the whole range of the system. Right: Enlargement of the central superconducting region. The grey area marks the superconducting region.*

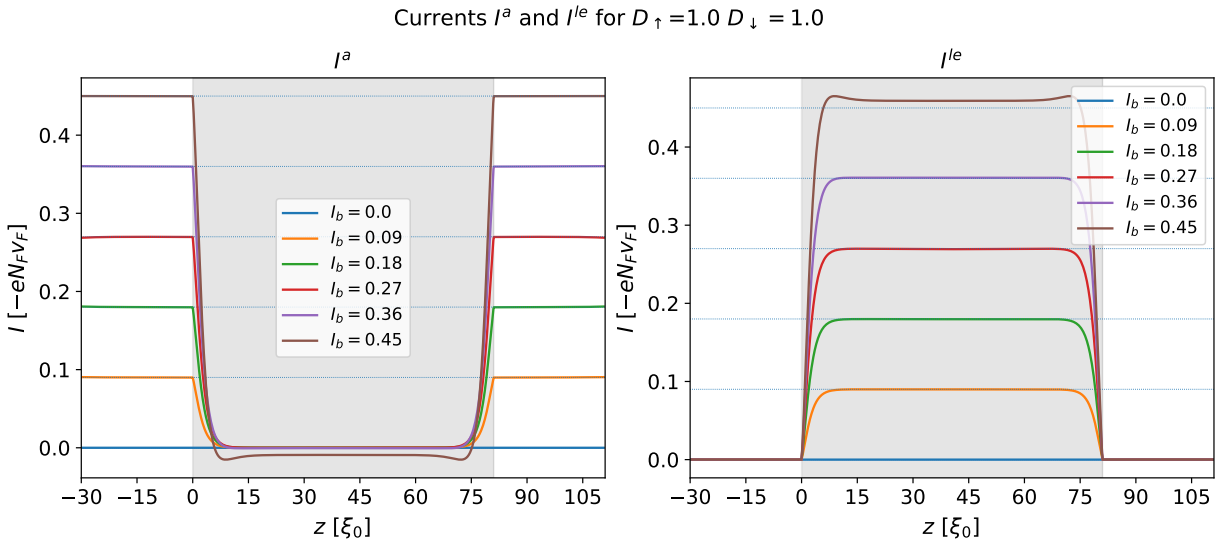

Figure 3.11: *Conversion from normal-state "anomalous" current into supercurrent over the system. The dotted lines show the respective boundary current.*

In the superconducting region, the chemical potential is strongly suppressed and, for small currents, vanishing exponentially towards the bulk. For a large current, here in the case of $I_b = 0.45$, we see a constant non-vanishing chemical potential in the entire superconductor. This indicates a non-vanishing charge imbalance that we will discuss in more detail in the following. The spatial behaviour of the two currents, j^a and j^{leq}, can be seen in Fig. 3.11.

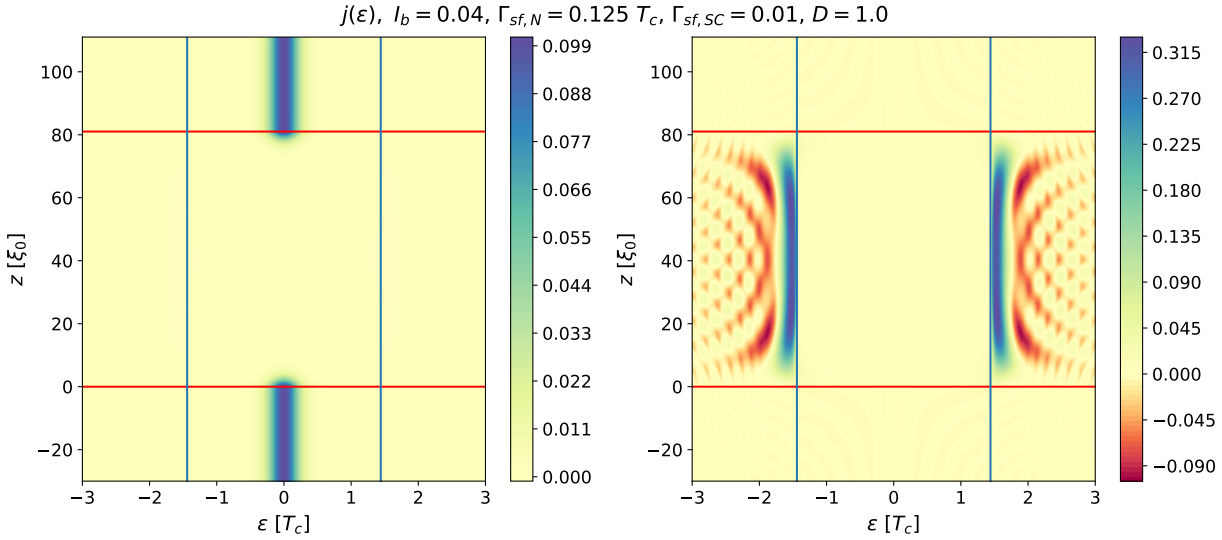

Figure 3.12: *Current density for a small current in the NSN system. Left: anomalous current, right: local-equilibrium current. Red horizontal lines indicate the beginning of the superconducting region, while blue vertical lines indicate the value of the bulk order parameter.*

In the normal regions at the system edges we start with completely "anomalous" current. This current is exponentially falling off in the superconducting region while the "local-equilbrium" supercurrent builds up until the current is entirely carried by superflow in the bulk of the superconductor.

Further insight can be won by studying the energy-resolved spectral current density $j_\varepsilon(\varepsilon, z)$, given by the energy-dependent current kernel

$$I(z) = \int_{-\varepsilon_c}^{\varepsilon_c} \mathrm{d}\varepsilon\ j_\varepsilon(z, \varepsilon)\ d\varepsilon. \tag{3.14}$$

Note that in contrast to the usual expressions in literature, such as [46], our current density *includes* the distribution function x, in contrast to a potential-bias description where factoring the trivial distribution function out is more meaningful. The spectral current densities, split again into anomalous and local-equilibrium part, for a small current is shown in Fig. 3.12. Based on the discussion in Sect. 3.2, the dominant transport channel for particles in the subgap is Andreev reflection. In the fully self-consistent calculation with impurities, there is also a finite transmission probability, and the anomalous current entering the superconductor dies out over a lengthscale determined by ξ_0. The supercurrent builds up over the same lengthscale in the region between the lower red, horizontal line and $5\xi_0$. The fact that the Andreev reflection is not a fully localized reflection process but rather consists of evanascent electron waves entering the superconductor is also discussed in, e.g., [14].

Note that the oscillations visible in the local-equilibrium current, the right plot in Fig. 3.12, are so-called Tomasch oscillations[57], a phenomenon that is caused by interference between quasiparticles interacting with the superconducting condensate[58].

In the normal metal far away from the superconductor, the current is carried only by the anomalous part. We had seen in Fig. 3.8 that the slope of the potential gradient in the normal metal increases for larger currents. In the current density, larger currents thus widen the energy-window in which current is carried.

Once we get to larger currents in Fig. 3.11, see the case of $I_b = 0.45$, we observe an "overshooting" behaviour of the anomalous current: The anomalous current does not fall off to zero but rather becomes negative, indicating a backflow of quasiparticle current that is compensated by increased superflow. This backflow is caused by two effects. Firstly, superflow will alter the density of states, since particles with (against) the superflow will experience energy-shifts in opposite directions, captured in the subsitution

$$\varepsilon \to \varepsilon - \vec{v}_F \cdot \vec{p}_S, \tag{3.15}$$

used in the presence of superflow $\vec{p}_s$. In analogy to Eq. 2.46, we define the momentum-resolved density of states by

$$N_{R(L)}(\varepsilon, \vec{r}) = \mp \frac{N_F}{2\pi} \operatorname{Im} \int_0^{\pm 1} \frac{d\xi_F}{2} \operatorname{tr} \hat{\tau}_3 \hat{g}^R(\varepsilon, \vec{r}), \tag{3.16}$$

where R (L) refers to right-moving (left-moving) particles. We show this momentum-resolved density of states for the case of $I_b = 0.44$, together with the (degenerate) equilibrium case, in Fig. 3.13.

As expected from our negative, i.e., left-flowing superflow $\vec{p}_S$, the left-moving particles get shifted down in energy while the right-moving ones get shifted up. Additionally, the bulk spectral gap gets reduced in the presence of superflow compared to the zero-current equilibrium case.

Secondly, in the case of large currents the energy window that contributes to transport is wide enough for quasiparticle states above the superconducting energy gap to get occupied. As we can see in Fig. 3.13, the first available quasiparticle states will be predominantly right-movers together with left-moving quasiholes at negative energies. Both combined lead to a net flow of negative charge to the right. By our sign convention for the current, Eq. (3.1), the positive current we enforce corresponds to left-moving negative charge, so that the right-moving quasiparticles corresponds to a current flow in the opposite direction. Note that this "backflow" of quasiparticle current is compensated for by addtional pair flow that is carried by x^{le}, as can be seen in Fig. 3.11. In the spectral current density for such a large current, Fig. 3.14, this quasiparticle backflow can be explicitly seen to survive through the entire superconducting region.

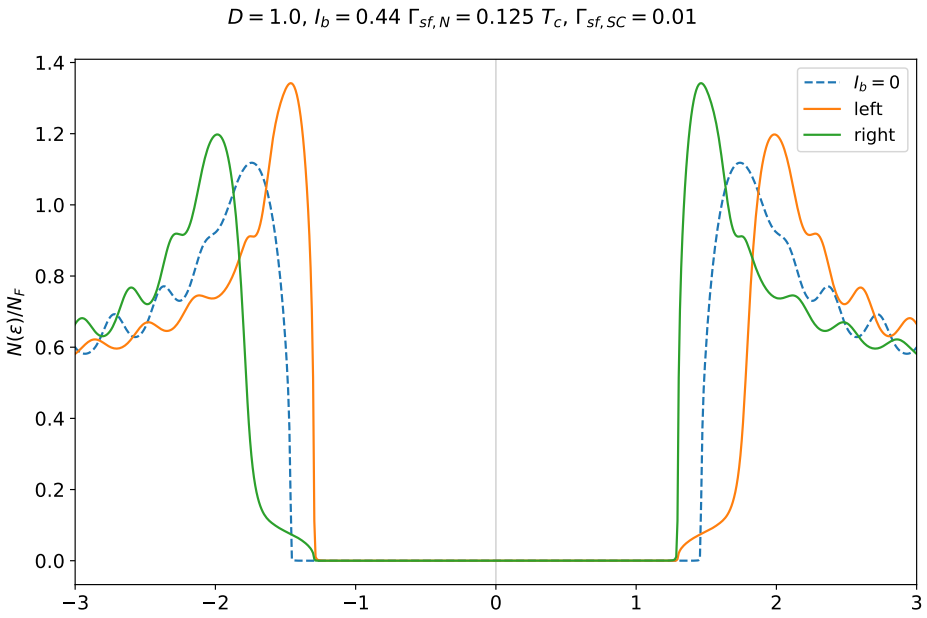

Figure 3.13: *Momentum-resolved density of states in the presence of superflow for* $I_b = 0.44$.

The occupation of quasiparticle states above the gap then explains the non-vanishing chemical potential, or charge imbalance, everywhere in the superconductor. Quasiparticles entering from the normal metal with subgap energies eventually get converted into superflow by Andreev reflection.

The fact that the charge imbalance does not decay for quasiparticles above the gap is, in some sense, expected.

A decay of this charge imbalance requires energy relaxation of quasiparticles via inelastic scattering processes. In our model, we assume that the size of the central superconducting region, L, is much less than the lengthscale of inelastic scattering, $L \ll l_{in}$, so that energy relaxation does not happen. We note that inclusion of inelasctic scattering, for example via electron-phonon coupling, is also referred to as the strong-coupling regime and discussed in, e.g., [59].

In Fig. 3.15, we show the order parameter and the bulk p_s for the currents discussed above. Since we are far from the critical current, Δ remains largely unaltered by the current flow, and p_s grows linearly with the enforced current.

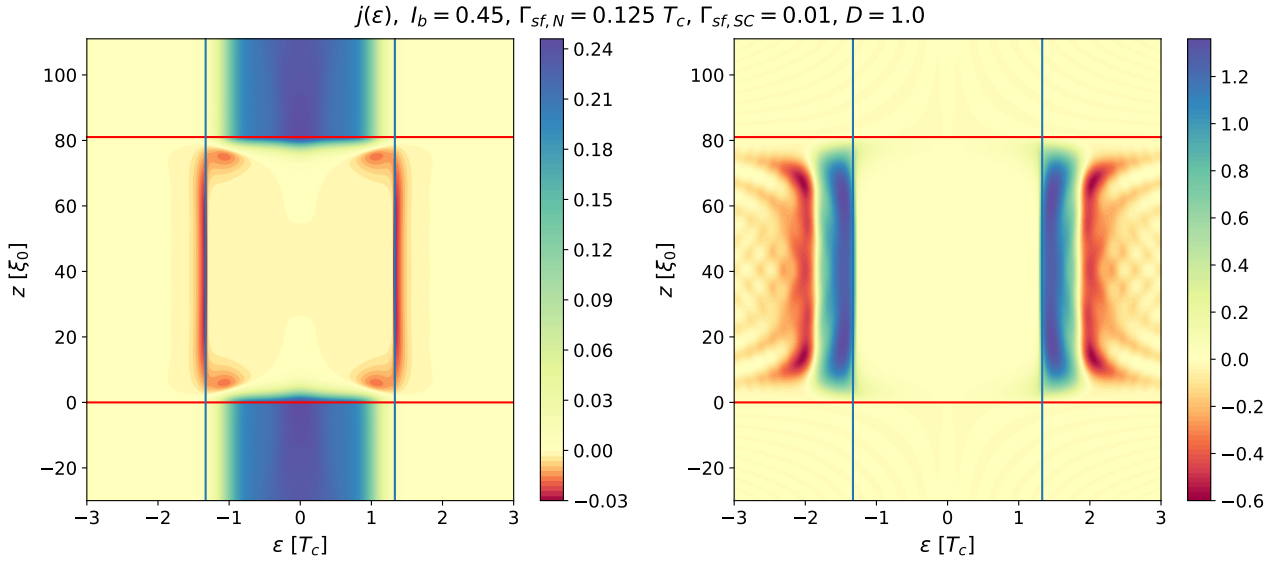

Figure 3.14: *Current density for a large current in the NIS system. Left: anomalous current, right: local-equilibrium current. Red horizontal lines indicate the beginning of the superconducting region, while blue vertical lines indicate the value of the bulk spectral gap.*

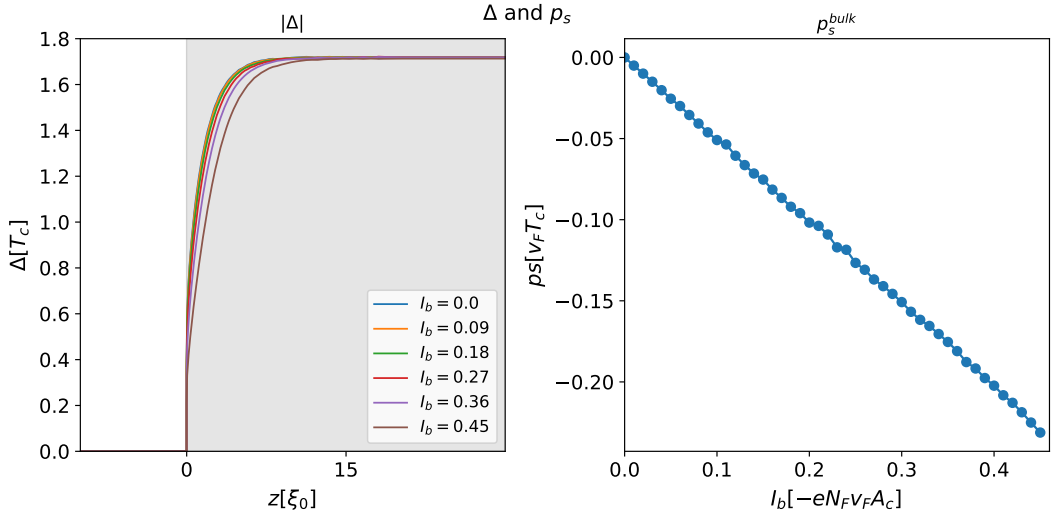

Figure 3.15: *Spatial dependence of the order parameter (left) and bulk value of the superflow p_s (right) for small currents and transparency $D = 1$.*

We see that for higher currents, the superconducting order parameter Δ starts to be suppressed by the increasing value of p_s in the bulk. If we increased the current even more the superconducting region would become normal at a critical current. We note here that within our time-independent theory, this phase-transition area cannot be properly treated. Since we have a rather small impurity concentration

in the superconductor, the transition to a normal metal is rather sharp, and we do not find $\vec{p}_S$ to exhibit any non-linearity one in the vicinity of the critical current but rather an abrupt phase transition where our calculations break down.

We expect that two strategies would allow for a larger critical current and hence larger current bias. Firstly, the discussed energy-relaxation mechanisms should be included. Secondly, a full angular average over the Fermi surface should be performed instead of our simplified one-trajectory model. Thirdly, the interfaces between the N and S region should be replaced by a tunnel barrier depending on the momentum orientation, such as in [40], effectively allowing current to be carried only by a range of trajectories. In this case, the superconducting order parameter should be suppresed less by the current, resulting in a higher critical current.

For smaller transparencies, we observe larger potential jumps at the interface and find that both the critical current and the "overshooting" behaviour is reached already for smaller currents. An illustrative example, for $D = 0.5$, is shown in Fig. 3.16. Similiar to before, we see that the anomalous current gets converted into supercurrent, but in comparison to the full-transparency case, the onset of the "overshooting" behaviour happens at smaller currents. This is can be understood by considering the chemical potential, seen in Fig. 3.17. The reduced interface conductance enforces a larger potential drop at the interface compared to the case of high D. For equal currents, the energy window participating in transport is thus larger, resulting in an occupation of quasiparticle states at lower currents. Similiarly, the superconducting region becomes normal at a lower bias current.

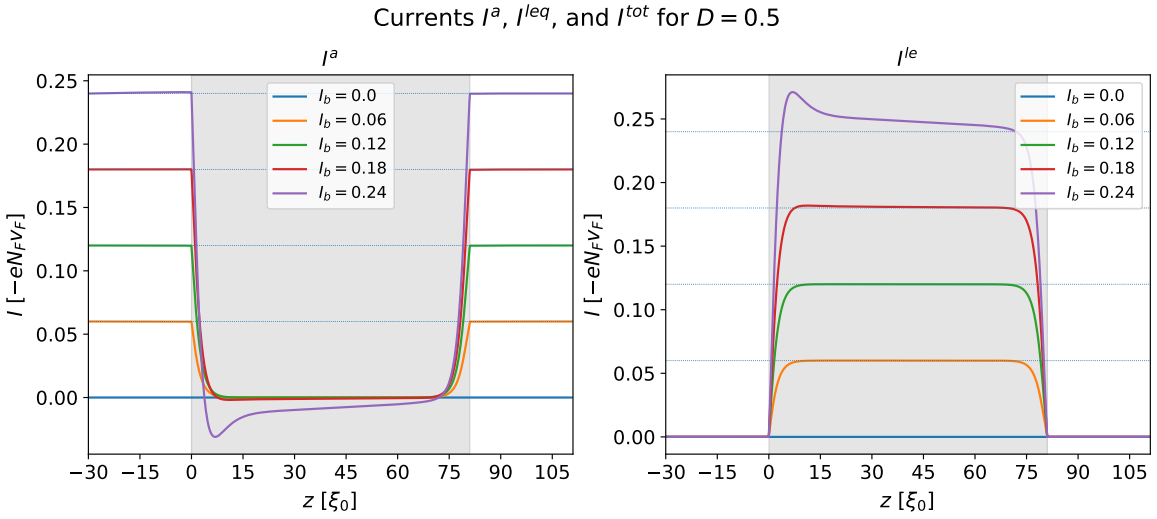

Figure 3.16: *Conversion from normal-state "anomalous" current into supercurrent over the system with a left-interface transparency $D = 0.5$. The dotted lines show the respective boundary current.*

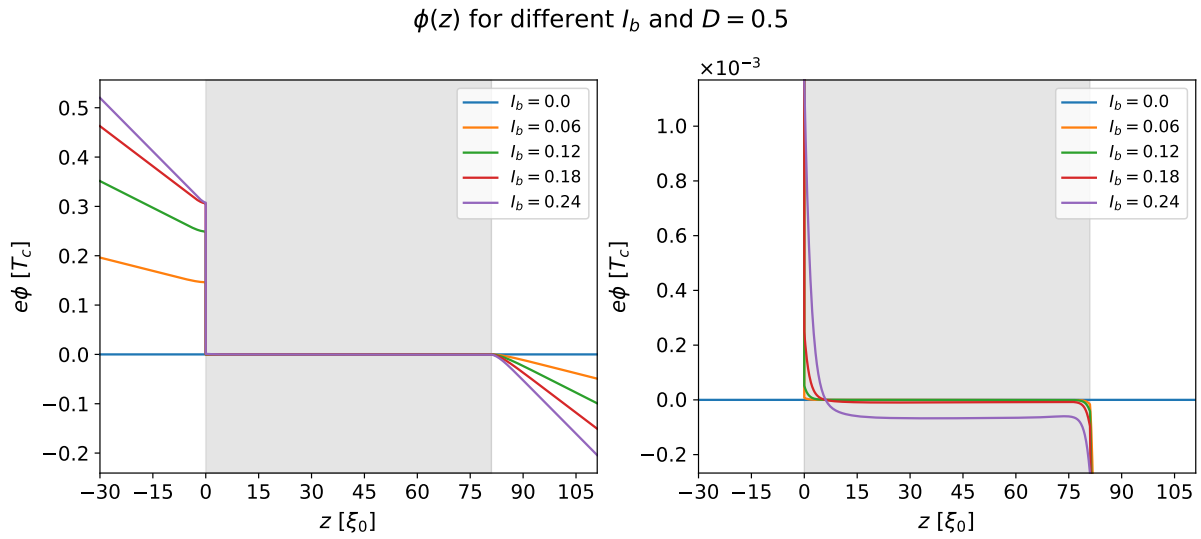

Figure 3.17: *Chemical potential $\phi(z)$ for the NIS system with a left-interface transparency $D = 0.5$. Left: $\phi(z)$ over the whole range of the system. Right: Enlargement of the central superconducting region.*

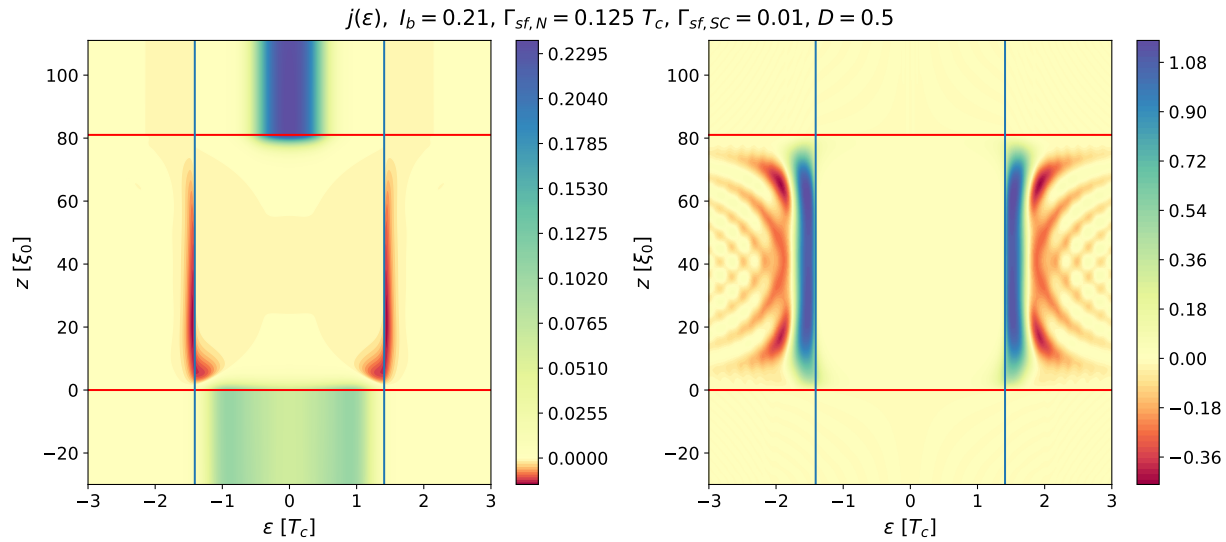

Figure 3.18: *Current density for a large current in the NIS system with a left-interface transparency $D = 0.5$. Left: anomalous current, right: local-equil. current. Red horizontal lines indicate the beginning of the superconducting region, while blue vertical lines indicate the value of the bulk order parameter.*

The effect of the lower interface conductance can also be seen directly in the current density. It is more evenly spread out over a wider energy range in the normal metal, as seen in Fig. 3.18.

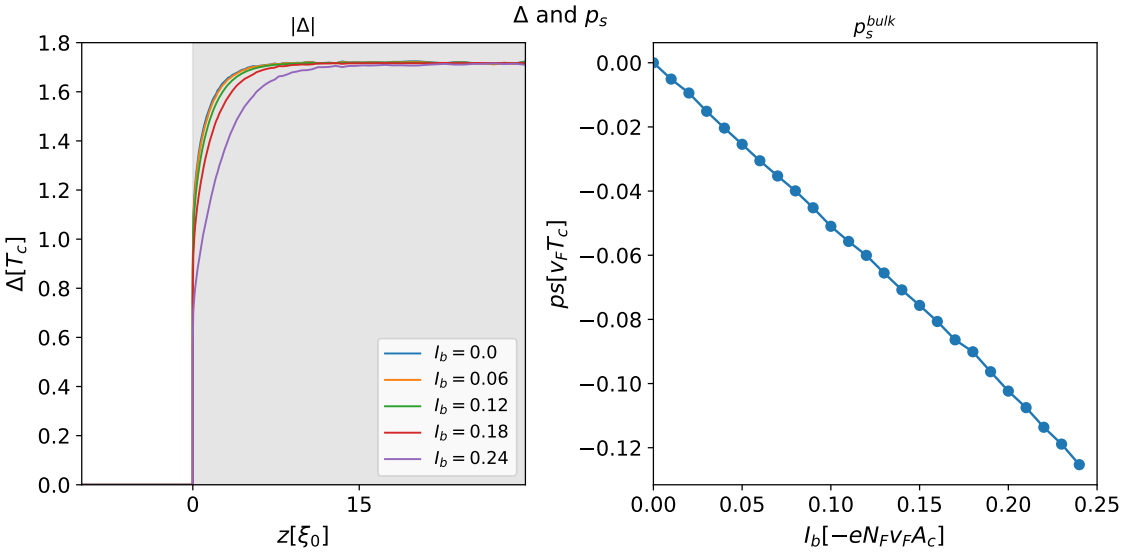

Figure 3.19: *Spatial dependence of the order parameter (left) and bulk value of the superflow p_s (right) for small currents with a left-interface transparency $D = 0.5$*

Note especially how the current density on the upper side of the left plot, corresponding to the right normal lead, is a narrower and higher-peaked function compared to the normal side with the finite interface resistance. Similiarly to occupying continuum states, the order parameter gets suppressed for smaller currents compared to the large-transparency case, as seen in Fig. 3.19. Already for a current of $I_b = 0.2$, we see a larger suppression of the order parameter compared to the same current in 3.15. Note also that the superflow in the bulk p_s required for a certain current does not depend on the interface transparency, as would be expected.

We observe that, compared to a large transparency, a larger energy window is needed for a low-transparency interface to enforce the same current through the structure. This has two effects. Firstly, quasiparticle states becomes occupied already at smaller currents. Secondly, we inject quasiparticles over the entire superconducting energy gap at lower currents compared to the high-transparency case and hence reach the critical current at a smaller current.

Lastly, we can consider the case of transparency that is closer to the tunneling limit, $D = 0.2$. We show the a range of currents for this case in Fig. 3.20. As we can see, already for a small current of $I = 0.05$ we start to occupy continuum states, compared to the full-transparency case where such behaviour only occured at $I = 0.4$. This indicates that a wide energy window contributes to transport even for small currents, which is consistent with the potential observed in Fig. 3.21.

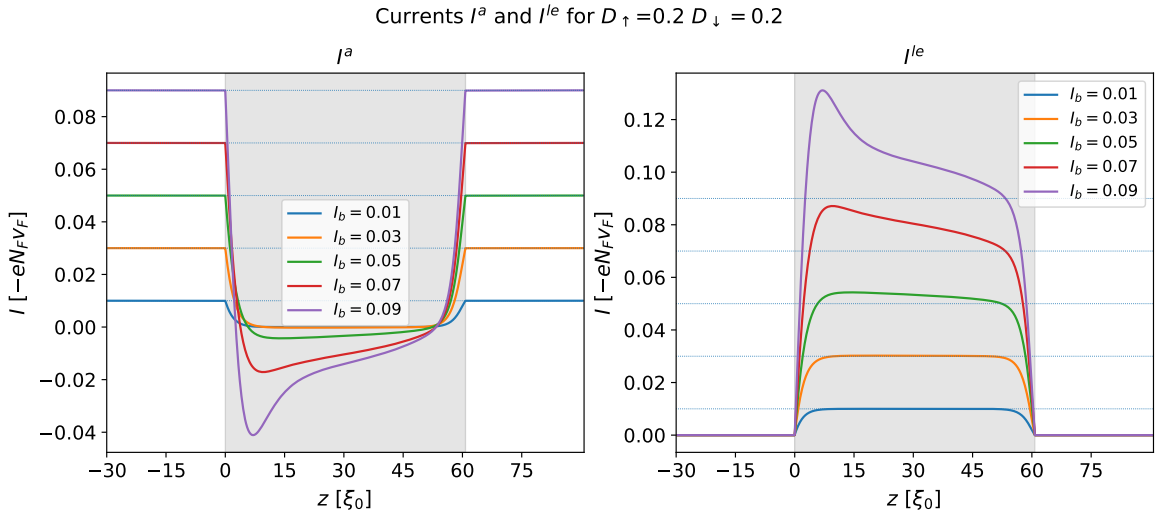

Figure 3.20: *Conversion from normal-state "anomalous" current into supercurrent over the system with a left-interface transparency $D = 0.2$. The dotted lines show the respective boundary current.*

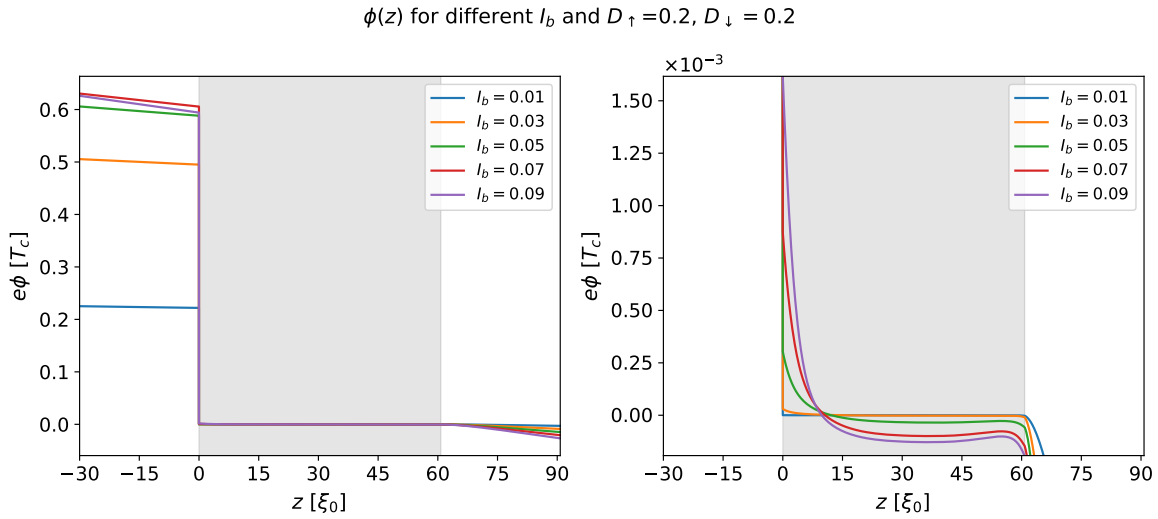

Figure 3.21: *Chemical potential $\phi(z)$ for the NIS system with a left-interface transparency of $D = 0.2$. Left: $\phi(z)$ over the whole range of the system. Right: Enlargement of the central superconducting region.*

The low transparency leads to an even larger potential drop at the interface, which largely dominates the behaviour of ϕ. We can see that the potential difference between the left system edge and the interface is less than five percent. For smaller transparencies, this behaviour gets even more pronounced. Lastly, we can see the order parameter and p_s for the low-transparency case in Fig. 3.22.

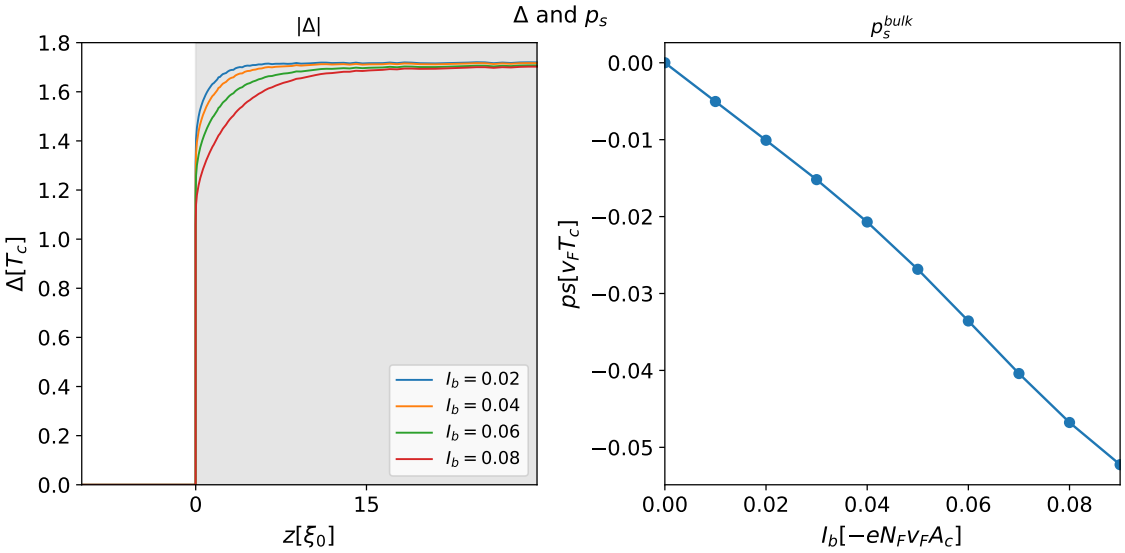

Figure 3.22: *Spatial dependence of the order parameter (left) and bulk value of the superflow p_s (right) for small currents with a left-interface transparency $D = 0.5$*

Compared to the cases of higher transperencies, see Fig. 3.15 and 3.19, we see a much larger suppression of Δ near the interface, while the bulk p_s for a given current remains unchanged. This suggest that within our model, we do not reach the depairing current in the bulk. The depairing current is defined as the current where superconductivity breaks down because the superflow becomes so large that $v_F p_{s,dep.} = \Delta$, see also [14]. Rather, the injection of a nonequilibrium quasiparticle population over the superconducting energy gap forces the superflow near the interface to becomes so large that it destroys superconductivity.

3.5 Comparision to potential-bias description

In contrast to the NIN system discussed in Sect. 3.3 the potential jump at the interface will now be dependent on the boundary current. This is expected since the conductance at an N-S interface depends on the energy of injected quasiparticles, see also the discussion in Sect. 3.2. As we have discussed in this chapter, enforcing a larger current requires a wider energy window.

Instead of considering the potential drop over the interface, as in the NIN case, we will compare the potential drop from the left of the interface to the center of the superconductor. As we had seen, the conversion from quasiparticle current into superflow happens over a finite lengthscale rather than at the interface only. We define this potential drop as

$$\Delta\phi_{SC} \equiv \phi_L - \phi_{SC,center}, \tag{3.17}$$

where L refers to the left of the interface, and the other potential is taken at the center of the superconductor.

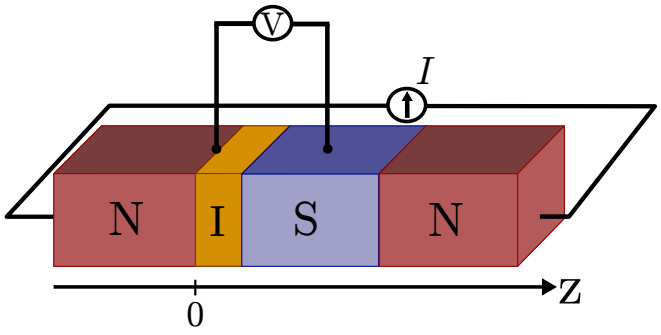

Figure 3.23: *Sketch of a voltage-drop measurement in the NIS system.*

This can be seen as modelling a four-point measurement, depicted in Fig. 3.23, and is thus also experimentally relevant. We note that experimentally it is most likely impossible to locate the voltage probe exactly at the interface and measurements can include spread resistance, see also the discussion in [60]. Using the potential drop in Eq. (3.17), we can determine the implicit dependency

$$\Delta\phi_{SC}(I_b), \tag{3.18}$$

which gives the potential drop as a function of current. We then define the interface resistance for the N-S interface via

$$R_{I,SC} \equiv \frac{\Delta\phi_{SC}}{I_b}. \tag{3.19}$$

This resistance as function of current can be seen in Fig. 3.24. Experimentally, the resistance $R_{I,SC}$ can be obtained as the slope of the $\Delta\phi(I)$ curve in a measurement of the voltage drop as function of the applied current I_b in the sense of Fig. 3.23.

We see that the resistance vanishes in the case of full transparency. For finite transparency, the resistance is peaked at small currents and falling off for larger currents. As discussed, a larger current requires a larger energy window and for energies closer to the gap edge, the probability of Andreev reflection increases which provides a transport channel that does not create a voltage drop.

For the full transparency interface, the potential-bias description in Sect. 3.2 predicted a subgap-conductance of twice the normal-state conductance, in agreement with [28]. Our results, however, predict a vanishing resistance in the full-transparency case indicating a diverging conductance. Similiar to the discussion of the normal-state resistance, i.e., the discussion of Eq. (3.12), this discrepancy is caused by the fact that our approach in fact uses a different definition of the conductance than the BTK approach.

Following the arguments presented in [56], the potential-bias description can be seen as relating the potential of the *incoming* (right-moving) electrons to the potential of the (grounded) superconductor, i.e., it assumes a relation

$$I = G\ \left(\mu_{\mathrm{R}} - \mu_S\right), \tag{3.20}$$

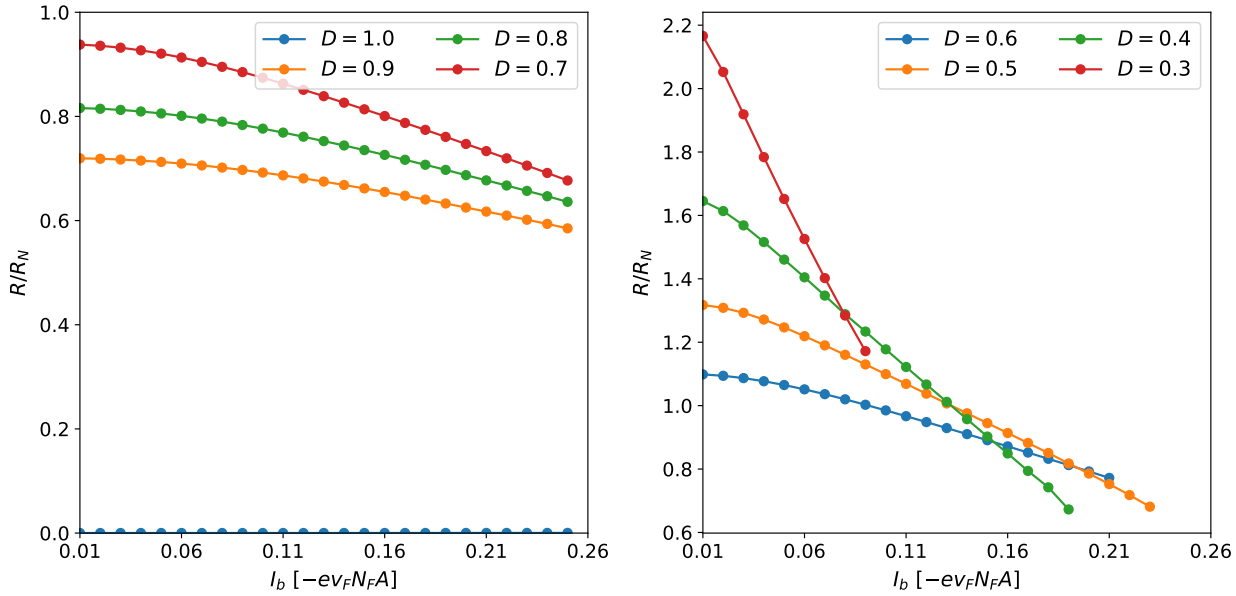

Figure 3.24: *Interface resistance $R_{I,SC}$ normalized to normal-state resistance as function of applied current for different transparency D.*

where R refers to right-moving. The chemical potential we calculate however, is the average of left-moving and right-moving electrons,

$$\langle \mu \rangle = \frac{1}{2} \left(\mu_L + \mu_R \right), \tag{3.21}$$

and in terms of this averaged potential, we will have a relation

$$I = \tilde{G} \left(\langle \mu \rangle - \mu_S \right), \tag{3.22}$$

where generally $\tilde{G} \neq G$. We had seen in Sect. 3.3 that our normal-state conductance has the proportionality $\tilde{G} \propto D/R$, in constrast to the potential-bias normal-state conductance discussed in Sect. 3.2 which obeyed $G \propto D$. Our results for a low-transparency interface indicate that in the limit of small transparency, however, both approaches provide qualitatively similiar results, as the transport through the interface becomes dominated by the potential drop at the interface.

4 Spin imbalance

In this chapter we will study transport in a hybrid structure of normal-metal (N) and superconducting (S) regions, connected via a spin-active interface (SAI), as depicted in Figure 4.1. Here, the SAI between the left and central region will have varying transparencies $D_\uparrow$, $D_\downarrow$, and possibly give rise to a spin-mixing angle ϑ caused by different phase shifts for spin-up and spin-down excitations[4].

There are two independent effects that we will discuss separately. Firstly, the transparencies for spin-up and spin-down quasiparticles can be different, referred to as spin filtering. Secondly, we can have a finite spin-mixing angle ϑ, which is accordingly referred to as spin mixing. While in a real-world system both effects will typically be present, we discuss them individually in order to separate the effects of the two mechanisms.

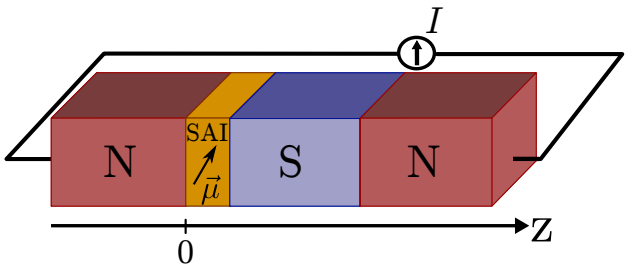

Figure 4.1: *Sketch of an normal-metal/superconductor hybrid system with spin-active interface. The central S region can also be replaced by a normal conductor, referred to as NIN system.*

4.1 Andreev bound states

The phenomenon of Andreev reflection discussed in Sect. 3.1 gives rise to additional interesting physics. Earliest discussed in [61, 62] for a normal metal-insulator-superconductor (NIS) system, so-called Andreev bound states (ABS) can appear at the boundary region between a superconductor and a normal metal. In short, particles are Andreev-reflected at the surface of the superconductor and normal-reflected at the normal metal surface. This can lead to constructive interference and hence a bound state between the two subsystems. Using a Bohr-Sommerfeld quantization argument, see [63], it can be shown that the energy of this bound state is given by

$$E = \pm\Delta \cos\frac{\beta(E)}{2}, \tag{4.1}$$

where $\beta(E)$ is the energy-dependent phase accumulated by a particle while propagating between repeated reflections.
As has been predicted theoretically[64] and shown experimentally[65], a SAI gives rise to a spin-dependent ABS. This can be understood by considering a diagram, similiar to those used in Sect. 2.67, see Fig. 4.2.

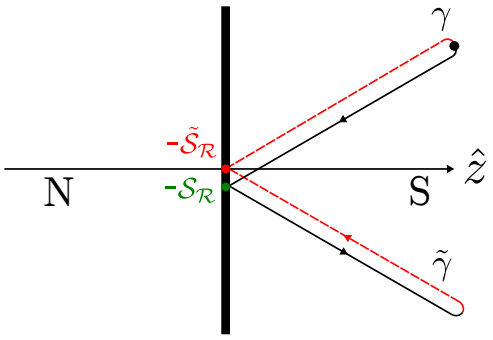

Figure 4.2: *Formation of an Andreev bound state: An electron starting in the black dot (top right) gets reflected at the SAI ($\mathcal{S}_{\mathcal{R}}$), gets converted to a hole ($\tilde{\gamma}$) that gets reflected again ($\tilde{\mathcal{S}}_{\mathcal{R}}$) and gets converted back to an electron (γ), forming a closed loop.*

In the case of a spin-active interface, the total phase acquired is composed of, firstly, each reflection giving rise to a spin-dependent phase shift $\pm\vartheta/2$, recall Eq. (2.79), and an energy-dependent phase shift caused by particle-hole conversion. Combining these contributions, one can show that the bound-state energy will be

$$\varepsilon_{ABS,\pm} = \pm\Delta\cos\frac{\vartheta}{2}, \tag{4.2}$$

where ϑ is the spin-mixing angle of the interface[40, 63]. For the non-trivial cases of $\vartheta \in (0, 2\pi)$ these bound states are thus within the superconducting energy gap.[1] The creation of these bound states by an SAI strongly alters both the equilibrium behaviour as well as the non-equilbrium transport properties at an NS interface.

4.2 Equilibrium properties

If we do not perform a self-consistent calculation, we can derive the subgap density of states analytically, and find

$$\frac{N(\varepsilon)}{N_F} = \frac{1-R_\uparrow R_\downarrow}{1+R_\uparrow R_\downarrow-2\sqrt{R_\uparrow R_\downarrow}\cos(2\delta-\vartheta)} + \frac{1-R_\uparrow R_\downarrow}{1+R_\uparrow R_\downarrow-2\sqrt{R_\uparrow R_\downarrow}\cos(2\delta+\vartheta)}, \tag{4.3}$$

where $\delta = \arccos(\varepsilon/\Delta)$, see also [46]. This shows that there are pairs of resonances, located around the energy given by Eq. (4.2). A resonance apporiximation for the

[1] Note that the spin-mixing angle, that can be understood as a phase difference between up-spin and down-spin quasiparticles, is 2π-periodic.

spin-up peak leads to

$$\frac{N_\uparrow}{N_F} \approx \frac{\Delta(1+\sqrt{R_\uparrow R_\downarrow})\sin\frac{\vartheta}{2}}{2\sqrt[4]{R_\uparrow R_\downarrow}} \frac{\Gamma}{\Gamma^2+(\varepsilon-\varepsilon_{ABS,+})^2}, \tag{4.4}$$

where

$$\Gamma = \frac{\Delta(1-\sqrt{R_\uparrow R_\downarrow})\sin\frac{\vartheta}{2}}{2\sqrt[4]{R_\uparrow R_\downarrow}}. \tag{4.5}$$

For small D, the peak is then a Lorentian of width $\Gamma \overset{D\ll 1}{\approx} \Delta(D/2)\sin(\vartheta/2)$. Using the spin-resolved density of states one can show that these ABSs are each spin-polarized, with the spin-up (spin-down) state at positive (negative) energy. For larger transparencies, the peaks broaden considerably and spread out over the subgap region. In a self-consistent calculation that includes impurities there is typically additional broadening of the bound state. Fig. 4.3 shows the density of states for different values of the spin-mixing angle and different impurity strengths in the SC.

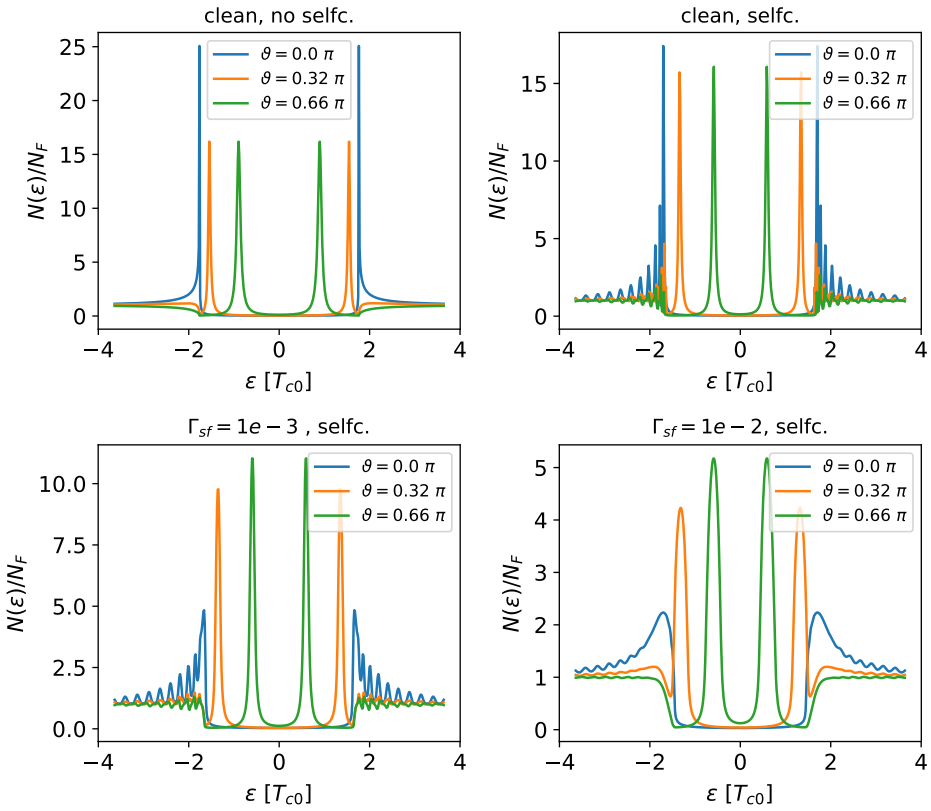

Figure 4.3: *Density of states at the SAI for $D = 0.06$, different impurity strengths in the SC and spin-mixing angle. The oscillations are so-called Tomasch oscillations that are suppressed by high impurity concentration and average out if more trajectories are included in the calculation.*

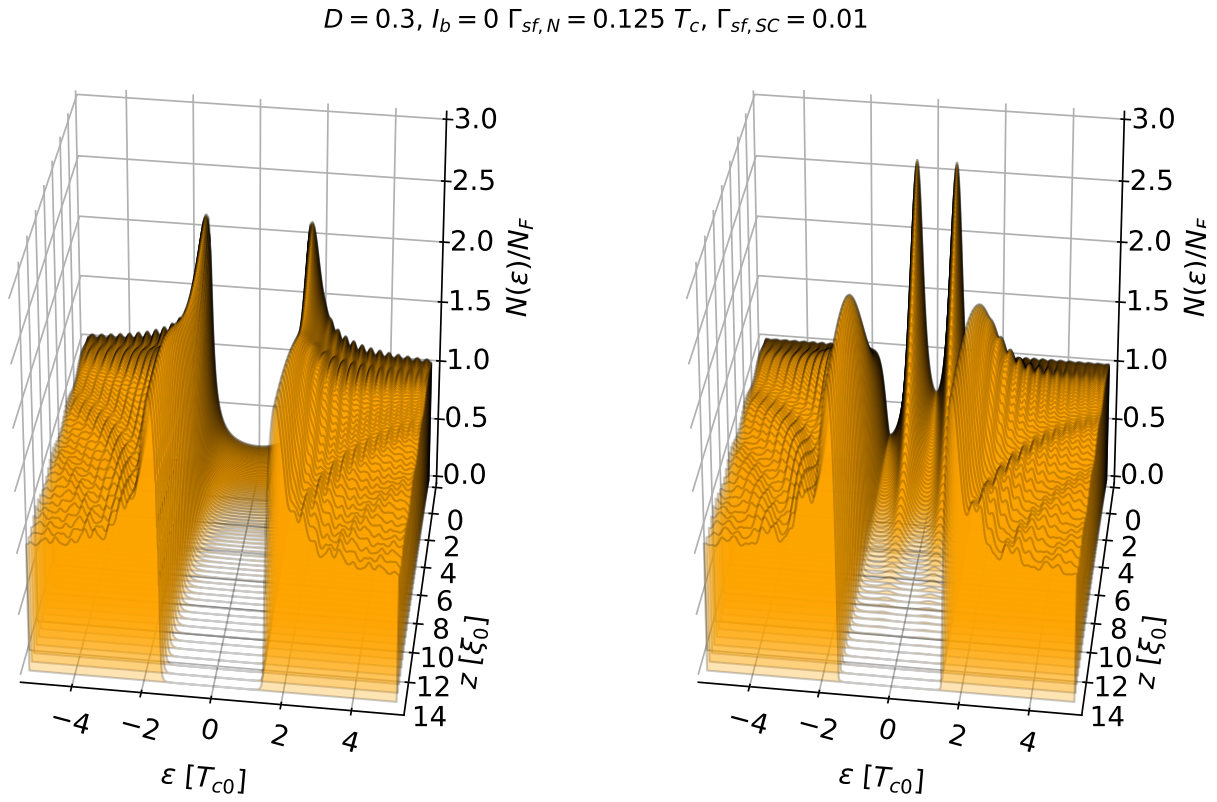

Figure 4.4: *Density of states as function of energy and distance from the SAI (at $z = 30\xi_0$) for a spin-mixing angle of $\vartheta = 0$ (left plot) and $\vartheta = 0.49\pi$ (right plot).*

Even without impurities, the inverse proximity effect reduces the spectral gap from the bulk BCS value of $\Delta \approx 1.763\ T_{c0}$ to about $\Delta_{selfc.,eq} \approx 1.44\ T_{c0}$. A small impurity concentration of $\Gamma = 0.01\hbar$ reduces the gap by less than 5%.

Away from the interface, the bound state decays into the bulk of the superconductor. Fig. 4.4 shows the spatially-resolved density of states obtained for a self-consistent calculation without an applied current but with taking into account the inverse proximity effect, i.e., a reduction of the order parameter close to the normal region. Even without spin-mixing (left plot), the inverse proximity effect induces a nonzero density of states in the entire gap near the interface that decays within one coherence length. In the case of non-vanishing spin-mixing angle (right plot), a larger transparency combined with impurities broaden the peaks. We can see that the bound-state features reach out further into the bulk but have similiarly disappeared within less than 10 ξ_0.

As discussed above, the ABS peaks in the density of states are spin-polarized, one at positive and one at negative energies. In equilibrium and for $\vartheta \in (0, \pi)$, the positive-energy spin-up state is is unoccupied while the negative-energy spin-down state is occupied. The resulting unequal occupation of spin-up and spin-down states leads to a magnetization even in equilbrium.

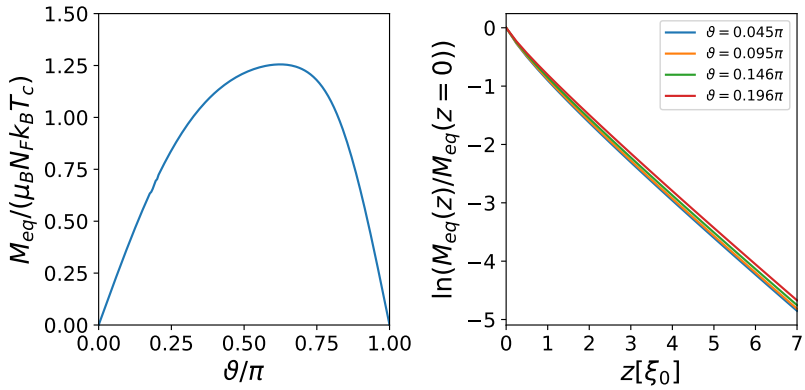

Figure 4.5: *Equilbrium magnetization at the SAI as function of spin-mixing angle ϑ (left) and decay into the bulk of the SC (right).*

For $\vartheta \in (\pi, 2\pi)$, the two spin orientations change their roles and the magnetization changes sign. Fig. 4.5 shows the magnetization for different spin-mixing angle and the decay into the bulk of the superconductor. We note here that the equilibrium magnetization is reduced compared to the results in [40], where the self-consistency of the order parameter was neglected, with the maximal value being slightly less than half of the non-selfconsistent result. Just as in the discussion in Ch. 3, we can consider the non-self consistent interface scattering amplitudes for the case of finite spin-mixing angle, shown in Fig. 4.6.

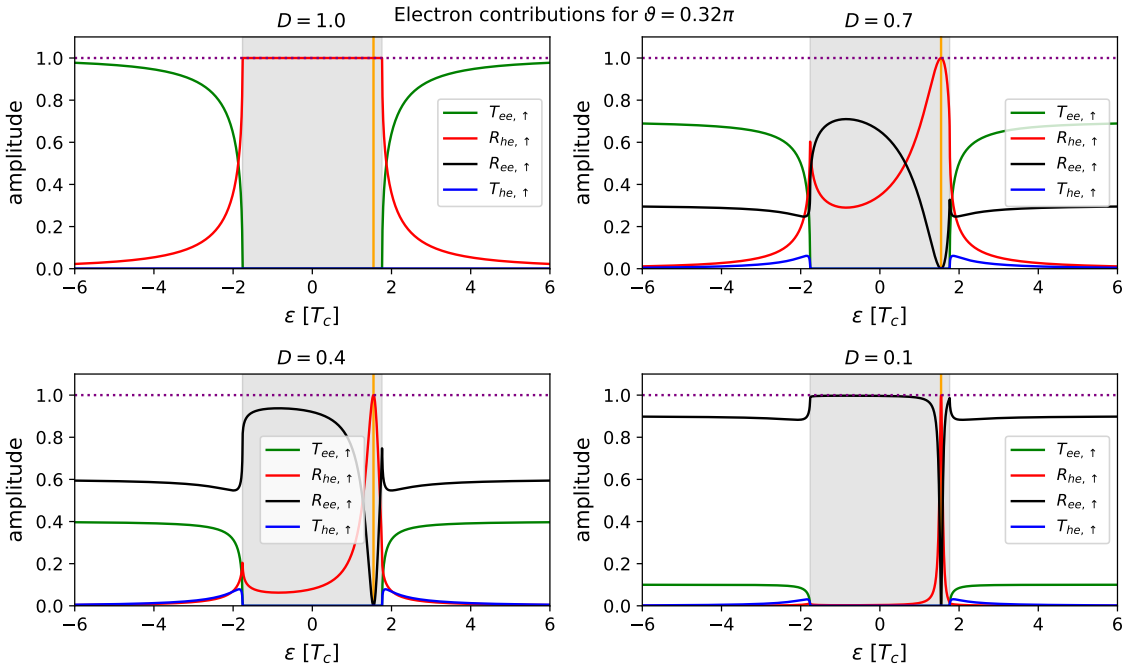

Figure 4.6: *Physical mechanisms for charge transport at the N-S interface on the normal side. The purple-dotted line is the sum of all four contributions which has to equal unity according to Eq. (2.77), the orange line is the position of the ABS.*

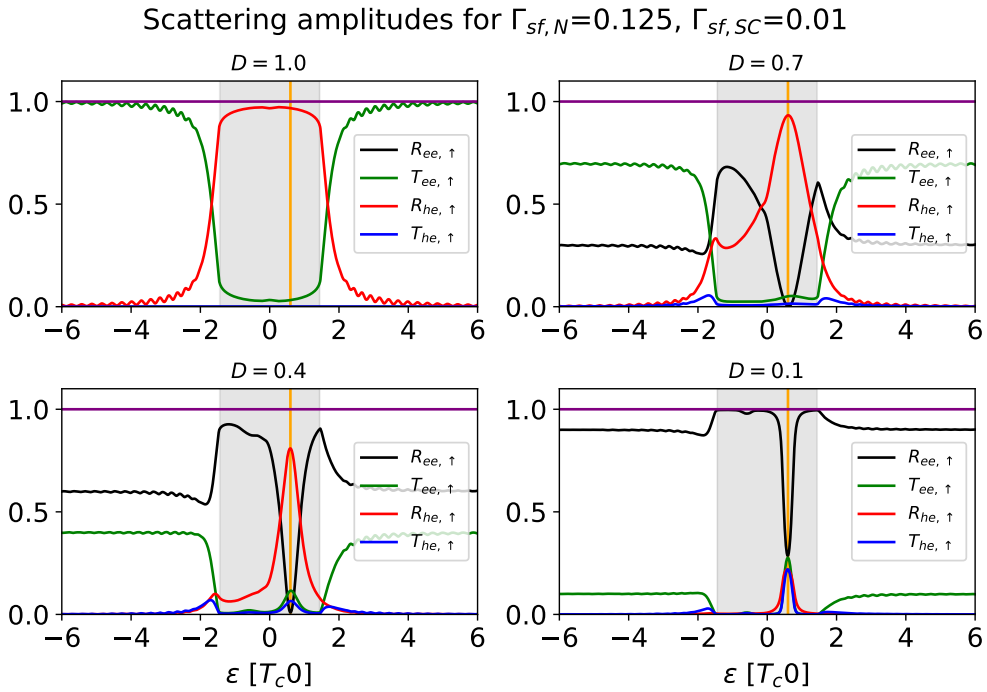

Figure 4.7: *Physical mechanisms for charge transport at the N-S interface on the normal side with small impurity concentration. The purple-dotted line is the sum of all four contributions which has to equal unity according to Eq.* (2.77)*, the orange line is the position of the ABS.*

In an energy window around the bound-state energy, Eq. (4.2), Andreev reflection is always possible. The size of the energy window is seen to decrease for smaller transparencies. In contrast, Andreev reflection is largely suppressed within the entire subgap region if no ABS is present, see Fig. 3.3 in Chapter 3. Similiarly to the discussion there, the presence of impurities will slightly alter these results, as shown in Fig. 4.7. Notice especially that for low transparency not only Andreev reflection is possible around the bound-state energy but rather also electron transmission T_{ee} and Andreev transmission T_{he}. However, these transmitted quasiparticles become converted into superflow over a finite lengthscale, see also the discussion in Chap. 3, since there are no quasiparticle states in the energy gap inside the superconductor.

4.3 Normal metal

We start with both the central and outer regions being a normal metal. Similiarly to the discussion for charge imbalance, the superconducting order parameter Δ, as well as the coherence functions γ vanish everywhere and the entire physics is captured by the distribution function x and the chemical potential ϕ.

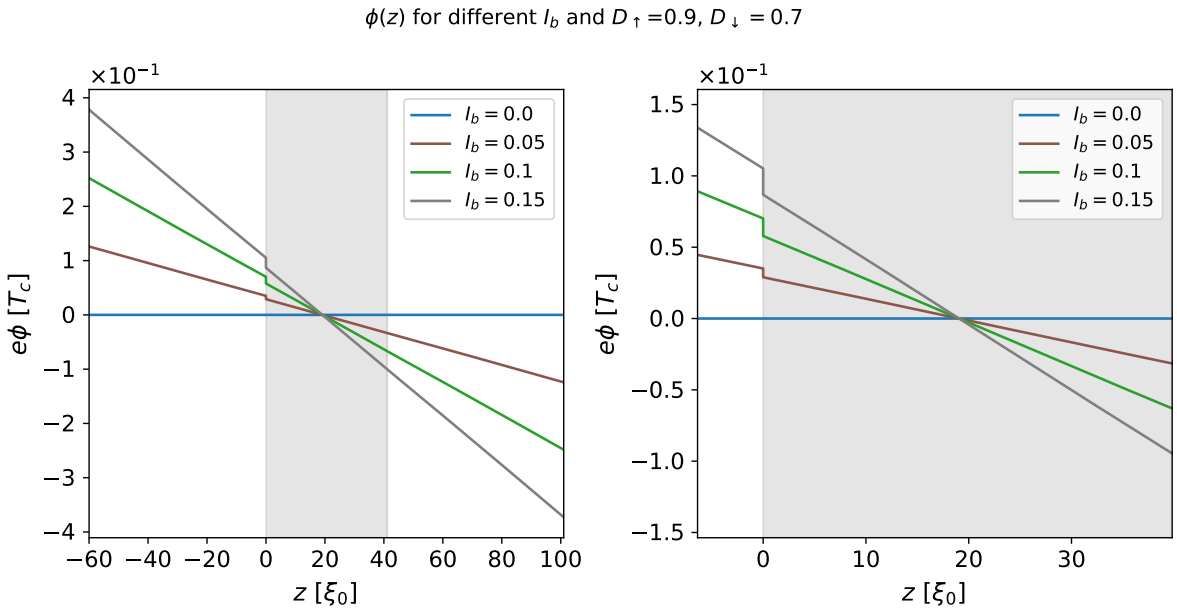

Figure 4.8: *Chemical potential $\phi(z)$ for spin-filtering in the NIN system. Left: Drop of ϕ over the whole range of the system. Right: Enlargement of the central region with the potential jump at the interface, always for the respective top figure.*

4.3.1 Spin filtering

In the case of spin-filtering we have different transparencies for the two spin orientations. In the following we assume that $D_\uparrow > D_\downarrow$, so that spin-up quasiparticles always have a higher transmission probability, the opposite case only switches the sign of magnetizations and spin currents. The filtering has two effects: Firstly, a finite spin current and magnetization are created in the vicinity of the interface. Secondly, the interface resistance that determines the jump in the chemical potential will typically be altered compared to the spin-degenerate case.
Fig. 4.8 shows the shape of the chemical potential for small spin filtering, $D_\uparrow = 0.9, D_\downarrow = 0.7$. While the absolute potential drop is slightly higher compared to Fig. 3.7, the overall behaviour is unchanged, we have a linear gradient in ϕ within each region, combined with a jump at the left-hand side interface.

Similiar to the spin-degenerate case, the potential jump depends on both bias current and transparency. The potential drop can thus be quantified by the interface resistance defined in Eq. (3.10), shown in Fig. 4.9.

In a simplified picture, the two spin orientations are two independent, parallel transport channels through the interface with different transparencies giving rise to a different potential jump compared to the spin-degenerate case.

The total resistance for $D_\uparrow = 0.9$ and varying $D_\downarrow$ will thus always be between the resistance for spin-degenerate $D = 0.9$ and the respective lower resistance. In

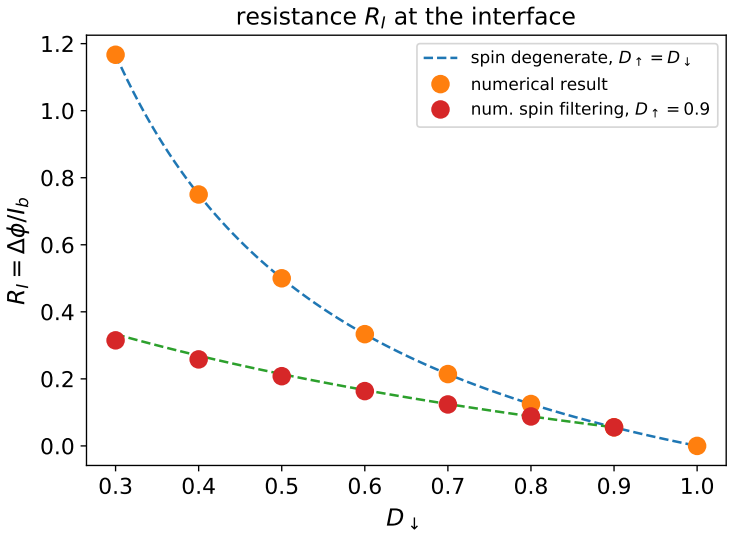

Figure 4.9: *Resistance R_I at the SAI for spin filtering with different transparency $D_\downarrow$.*

similiar logic to the discussion around Eq. (3.12), we find the dependency

$$R_I/R_0 = \frac{R_\uparrow + R_\downarrow}{D_\uparrow + D_\downarrow}. \tag{4.6}$$

In Fig. 4.10, we see the magnetization induced by the spin-filtering for the same transparencies as in Fig. 4.8.

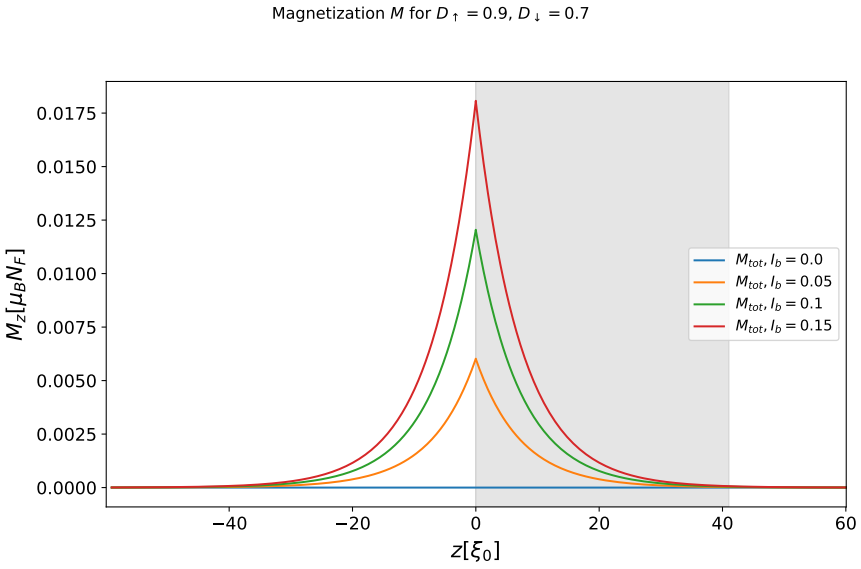

Figure 4.10: *Magnetization $M(z)$ induced by the SAI, at $z = 0\ \xi_0$, for small spin-filtering. The grey area marks the central region.*

Notice that there is no magnetization in the equilbrium case of $I = 0$, indicating

that the magnetization is a pure nonequilbrium phemenom for the normal-metal system and caused by current flow.

In a simplified picture, a large transparency for spin-up quasiparticles leads to more spin-up being transferred to the right side of the interface and, at the same time, more reflection of spin-down quasiparticles on the left side. There will thus be an imbalance of more spin-up particles on the right and more spin-down particles on the left, resulting in a net magnetization with opposite signs. Directly at the interface, the magnetization on the left and right side are, consequently, opposite in direction but equal in magnitude.

The magnetization then decays exponentially with distance from the interface. The fact that the decay is symmetric on both sides of the interface is due to the fact that we have the same spin-scattering mean free path on both sides. In the case of unequal impurity concentrations on the two sides, we find equal absolute values of M^a at the interface, but a decay over different lengthscales on the two sides (not shown).

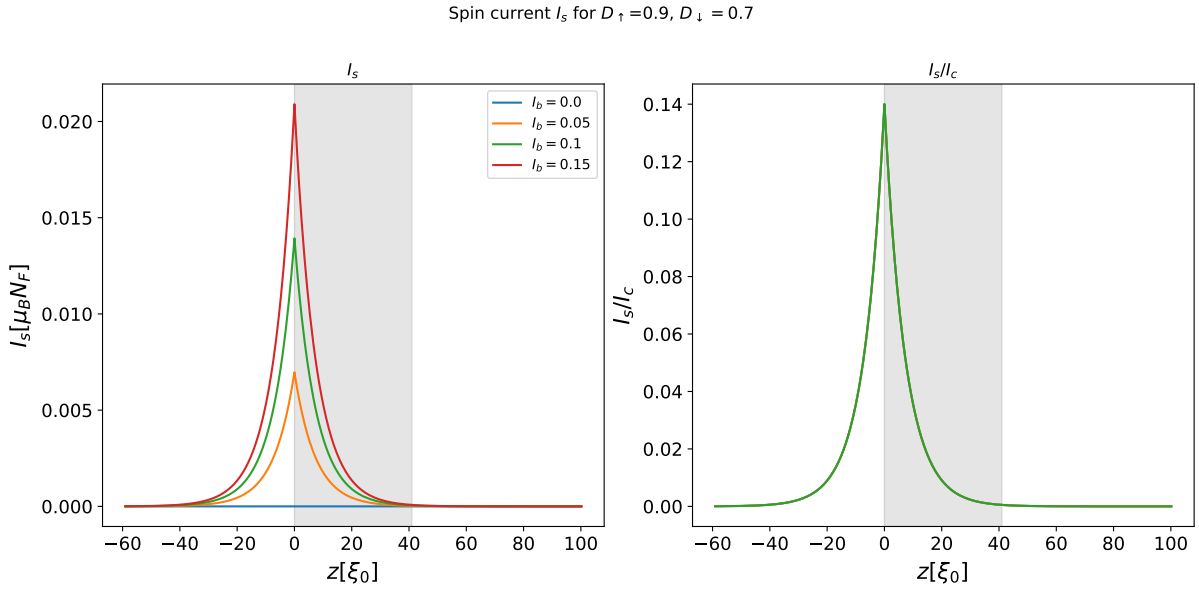

Figure 4.11: *Left plot: Spin current I_s near the interface. Right plot: Current polarization $P = I_s/I_c$ near the interface.*

Additionally, the spin filtering results in a spin current across the interface, which can be seen in the left of Fig. 4.11, caused by a partial spin polarization of the current. The right plot in the same figure shows that the polarization of the spin current does not depend on the choice of boundary current I_b since the ratio I_s/I_c is a constant. Hence, this polarization is a property of the SAI only and determined by the difference in transparency for the two spins.

A standard result for charge currents is the derivation of a conservation law of

the form

$$\partial_t \rho_c + \vec{\nabla} \cdot \vec{j}_c = 0, \tag{4.7}$$

which in the case of our stationary nonequilbrium simplifies to a conservation of charge current throughout the system.[1] As discussed in [67], a similiar balance equation can be derived for spin current, which is typically *not* a conserved quantitiy, in the form of

$$\partial_t \rho_{s_z} + \vec{\nabla} \cdot \vec{j}_{s_z} = S(z), \tag{4.8}$$

where $S(z)$ is an inhomogenous source or drain term that has to be derived from microscopic theory. A simplified model consist of assuming

$$S(z) = -\frac{M(z) - M_0}{\tau}, \tag{4.9}$$

where τ is a characteristic decay time and $M(z) - M_0$ is the nonequilibrium magnetizatin. In our case, τ is determined by the spin-flip mean free path, $\tau_{sf} = l_{sf}/v_F$. Since we are considering the one-dimensional, time-independent case, we thus find

$$\partial_z j^z_{s_z} = -\frac{M(z) - M_0}{\tau}. \tag{4.10}$$

In the normal metal case, we find good agreement between such a model and the spin-current decay.

While the absolute value of $M^a(z)$ is current-dependent, the ratio M_z/I_b is, similiarly to the current polarization, a constant that is only determined by the difference between $D_\uparrow$ and $D_\downarrow$, as seen in Fig. 4.12.

[1] As discussed in, e.g., [66], in superconducting regions there is a right-hand side in this equation that vanishes once the order parameter is obtained self-consistently, restoring current conservation.

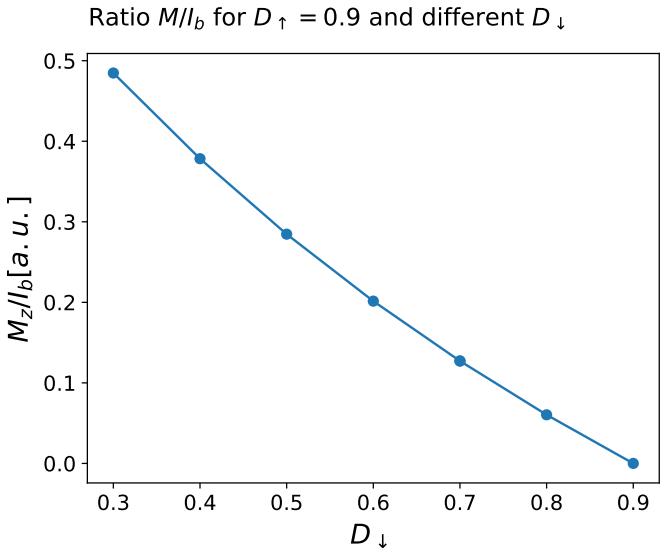

Figure 4.12: *Ratio of Magnetization over current, M_z/I_b, for varying transmission $D_\downarrow$ at fixed $D_\uparrow = 0.9$.*

This shows that the spin imbalance that leads to the magnetization is caused by different backscattering rates for the two spin-orientations and hence determined by barrier properties.

4.3.2 Spin mixing

In entirely normal-metal system, a spin-mixing angle at the SAI does not have any observable effect, and the results reduce to those for the spin-degenerate or spin-filtering case depending on the transparencies for the two spin orientations. In physical terms, the absence of particle-hole correlations means that the different phase shifts caused by the barrier are irrelevant to the transport — since there is no coherent transport channels available, quantum-mechanical phase differences do not have any observable effect in the average current or magnetization. We note that an effect on higher-order correlation functions, such as current noise, is possible but outside the scope of this work.

4.4 Superconductor

We had seen in the discussion of charge imbalance how a central superconducting region alters the transport behaviour by the presence of the condensate and Andreev reflection. Regarding the spin-dependent transport, similiar new features appear. The main difference to the normal-metal case is the existence of spin-polarized Andreev bound states at the SAI in an N-S hybrid system. As was shown

in [40], these states lead to a finite equilbrium magnetization with the dependency

$$M^{eq} = M^{tot}(I = 0) \propto \sin\vartheta \; f(\vartheta). \tag{4.11}$$

In the case of spin filtering there is thus no equilibrium magnetization just as for the NNN system.

4.4.1 Spin filtering

We again assume that $D_\uparrow > D_\downarrow$, so that spin-up quasiparticles always have a higher transmission probability. In subsection only, the calculations were performed with a slightly larger impurity concentration in the superconductor, namely $\Gamma_{sf} = 0.05\ \hbar$, which reduces the mean free path to $l_{sf} \approx 20\ \xi_0$ in the superconductor. Additionally, the bulk order parameter, and hence the critical current, gets suppressed.

The spatial behaviour of the chemical potential is similiar to the case of charge imbalance, with the jump at the interface being slightly altered in the case of spin-filtering by the different transparencies for the two spin channels. Fig. 4.13 shows the chemical potential for small spin-filtering strength. The general behaviour of ϕ in the normal and superconducting region is similiar to the spin-degenerate case discussed in Chapter 3. The potential jump at the interface, however, is no longer only determined by interface properties but rather also dependent on the applied current bias, as seen in Fig. 4.14.

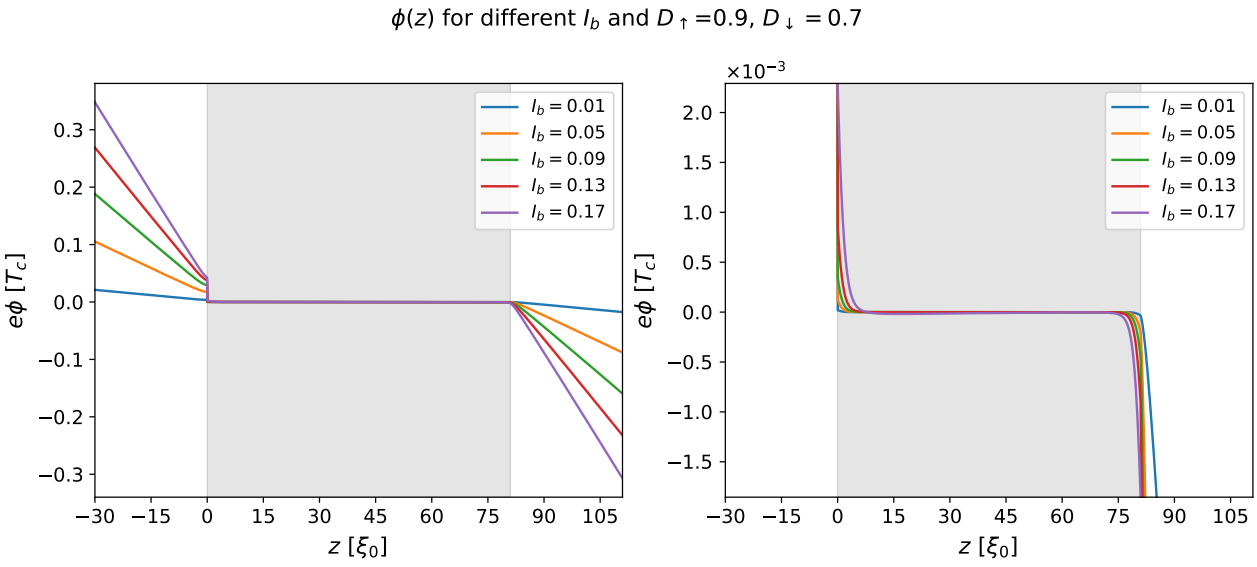

Figure 4.13: *Chemical potential $\phi(z)$ for spin-filtering in the NSN system with a left-interface transparency $D_\uparrow = 0.9$ and $D_\downarrow = 0.7$. Left: $\phi(z)$ over the whole range of the system. Right: Enlargement of the central superconducting region.*

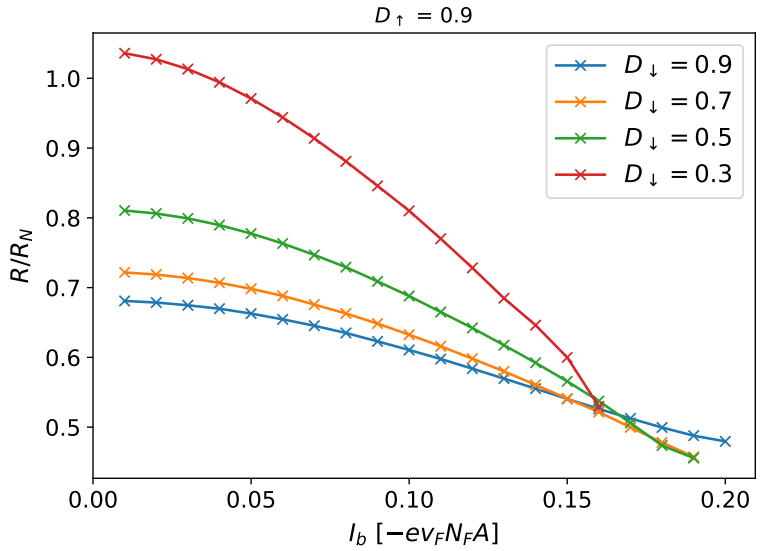

Figure 4.14: *Interface resistance R_I normalized to respective normal-state resistance at the SAI for $D_\uparrow = 0.9$, different transparency $D_\downarrow$ and currents I_b.*

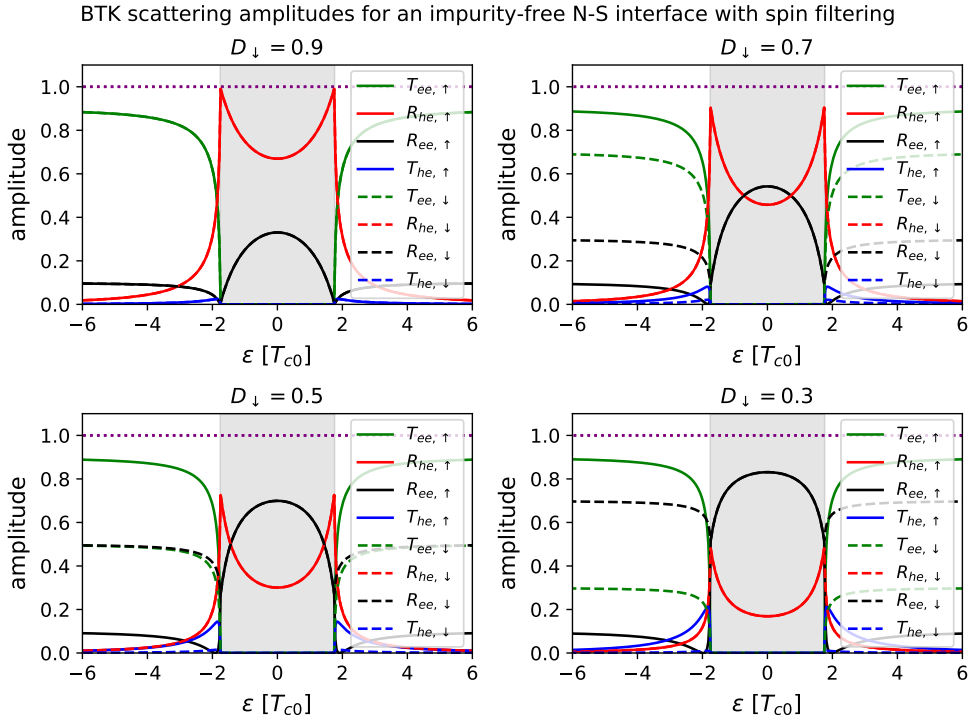

Figure 4.15: *Transport amplitudes for spin filtering. The sum of all four contributions has to add to unity (purple line). In the subgap region the amplitudes for normal and Andreev reflection are degenerate for spin up and spin down quasiparticles.*

In order to understand this behaviour, we can examine the transport amplitudes for constant $D_\uparrow = 0.9$ and varying $D_\downarrow$, seen in Fig. 4.15.

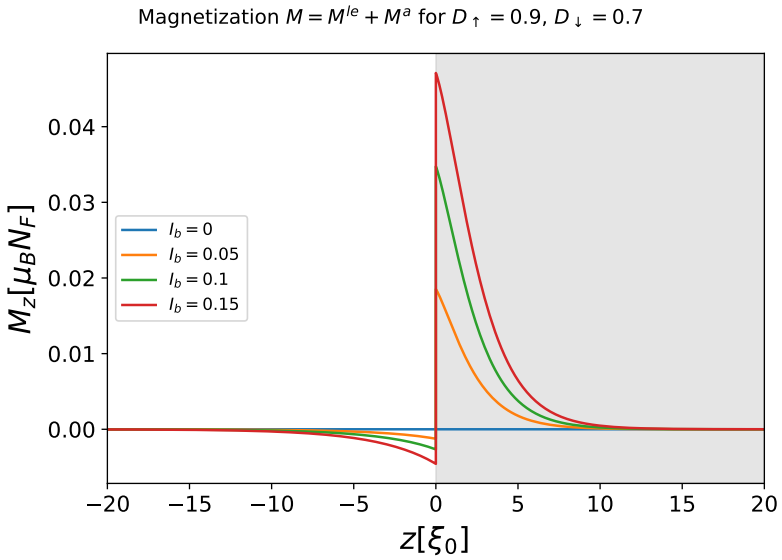

Figure 4.16: *Magnetization $M(z)$ for spin-filtering and subsequent decay with distance to the SAI located at $z = 0$ ξ_0. The gray area marks the superconducting region.*

Starting from a maximum, the resistance decreases for larger currents. This is caused by the fact that the probability for Andreev reflection increases from zero energy towards the gap edge. Since larger currents leads to a larger energy window, more particles can tunnel via Andreev reflection which reduces resistance. Additionally, the maximum resistance increases for larger spin-filtering strength since Andreev reflection becomes suppressed for larger spin-filtering strength. This is expected for an s-wave superconductor where both spin orientations are necessary for Andreev reflection to occur. At the same time, the probability for Andreev transmission (T_{he}) for energies above the gap increase for stronger spin-filtering, which explains the faster drop for large currents in the case of strong spin filtering.

Fig. 4.16 shows the magnetization for small spin-filtering. Compared to magnetization in the normal-metal system, see Fig. 4.10, the magnetization is no longer opposite but of equal magnitude on the two sides of the interface. How can we understand the different magnitudes in the magnetization on the two sides of the interface?

The novel element in the superconducting system is Andreev reflection. Assume spin-up electrons having a higher chance of transmission than down-spin electrons. If a spin-up electron crosses the barrier it will be Andreev-reflected within a few ξ_0, which results in a spin-down hole being retro-reflected. This spin-down hole corresponds to depopulating a spin-down state, which we expect to have two effects. Firstly, it will enhance the spin-up imbalance to the right as spin-down states become depopulated in addition to the spin-up particles being injected into the SC. Secondly, some of the spin-down holes will also be transmitted back into the normal metal, reducing the surplus of spin-down particles and magnetization there.

Fig. 4.17 shows M^{neq} for identical current and transparencies for the normal-metal and superconducting system. We indeed observe that the spin-imbalance gets reduced on the normal side and increased on the superconducting side compared to the normal-metal system.

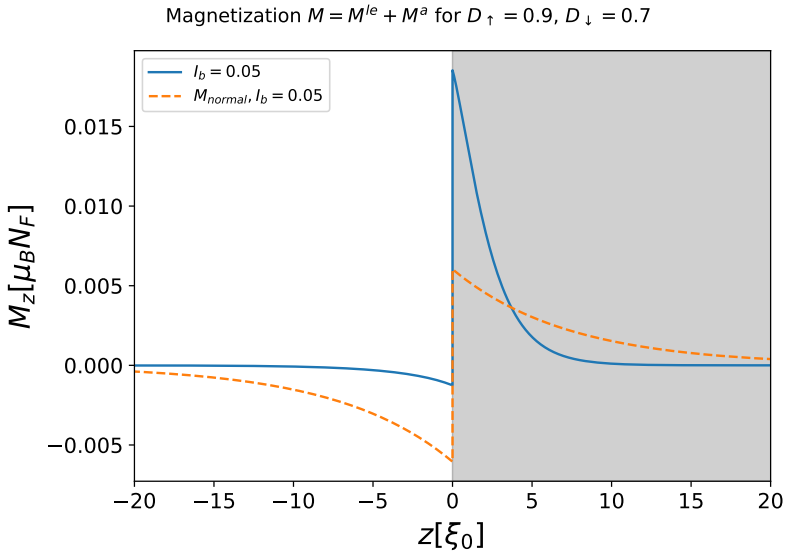

Figure 4.17: *Magnetization for NIS system compared to the NIN system for equal transparencies and current.*

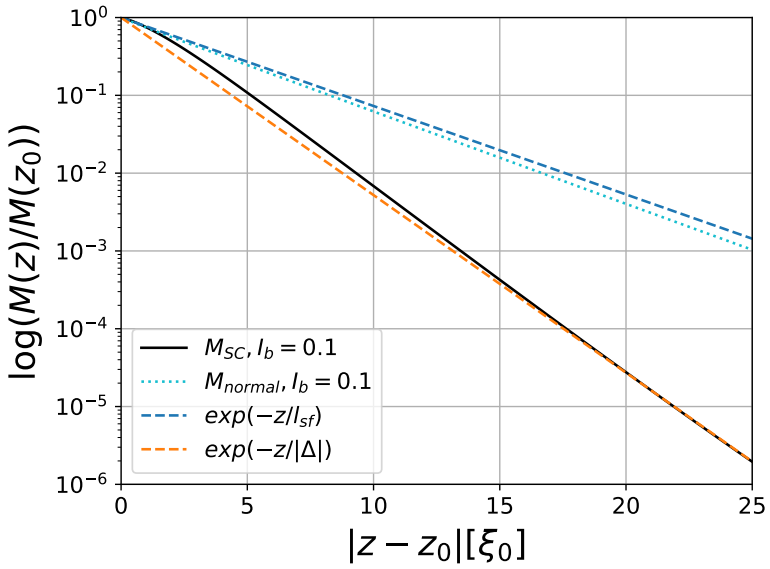

Figure 4.18: *Decay of the magnetization $M(z)$ away from the interface at $z_0 = 0$ into the normal and superconducting regions. The dashed lines are approximately the expected behaviour.*

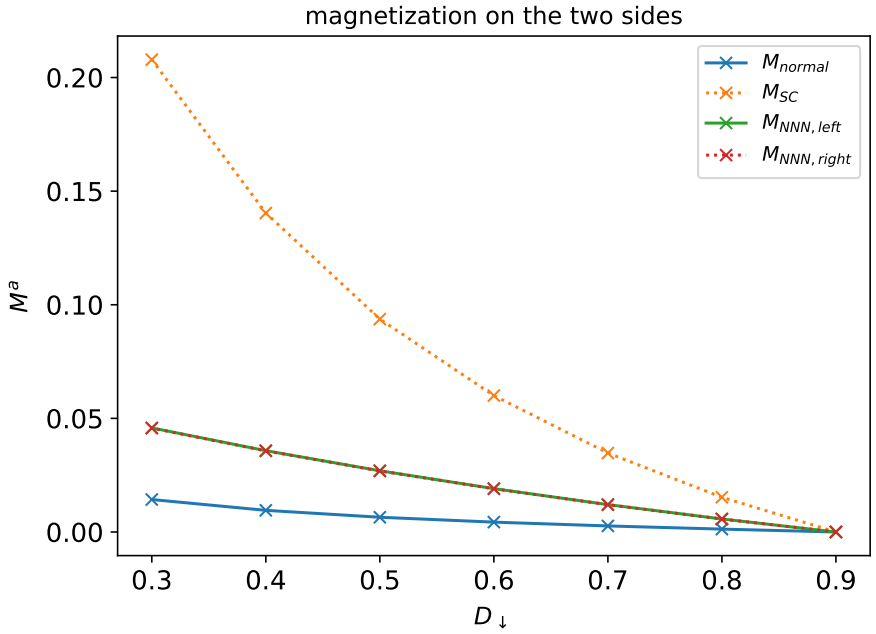

Figure 4.19: *Magnitude of $M^a(z)$ for the left and right side of the SAI in the NIN and NIS system for a medium current of $I = 0.1$.*

While not apparent from the discussion and Fig. 4.16, the magnetization induced at the interface decays over different lengthscales in the normal and superconducting regions. In Fig. 4.18 we show the decay away from the interface for both sides in a semilog plot.

In the normal metal, spin-flip scattering over a lengthscale l_{sf} relaxes the spin imbalance, while in the superconductor the imbalance decays on the shorter lengthscale of Andreev reflection,

$$\xi_{AC} \equiv \hbar v_F \sqrt{\Delta^2 - \varepsilon^2}, \tag{4.12}$$

which converts the injected, spin-polarized quasiparticles into unpolarized superflow.

In Fig. 4.19 we compare the magnetization of the NIN system to the N-SAI-S system for the same current but varying spin-filtering strength. We can see that, independent of the difference in transparencies, the magnetization is always equal in magnitude on the two sides of the SAI if the system is consisting entirely of normal-metal regions.

In contrast, a superconducting region on one side of the interface will create an unequal magnetization on the two sides, as discussed above. Interestingly, this imbalance gets larger as the spin-filtering strength is increased.

This might seem surprising, given that the discussion around Fig. 4.14 indicates that for lower tranmission of one spin-flavour Andreev reflection becomes

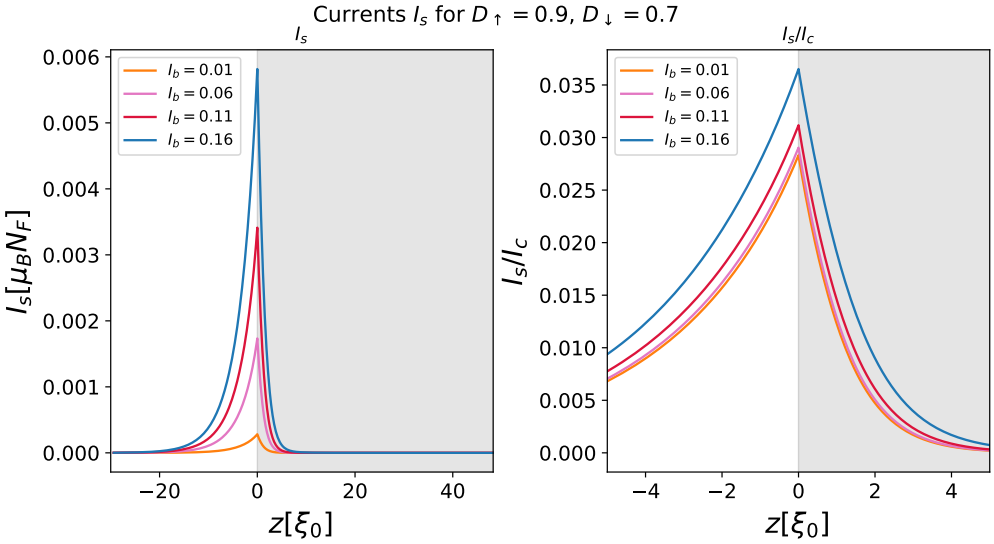

Figure 4.20: *Spin current and current polarization in the superconducting system with* $D_\uparrow = 0.9$ *and* $D_\downarrow = 0.7$.

suppressed while normal reflection becomes dominant. We could thus assume that for larger spin-filtering we get behaviour that is more reminiscent of a N-SAI-N system, which is not the case.

However, the presence of impurities alters the transmission amplitude compared to the clean, non-selfconsistent results, and there is always a finite transmission propability T_{ee} at the interface as long as the transmission is non-zero, caused by the inverse proximity effect. The above argument about Andreev reflection in the superconductor thus still holds given that the Andreev process happens not localized at the interface but rather over a finite lengthscale given by Eq.(4.12).

Lastly, we can examine the spin current, seen in Fig. 4.20 for some exemplary currents. In the normal metal the behaviour is similiar to the N-SAI-N system although the magnitude of the spin currents is reduced for identical transparencies and currents in Fig. 4.11.

Since the interface is only spin-filtering, the entire spin current entering the superconductor is the injected, spin-polarized quasiparticle current. Similiar to the magnetization, the spin current decays on the length scale of Andreev reflection, Eq. (4.12), in the superconductor and on the spin-flip scattering length l_{sf} in the normal metal. The current polarization I_s/I_c gets reduced compared to the normal-metal system, indicating that less spin-polarized quasiparticle current is transported into the superconductor, which can, similiar to the magnetization, be interpreted as a reduction caused by Andreev reflection in the superconducting region. Additionally, there is a weak depence of the ratio on the current caused by the energy-dependence of the spin-dependent scattering amplitudes.

4.4.2 Spin mixing

As discussed in Sect. 4.2 there is a finite equilibrium magnetization in the superconducting system with non-vanishing spin-mixing angle. Depending on the transparency of the interface, the behaviour of both spin current and magnetization is somewhat different. We had seen in Fig. 4.3 that for a tunneling, low-transparency barrier we have distinct bound-state peaks centered around a certain energy. As discussed, each of these Andreev bound states is spin-polarized, which can also be seen in the spin-resolved density of states shown in Fig. 4.21. This spin polarization of the density of states does not exist in the case of spin filtering and creates a nonzero magnetization also in equilbrium. Without an applied current and at zero temperature, all quasiparticle states up to zero energy are occupied.

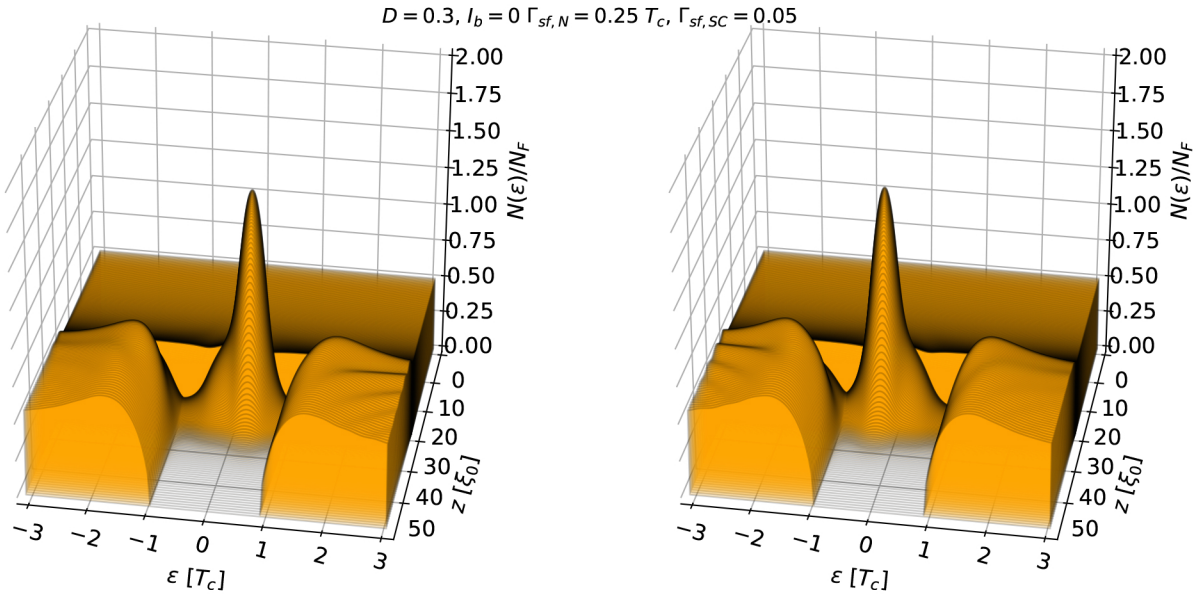

Figure 4.21: *Spin-resolved, equilibrium density of states for an SAI with small transparency of $D_\downarrow = D_\uparrow = 0.3$ and a spin-mixing angle of $\vartheta = 0.66\ \pi$. Spin-up DOS on the left, spin-down DOS on the right.*

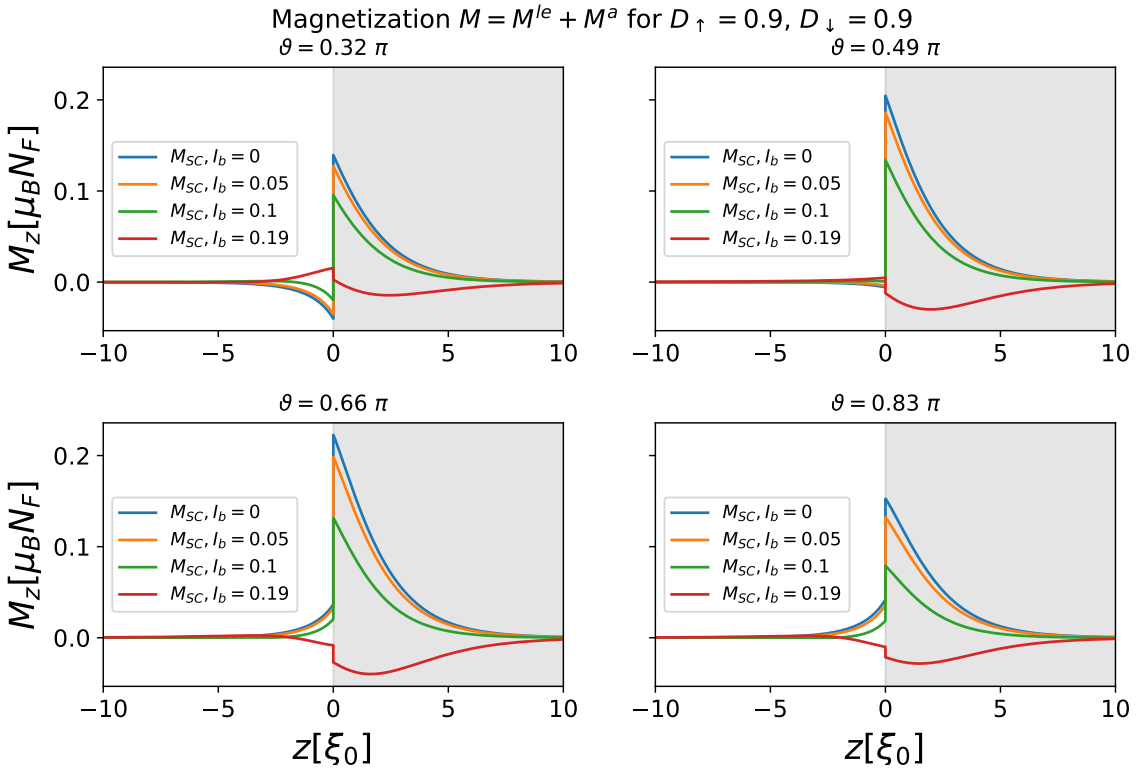

Figure 4.22: *Magnetization at the SAI for high transparency of $D = 0.9$ and different spin-mixing angle ϑ. The grey area marks the superconducting region.*

For spin-mixing angles $\vartheta \in [0, \pi]$, there will be a spin-up peak in the density of states at positve energy, and the occupation of the negative-energy spin-down states will naturally lead to a spin imbalance and magnetization. For angles between π and 2π the two spin-orientations switch roles, while larger or negative angles can be mapped to these two ranges since the physics is 2π-periodic in the spin-mixing angle. Fig. 4.22 shows the magnetization for different currents for a high transparency of $D_\uparrow = D_\downarrow = 0.9$ and varying spin-mixing angles.

Once we apply a current, an increasing number of positive-energy spin-up states participate in transport and become occupied, reducing the spin imbalance. The magnetization should thus decrease compared to the equilibrium magnetization and this is indeed what we observe. Once the entire spin-up state is occupied by a wide enough energy window, the magnetization vanishes. We also see a sign change in the magnetization for a large current of $I = 0.19$ in all four cases. For this large current, we start to occupy continuum states that will become spin polarized opposite to the Andreev bound state, see Fig. 4.23. The behaviour of the magnetization in the normal side can be understood in similiar terms, as the density of states on the normal side will be weakly spin-polarized as a result of the spin-active interface, shown in Fig. 4.24.

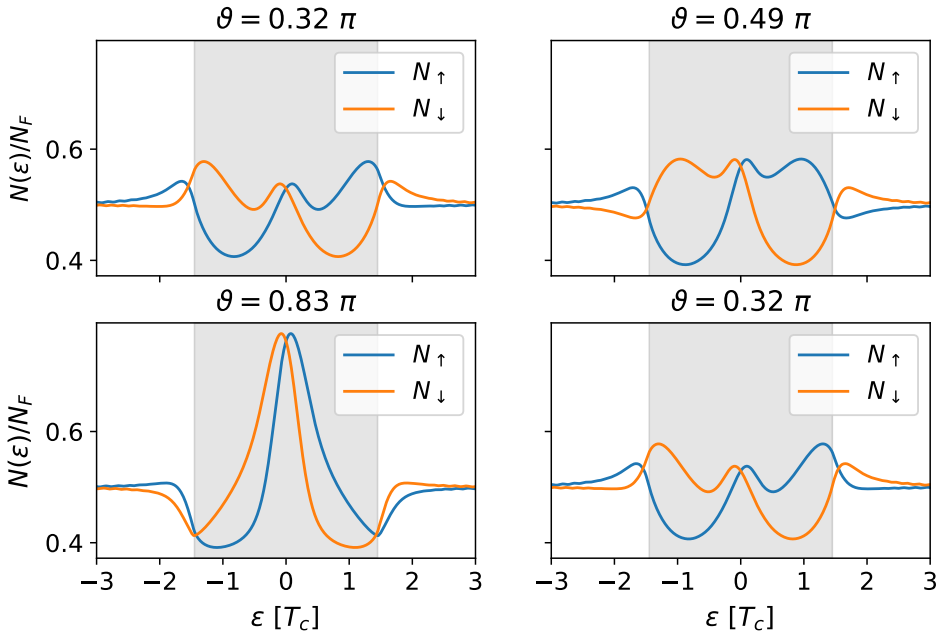

Figure 4.23: *Superconductor-side density of states the SAI for a high transparency of $D = 0.9$ and different values of the spin-mixing angle ϑ. The grey area marks the width of the bulk mean-field energy gap in the superconductor.*

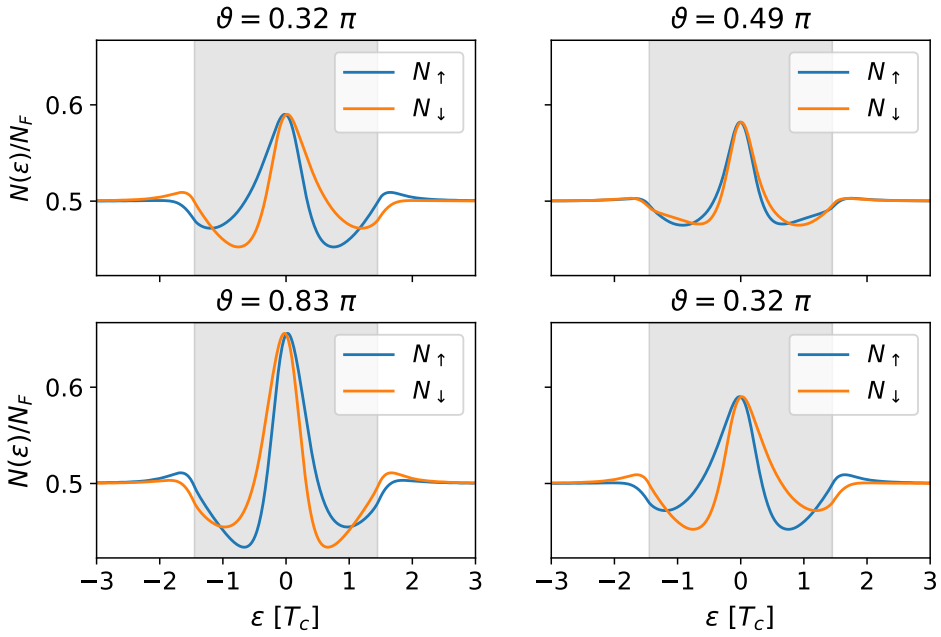

Figure 4.24: *Normal-side density of states the SAI for a high transparency of $D = 0.9$ and different values of the spin-mixing angle ϑ. The grey area marks the width of the bulk mean-field energy gap in the superconductor.*

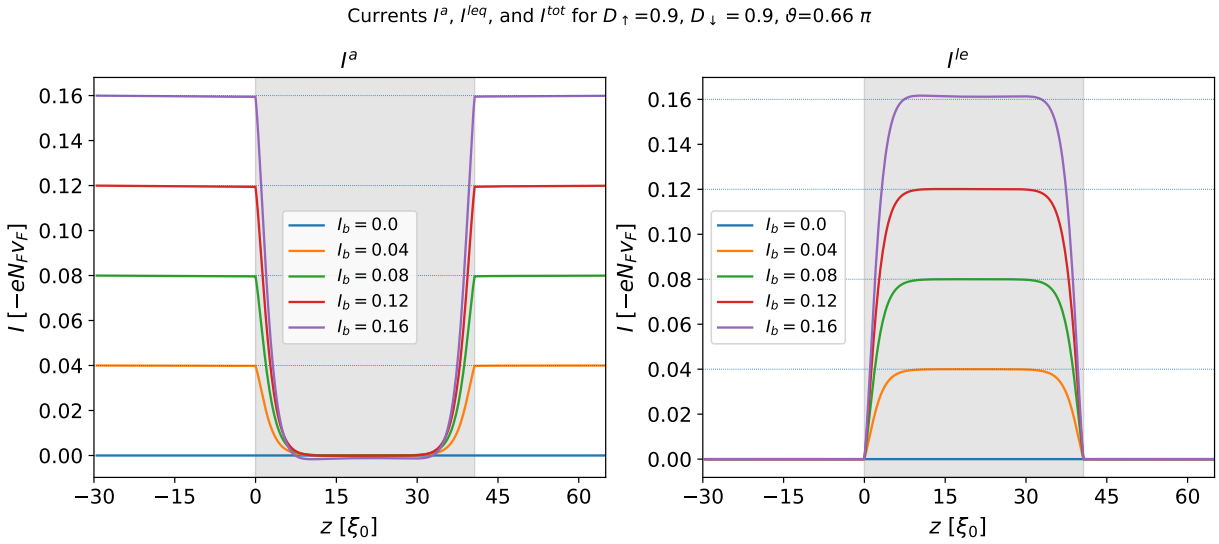

Figure 4.25: *Conversion from normal-state "anomalous" current into supercurrent over the system. The dotted lines show the respective boundary current. They grey area marks the superconducting region.*

In addition to the magnetization, the bound states also influence the charge and spin transport through the structure. The conversion length scale of quasiparticle current into supercurrent is unaffected by the presence of Andreev bound states, as can be seen in Fig. 4.25. The jump in ϕ at the interface will, however, be affected by the bound states. Fig. 4.26 shows the chemical potential for spin-degenerate transparencies of $D = 0.9$ and a rather large spin-mixing angle of $\vartheta = 0.66\ \pi$.

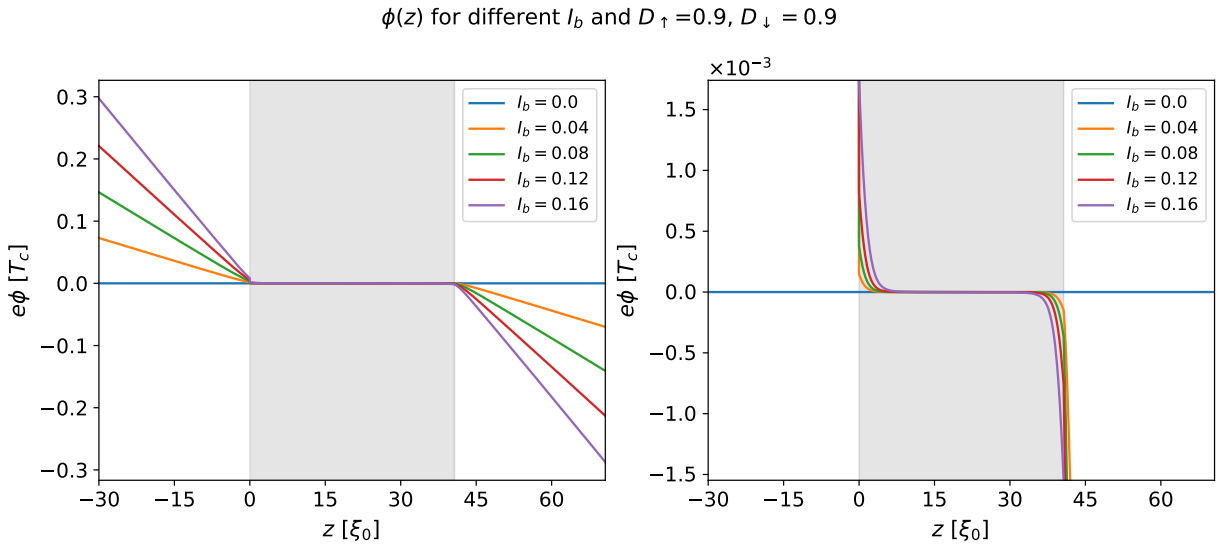

Figure 4.26: *Chemical potential $\phi(z)$ for spin-filtering in the N-SAI-S system with $D_\uparrow = D_\downarrow = 0.9$ and $\vartheta = 0.66\ \pi$. Left: $\phi(z)$ over the whole range of the system. Right: Enlargement of the central superconducting region.*

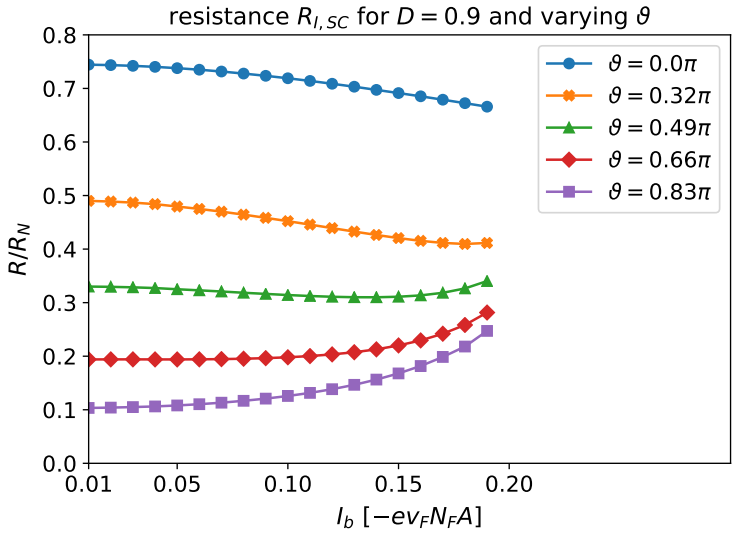

Figure 4.27: *Resistance R_I at the SAI for $D_{\uparrow,\downarrow} = 0.9$ for different spin-mixing angle ϑ and currents I.*

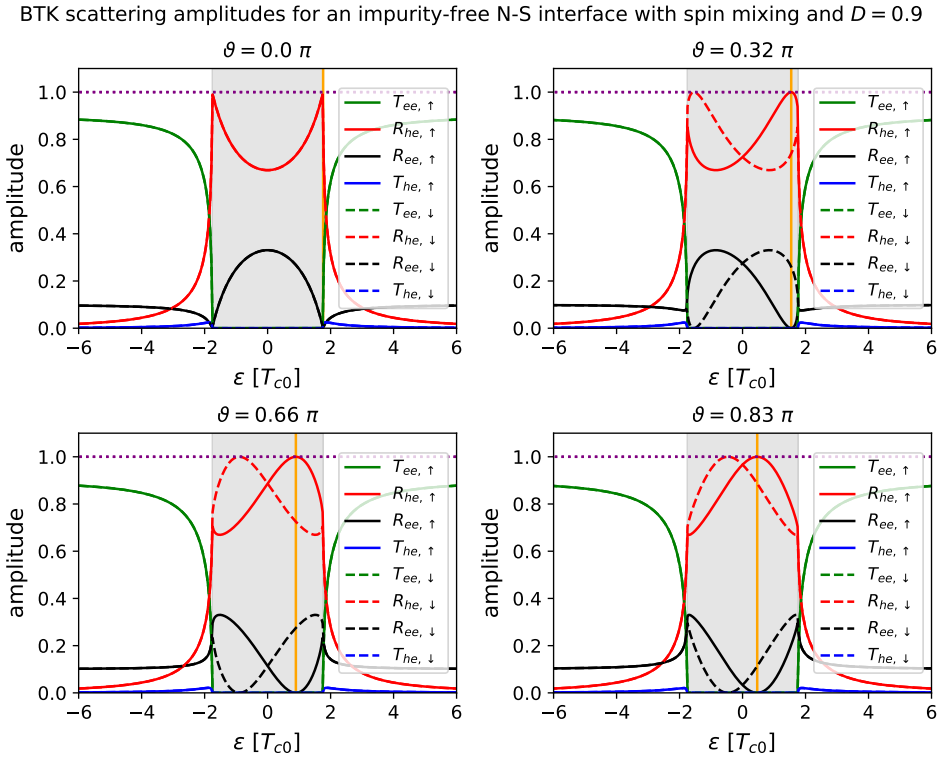

Figure 4.28: *Scattering amplitudes for a SAI with $D = 0.9$ for different spin-mixing angles. The purple-dotted line is the sum of all four amplitudes and equal to unity, ensuring probability current conservation, the orange line is the position of the ABS.*

Similiarly to the NIS system in Chap. 3, the interface resistance will again be current-dependent, shown in Fig. 4.27. We can understand this behaviour by consindering the scattering amplitudes at the SAI, seen in Fig. 4.28.

In the case of vanishing spin-mixing angle, Andreev reflection is suppressed around zero energy but increases towards the gap edge. As a result the resistance drops for larger currents where a wider energy window contributes to transport. As discussed in Sect. 4.1, the position of the ABS gets closer to zero energy for increasing spin-mixing angle and the state is not a sharp peak but spread out in energy for large transparencies. As we can see, the bound state increases the probability of Andreev reflection in an energy range where it would be suppressed for an insulating barrier, reducing the interface resistance at small currents.

The shift of R_{he} from the gap edge towards zero energy also explains the increased resistance for larger currents in this case. This is in agreement with earlier results that predicted an increased conductance for a localized ABS in the voltage-bias case[40].

We can also see in the above amplitudes that the two spin-orientations will have different transmission probabilities which leads to a finite spin current through the interface, shown in Fig. 4.29.

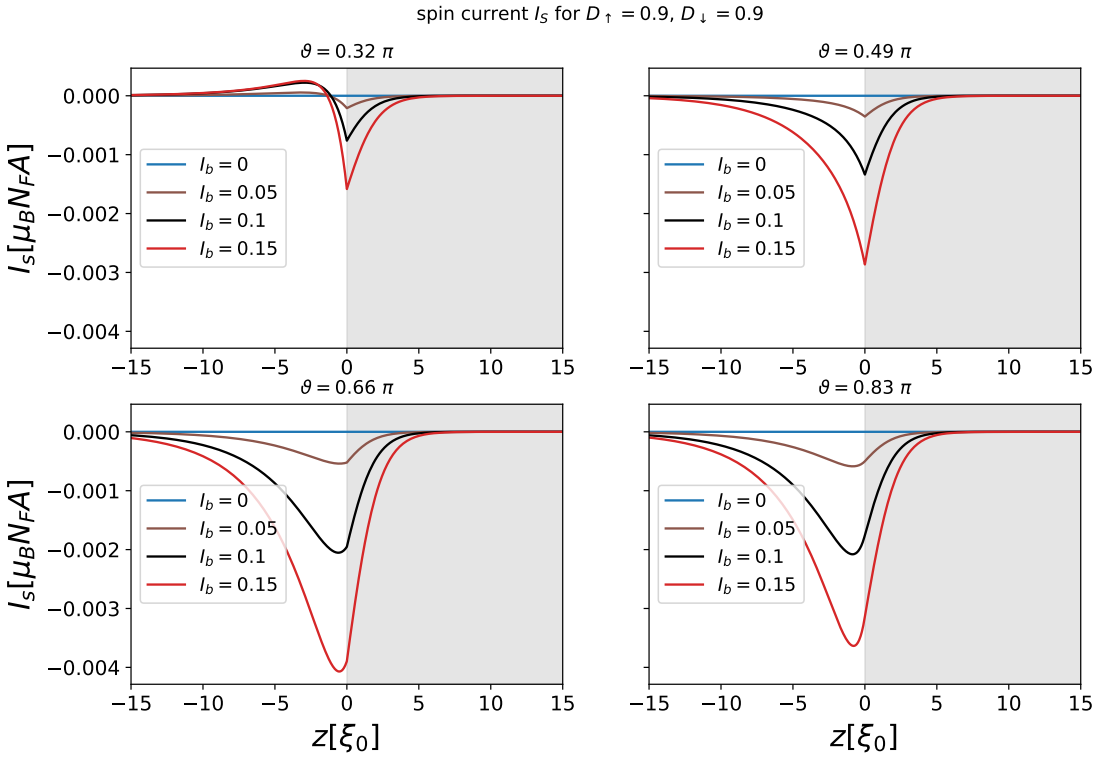

Figure 4.29: *Spin current in the NSN system with $D_\uparrow = 0.9$ and $D_\downarrow = 0.9$ for different spin-mixing angle ϑ and currents I_b. They grey area marks the superconducting region.*

For smaller transparencies the bound state peaks become more localized in energy space, as discussed earlier. Just as in the case of pure charge imbalance, this smaller transparency also leads to a larger potential jump at the interface and, for the same current, a correspondingly larger energy window participating in the transport. Fig. 4.30 shows the interface resistance as a function of applied current and spin-mixing angle for a lower transparency of $D = 0.3$.

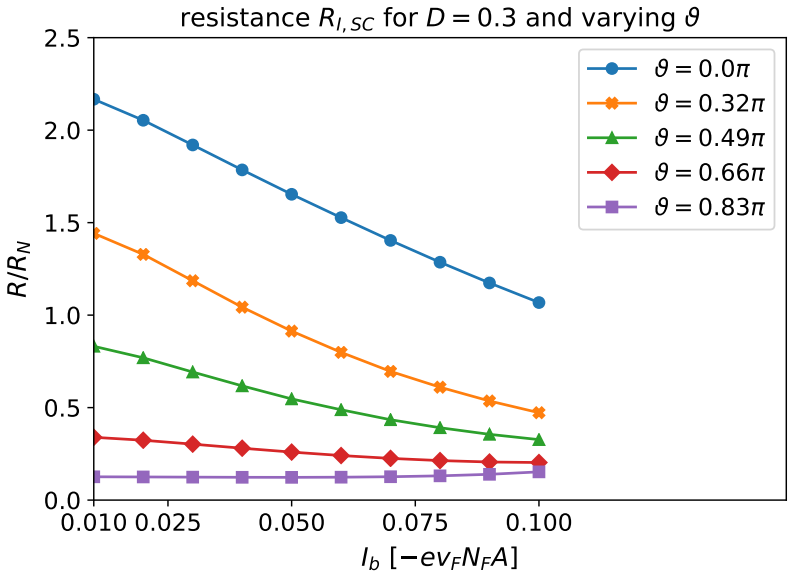

Figure 4.30: *Resistance R_I at the SAI for $D_\uparrow = D_\downarrow = 0.3$ for different spin-mixing angle ϑ and currents I.*

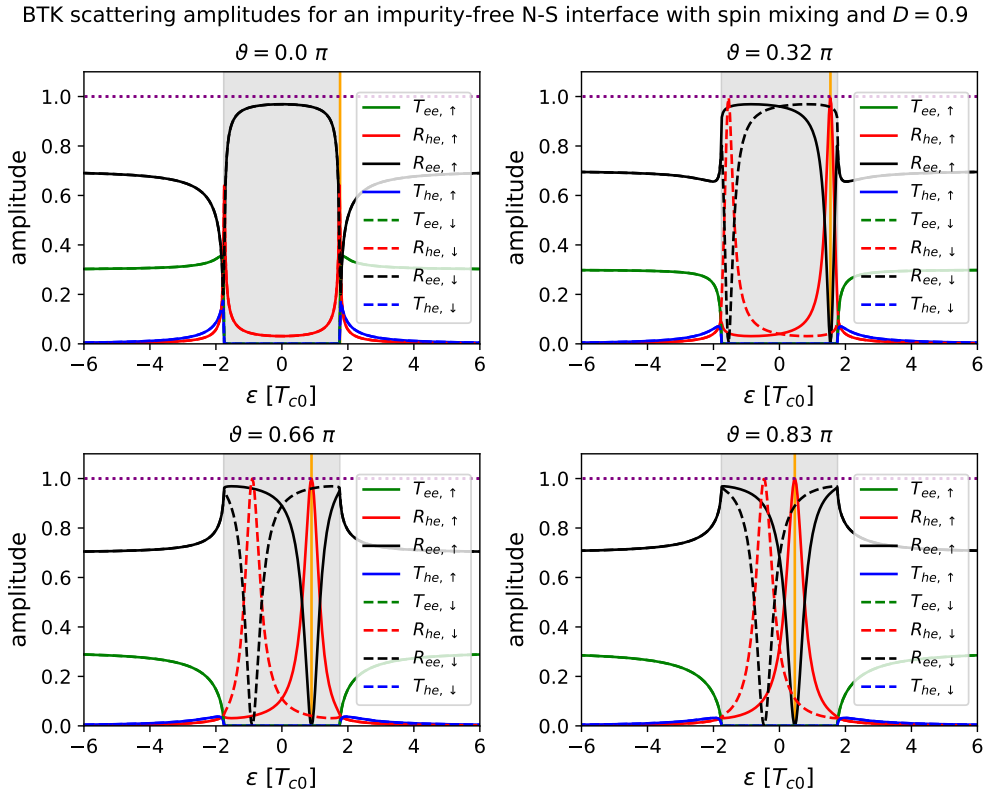

Figure 4.31: *Scattering amplitudes for a small-transparency ($D = 0.3$) SAI for different spin-mixing angles. The purple-dotted line is the sum of all four contributions which has to equal unity to ensure probability current conservation, the orange line is the position of the ABS.*

Fig. 4.31 shows the scattering amplitudes for low transparency. Similiar to the discussion for high transparency, the presence of the ABS enhances the probability of Andreev reflection in the subgap region compared to the case of no spin mixing. For vanishing or small spin mixing angle, the Andreev-refleciton probability is peaked close to or at the gap edge, leading to a decreased resistance for higher currents. For $\vartheta = 0.83\pi$, the bound-state peak is close to zero energy, resulting for a finite Andreev-refleciton amplitude over the entire subgap region. Hence, the interface resistance is strongly suppressed for a large spin-mixing angle with only a small increase towards to gap edge.

5 Conclusion & Outlook

In this thesis, we have used the quasiclassical theory of superconductivity to study transport in mesoscopic hybrid structures consisting of a superconductor connected to normal-metal leads, connected via an insulator (NIS) or a spin-active interface (N-SAI-S) of arbitrary transparency. To study such systems in nonequilibrium, we performed a fully self-consistent calculation of the superconducting order parameter and the chemical potential.

To this end, we constructed a boundary condition for the distribution function and a calculation scheme that allows to enforce a certain current in such hybrid systems with normal leads at both ends of the system. This provides a natural framework for the description of current-biased superconductors. We used this scheme to study two groups of systems. Firstly, we compared the transport in both an entirely normal-metal structure with an insulating barrier to the NIS system. Similiar studies of the NIS system, e.g. [52, 68], treat the normal leads regions as reservoirs and neglect the proximity effect. Secondly, we studied the effect of a spin-active interface in both systems.

For the NIS system, the fully self-consistent calculation allowed us to examine phenomena such as the conversion from quasiparticle current into superflow and the decay of charge imbalance in the superconductor. For large currents densities we found that injected quasiparticles lead to a "backflowing" quasiparticle current component that is overcompensated by additional supercurrent. The effect is found to be a result of the Doppler shift of quasiparticles in the presence of superflow.

The N-S interface resistance we obtain differs from the results in [28]. In comparison to their work, we relaxed the point-contact assumption and the potential boundary condition, replacing the latter with a current boundary condition. The resistances calculated in our scheme are expected to be more accesible in experiments on devices with barriers not resembling a point contact.

The effect of a spin-active interface on transport is strongly dependent on the interface parameters. Spin filtering, meaning different transmission probabilites for the two spin orientations, leads to an increase in the interface resistance. This is caused by a suppression of Andreev reflection in the subgap region. Spin mixing, i.e., the presence of a finite spin-mixing angle at the interface, is found to reduce the interface resistance. This effect is especially pronounced for low-transparency interfaces where Andreev reflection would normally be strongly suppressed. This is caused by Andreev reflection becoming enhanced in an energy range around the energy of the Andreev bound state present at such interfaces.

This work can be extended in several ways. Firstly, it would be desirable to extend the nonequilbrium framework used in this work to the full two-by-two spin structure. This is straightforward but numerically challenging. Such an extension could be used to study systems involving interfaces with a rotating magnetization, which are predicted to host spin-polarized triplet pairs[4], in nonequilbrium. As discussed in the introduction, these triplet pairs are of high relevance to superconducting spintronics. Additionally, the inclusion of the full spin structure would allow to study systems with spin-orbit coupling and would provide a path towards topological superconductors[69].

Secondly, the framework presented here could be used to study the properties of unconventional superconductors in nonequilibrium to complement the extensive studies[70, 71] on their equilibrium behaviour.

Thirdly, we have considered our systems to be much smaller that the energy-relaxation length. If such effects cannot be neglected, inelastic scattering, for example via electron-phonon coupling as discussed in [59], has to be included. This should also lead to a decay of the above-gap quasiparticle population we observed in this work.

Lastly, this work was focused on normal-metal superconductor hybrid structures in the form of a N-(I/SAI)-S-N system. The present work calculated the potential drop in such hybrid structures under current bias. Another group of systems, Josephson junctions of either S-I-S or S-N-S type, could also be studied within the quasiclassical framework presented here. In this case we would instead obtain the superconducting phase drop as function of bias current, the current-phase characteristics. This can be used to extract the kinetic inductance of a given structure, similiar to the resistances calculated in this work. An extension in that direction could be used to analyze recent experimental progress[3, 72].

Appendices

Appendix A

Derivation of the stepping formula for distribution functions

The aim of this section is to derive the explicit stepping formula for the distribution function x. The derivation is based on the concepts introduced in [38]. Note that in the following, we assume a diagonalizable structure in spin space, meaning

$$\gamma^X = \begin{pmatrix} \gamma_\uparrow^X & 0 \\ 0 & \gamma_\downarrow^X \end{pmatrix} i\sigma_2, \qquad x = \begin{pmatrix} x_\uparrow & 0 \\ 0 & x_\downarrow \end{pmatrix}. \tag{A.1}$$

The starting point is the differential equation for x, Eq. (2.34), which can be rewritten as

$$i\partial x + \left(E - \gamma\tilde{\Delta}\right)^R - x\left(E + \Delta\tilde{\gamma}\right)^A = I^K, \tag{A.2}$$

where

$$I^K \equiv \gamma^R \tilde{E}^K \tilde{\gamma}^A + \Delta^K \tilde{\gamma}^A + \gamma^R \tilde{\Delta}^K + E^K. \tag{A.3}$$

Here, and in the following, we use

$$E^R = \varepsilon - \Sigma^R, \qquad E^A = \varepsilon - \Sigma^A, \qquad E^K = -\Sigma^K.$$

The formal solution, according to [38], is then

$$x(\rho) = S_U^R(\rho, 0)x(0)\tilde{S}_V^A(0, \rho) - i\int_0^\rho S_U^R(\rho, \rho')I^K(\rho')\tilde{S}_V^A(\rho', \rho)\, d\rho'.$$

Inserting the definitions

$$S_U^X(\rho, \rho') \equiv U^X(\rho)U^X(\rho')^{-1}, \qquad S_V^X(\rho', \rho) = V^X(\rho')^{-1}V^X(\rho),$$

we obtain the formula

$$x(\rho) = U^R(\rho)\left[x(0) - i\int_0^\rho U_R(\rho')^{-1}I^K(\rho')\tilde{V}^A(\rho')^{-1}\, d\rho'\right]\tilde{V}^A(\rho). \tag{A.4}$$

We now focus on the integral in this expression, and skip writing out the argument ρ' in the following . Putting in the definition of I^K we obtain

$$\int_0^\rho d\rho'(U^R)^{-1}I^K(\tilde{V}^A)^{-1} = \int_0^\rho d\rho'(U^R)^{-1}(\underbrace{\gamma^R\tilde{E}^K\tilde{\gamma}^A}_{=a} + \underbrace{\Delta^K\tilde{\gamma}^A}_{=b} + \underbrace{\gamma^R\tilde{\Delta}^K}_{=c} + \underbrace{E^K}_{=d})(\tilde{V}^A)^{-1}, \quad \text{(A.5)}$$

We can treat the four marked terms $a-d$, which we understand to include the outer operators $(U^R)^{-1}$ and $(\tilde{V}^A)^{-1}$, separately. To do this, we make use of the formula for γ in terms of U and V operators, Eq. (2.115). We find

a)
$$\int_0^\rho d\rho'(U^R)^{-1}\Big(\gamma_0^R + U^R\delta_i^R V_0^R\Big)\tilde{E}^K\Big(\tilde{\gamma}_0^A + \tilde{U}_0^A\tilde{\delta}_i^A\tilde{V}^A\Big)(\tilde{V}^A)^{-1}$$
$$= \int_0^\rho d\rho \underline{(U^R)^{-1}\gamma_0^R\tilde{E}^K\tilde{\gamma}_0^A(\tilde{V}^A)^{-1}} + \underdot{\delta_i^R V_0^R\tilde{E}^K\tilde{\gamma}_0^A(\tilde{V}^A)^{-1}}$$
$$+ \underline{(U^R)^{-1}\gamma_0^R\tilde{E}^K\tilde{U}_0^A\tilde{\delta}_i^A} + \underwave{\delta_i^R V_0^R\tilde{E}^K\tilde{U}_0^A\tilde{\delta}_i^A}$$

b)
$$\int_0^\rho d\rho'(U^R)^{-1}\Delta^K\Big(\tilde{\gamma}_0^A + \tilde{U}_0^A\tilde{\delta}_i^A\tilde{V}^A\Big)(\tilde{V}^A)^{-1} = \int_0^\rho d\rho' \underline{(U^R)^{-1}\Delta^K\tilde{\gamma}_0^A(\tilde{V}^A)^{-1}} + \underline{(U^R)^{-1}\Delta^K\tilde{U}_0^A\tilde{\delta}_i^A}$$

c)
$$\int_0^\rho d\rho'(U^R)^{-1}\Big(\gamma_0^R + U^R\delta_i^R V_0^R\Big)\tilde{\Delta}^K(\tilde{V}^A)^{-1} = \int_0^\rho d\rho' \underline{(U^R)^{-1}\gamma_0^R\tilde{\Delta}^K(\tilde{V}^A)^{-1}} + \underdot{\delta_i^R V_0^R\tilde{\Delta}^K(\tilde{V}^A)^{-1}}$$

d)
$$\int_0^\rho d\rho' \underline{(U^R)^{-1}E^K(\tilde{V}^A)^{-1}}$$

Next, we recombine terms from each of those four parts. Adding up the first term of each a to d (underlined in a - d) gives

$$\int_0^\rho d\rho'(U^R)^{-1}\Big(\gamma_0^R\tilde{E}^K\tilde{\gamma}_0^A + \Delta^K\tilde{\gamma}_0^A + \gamma_0^R\tilde{\Delta}^K + E^K\Big)(\tilde{V}^A)^{-1} \equiv \int_0^\rho d\rho'(U^R)^{-1}I_0^K(\tilde{V}^A)^{-1}. \quad \text{(A.6)}$$

which defines

$$I_0^K \equiv \gamma_0^R\tilde{E}^K\tilde{\gamma}_0^A + \Delta^K\tilde{\gamma}_0^A + \gamma_0^R\tilde{\Delta}^K + E^K, \quad \text{(A.7)}$$

in analogy to Eq. (A.3). All terms including either δ_i^R (dotted lines in a - d) or $\tilde{\delta}_i^A$ (dashed line in a - d) are

$$\int_0^\rho d\rho'\delta_i^R V_0^R\tilde{E}^K\tilde{\gamma}_0^A(\tilde{V}^A)^{-1} + \delta_i^R V_0^R\tilde{\Delta}^K(\tilde{V}^A)^{-1}, \quad \text{(A.8)}$$

and

$$\int_0^\rho d\rho'(U^R)^{-1}\gamma_0^R\tilde{E}^K\tilde{U}_0^A\tilde{\delta}_i^A + (U^R)^{-1}\Delta^K\tilde{U}_0^A\tilde{\delta}_i^A, \quad \text{(A.9)}$$

and the term including both δ_i^R and $\tilde{\delta}_i^A$ (wiggly line in a - d) is

$$\int_0^\rho d\rho' \delta_i^R V_0^R \tilde{E}^K \tilde{U}_0^A \tilde{\delta}_i^A. \tag{A.10}$$

Next, we invert the formulas [reference above formulas for U^R and $\tilde{V}^A$ to find

$$(U^R(\rho))^{-1} \equiv \left(\mathbb{1} + \delta_i^R W_0^R(\rho)\right) (U_0^R(\rho))^{-1}, \tag{A.11}$$

$$(\tilde{V}^A(\rho))^{-1} \equiv (\tilde{V}_0^A(\rho))^{-1} \left(\mathbb{1} + \tilde{W}_0^A(\rho)\tilde{\delta}_i^A\right). \tag{A.12}$$

Once we insert these two expressions into the formulas Eq. (A.6) - (A.10), all integrals only depend on the known quantities U_0^X, V_0^X, and W_0^X and can be taken analytically. For illlustration, we calculate the term in Eq. (A.6) explicitly. We find

$$\begin{aligned}\int_0^\rho d\rho' (U^R)^{-1} I_0^K (\tilde{V}^A)^{-1} = &\int_0^\rho d\rho' (U_0^R)^{-1} I_0^K (\tilde{V}_0^A)^{-1} + \delta_i^R \int_0^\rho d\rho' W_0^R (U_0^R)^{-1} I_0^K (\tilde{V}_0^A)^{-1} \tilde{W}_0^A \tilde{\delta}_i^A \\ &+ \delta_i^R \int_0^\rho d\rho' W_0^R (U_0^R)^{-1} I_0^K (\tilde{V}_0^A)^{-1} + \int_0^\rho d\rho' (U_0^R)^{-1} I_0^K (\tilde{V}_0^A)^{-1} \tilde{W}_0^A \tilde{\delta}_i^A.\end{aligned}$$

We now insert the definitions for the operators U, V and W. Assuming that both γ_0 and Δ can be written in a diagonal spin-structure, e.g.,

$$\gamma_0^X = \begin{pmatrix} \gamma_{0,\uparrow}^X & 0 \\ 0 & \gamma_{0,\downarrow}^X \end{pmatrix} i\sigma_2, \tag{A.13}$$

the operators U_0, V_0, and I_0^K become diagonal. Whenever we swap the place of any diagonal matrix with a term containing $i\sigma_2$, such as W_0, the diagonal elements of the matrix (in spin-space) get swapped. We can then swap all matrices around to form one of four different matrix exponentials

$$e^{-i\underline{\underline{\beta_i}}\rho} \equiv \begin{pmatrix} e^{-i\beta_{j,\uparrow}\rho} & 0 \\ 0 & e^{-i\beta_{j,\downarrow}\rho} \end{pmatrix}, \tag{A.14}$$

with the coefficients

$$\beta_{1,\sigma} \equiv E_\sigma^R - E_\sigma^A + \gamma_\sigma^R \tilde{\Delta}_{\underline{\sigma}}^R + \tilde{\gamma}_{\underline{\sigma}}^A \Delta_\sigma^A, \tag{A.15}$$

$$\beta_{2,\sigma} \equiv \tilde{E}_\sigma^R - \tilde{E}_{\underline{\sigma}}^A - \gamma_\sigma^R \tilde{\Delta}_{\underline{\sigma}}^R - \tilde{\gamma}_{\underline{\sigma}}^A \Delta_\sigma^A, \tag{A.16}$$

$$\beta_{3,\sigma} \equiv \tilde{E}_{\underline{\sigma}}^R - E_\sigma^A - \gamma_\sigma^R \tilde{\Delta}_{\underline{\sigma}}^R + \tilde{\gamma}_{\underline{\sigma}}^A \Delta_\sigma^A, \tag{A.17}$$

$$\beta_{4,\sigma} \equiv E_\sigma^R - \tilde{E}_{\underline{\sigma}}^A + \gamma_\sigma^R \tilde{\Delta}_{\underline{\sigma}}^R - \tilde{\gamma}_{\underline{\sigma}}^A \Delta_\sigma^A. \tag{A.18}$$

Here, a $\underline{\sigma}$ indicates a spin-flip, i.e., $\underline{\uparrow} = \downarrow$. Once integrated, the exponential function in Eq. (A.14) gives

$$\frac{1 - e^{-i\underline{\underline{\beta_i}}\rho}}{i\underline{\underline{\beta_i}}}, \tag{A.19}$$

where the fraction is to be understood as matrix inversion. Using this, we find the final formula

$$
\begin{aligned}
x(\rho) = U^R(\rho)\Bigg[& x(0) - \frac{1 - e^{-i\underline{\underline{\beta}}_1\rho}}{\underline{\underline{\beta}}_1}\Big(\mathbb{1} - \delta^R\tilde{\Delta}^R\mathcal{D}^R\Big)I_0^K\Big(\mathbb{1} - \tilde{\mathcal{D}}^A\Delta^A\tilde{\delta}^A\Big) \\
& - \frac{1 - e^{-i\underline{\underline{\beta}}_2\rho}}{\underline{\underline{\beta}}_2}\delta^R\Big(\tilde{\Delta}^R\mathcal{D}^R I_0^K\tilde{\mathcal{D}}^A\Delta^A + \tilde{\Delta}^R\mathcal{D}^R\Big(\gamma_0^R\tilde{E}^K + \Delta^K\Big) + \Big(\tilde{E}^K\tilde{\gamma}_0^A + \tilde{\Delta}^K\Big)\tilde{\mathcal{D}}^A\Delta^A + \tilde{E}^K\Big)\tilde{\delta}^A \\
& - \frac{1 - e^{-i\underline{\underline{\beta}}_3\rho}}{\underline{\underline{\beta}}_3}\delta^R\Big(\tilde{E}^K\tilde{\gamma}_0^A + \tilde{\Delta}^K + \tilde{\Delta}^R\mathcal{D}^R I_0^K\Big)\Big(\mathbb{1} - \tilde{\mathcal{D}}^A\Delta^A\tilde{\delta}^A\Big) \\
& - \frac{1 - e^{-i\underline{\underline{\beta}}_4\rho}}{\underline{\underline{\beta}}_4}\Big(\mathbb{1} - \delta^R\tilde{\Delta}^R\mathcal{D}^R\Big)\Big(\gamma_0^R\tilde{E}^K + \Delta^K + I_0^K\tilde{\mathcal{D}}^A\Delta^A\Big)\tilde{\delta}^A\Bigg]\tilde{V}^A(\rho),
\end{aligned}
\tag{A.20}
$$

where we introduced the additional shortcut $\mathcal{D}^X$, a diagonal spin matrix with elements

$$
\mathcal{D}_\sigma^X \equiv \Big(E_\sigma^X - \tilde{E}_{\underline{\sigma}}^X + 2\gamma_\sigma^X\tilde{\Delta}_{\underline{\sigma}}^X\Big)^{-1}, \tag{A.21}
$$

originates from the prefactor of the functions W_0^X and $\tilde{W}_0^X$, respectively.

References

[1] S. Datta, "Electronic Transport in Mesoscopic Systems", Cambridge Core (1995) 10.1017/CBO9780511805776 (cit. on p. 1).

[2] *The Tunneling Transistor - Quantum tunneling is a limitation in today's transistors, but it could be the key to future devices*, [Online; accessed 8. Jan. 2020], 2013 (cit. on p. 1).

[3] E. Trabaldo, R. Arpaia, M. Arzeo, E. Andersson, D. Golubev, F. Lombardi, and T. Bauch, "Transport and noise properties of YBCO nanowire based nanoSQUIDs", Supercond. Sci. Technol. **32**, 073001 (2019) (cit. on pp. 1, 90).

[4] M. Eschrig, "Spin-polarized supercurrents for spintronics: a review of current progress", Rep. Prog. Phys. **78**, 104501 (2015) (cit. on pp. 1, 6, 63, 90).

[5] H. K. Onnes, "The resistance of pure mercury at helium temperatures", Commun. Phys. Lab. Univ. Leiden **12** (1911) (cit. on p. 2).

[6] The Nobel Foundation, *The Nobel Prize in Physics 1913*, edited by T. N. Foundation, (July 2, 2019) https://www.nobelprize.org/prizes/physics/1913/summary/ (cit. on p. 2).

[7] W. Meissner and R. Ochsenfeld, "Ein neuer Effekt bei Eintritt der Supraleitfähigkeit", Naturwissenschaften **21**, 787–788 (1933) (cit. on p. 2).

[8] F. London and H. London, "The electromagnetic equations of the supraconductor", Proceedings of the Royal Society of London. Series A - Mathematical and Physical Sciences, [Online; accessed 17. Aug. 2019] (1935) 10.1098/rspa.1935.0048 (cit. on p. 2).

[9] J. Bardeen, L. N. Cooper, and J. R. Schrieffer, "Microscopic Theory of Superconductivity", Phys. Rev. **106**, 162–164 (1957) (cit. on p. 2).

[10] J. Bardeen, L. N. Cooper, and J. R. Schrieffer, "Theory of Superconductivity", Phys. Rev. **108**, 1175–1204 (1957) (cit. on p. 2).

[11] The Nobel Foundation, *The Nobel Prize in Physics 1972*, edited by T. N. Foundation, Aug. 17, 2019 (cit. on p. 3).

[12] J. G. Bednorz and K. A. Müller, "Possible highTc superconductivity in the Ba-La-Cu-O system", Z. Phys. B: Condens. Matter **64**, 189–193 (1986) (cit. on p. 3).

[13] *The Nobel Prize in Physics 1987*, [Online; accessed 25. Sep. 2019], 2019 (cit. on p. 3).

[14] M. Tinkham, *Introduction to Superconductivity*, Second Edition (Dover Publications, 1996) (cit. on pp. 3, 8, 52, 60).

[15] H. Fröhlich, "Theory of the Superconducting State. I. The Ground State at the Absolute Zero of Temperature", Phys. Rev. **79**, 845–856 (1950) (cit. on p. 3).

[16] L. N. Cooper, "Bound Electron Pairs in a Degenerate Fermi Gas", Phys. Rev. **104**, 1189–1190 (1956) (cit. on p. 3).

[17] S. Datta and B. Das, "Electronic analog of the electro-optic modulator", Appl. Phys. Lett. **56**, 665–667 (1990) (cit. on p. 5).

[18] B. D. Josephson, "Possible new effects in superconductive tunnelling", Physics Letters **1**, 251–253 (1962) (cit. on p. 6).

[19] F. S. Bergeret, A. F. Volkov, and K. B. Efetov, "Odd triplet superconductivity and related phenomena in superconductor-ferromagnet structures", Rev. Mod. Phys. **77**, 1321–1373 (2005) (cit. on p. 6).

[20] F. Hübler, M. J. Wolf, D. Beckmann, and H. V. Löhneysen, "Long-Range Spin-Polarized Quasiparticle Transport in Mesoscopic Al Superconductors with a Zeeman Splitting", Phys. Rev. Lett. **109**, 207001 (2012) (cit. on pp. 6, 7).

[21] T. S. Khaire, M. A. Khasawneh, W. P. Pratt, and N. O. Birge, "Observation of Spin-Triplet Superconductivity in Co-Based Josephson Junctions", Phys. Rev. Lett. **104**, 137002 (2010) (cit. on p. 6).

[22] W. M. Martinez, W. P. Pratt, and N. O. Birge, "Amplitude Control of the Spin-Triplet Supercurrent in $S/F/S$ Josephson Junctions", Phys. Rev. Lett. **116**, 077001 (2016) (cit. on pp. 6, 7).

[23] K. K. Likharev, "Superconductor digital electronics", Physica C: Superconductivity and its Applications **482**, 6–18 (2012) (cit. on p. 7).

[24] P. Bunyk, K. Likharev, and D. Zinoviev, "RSFQ technology: Physics and Devices", Int. J. High Speed Electron. Syst. **11**, 257–305 (2001) (cit. on pp. 1, 7).

[25] "The Next Wave", [Online; accessed 2. Oct. 2019] (2014) (cit. on p. 7).

[26] E. C. Gingrich, B. M. Niedzielski, J. A. Glick, Y. Wang, D. L. Miller, R. Loloee, P. Pratt W. Jr., and N. O. Birge, "Controllable 0–π Josephson junctions containing a ferromagnetic spin valve", Nat. Phys. **12**, 564–567 (2016) (cit. on p. 7).

[27] I. M. Dayton, T. Sage, E. C. Gingrich, M. G. Loving, T. F. Ambrose, N. P. Siwak, S. Keebaugh, C. Kirby, D. L. Miller, A. Y. Herr, Q. P. Herr, and O. Naaman, "Experimental Demonstration of a Josephson Magnetic Memory Cell With a Programmable π-Junction", IEEE Magn. Lett. **9**, 1–5 (2018) (cit. on p. 7).

[28] G. E. Blonder, M. Tinkham, and T. M. Klapwijk, "Transition from metallic to tunneling regimes in superconducting microconstrictions: Excess current, charge imbalance, and supercurrent conversion", Phys. Rev. B **25**, 4515–4532 (1982) (cit. on pp. 8, 23, 43, 45–47, 61, 89).

[29] Y. V. Sharvin, "A Possible Method for Studying Fermi Surfaces", Journal of Experimental and Theoretical Physics **48**, [Online; accessed 4. Jan. 2020] (1964) (cit. on p. 8).

[30] Henrik Bruus and Karsten Flensberg, *Many-Body Quantum Theory in Condensed Matter Physics - An Introduction* (Oxford Graduate Texts, Jan. 14, 2016) (cit. on pp. 11, 12).

[31] Nikolai Kopnin, *Theory of Nonequilibrium superconductivity* (Oxford Science Publications, 2001) (cit. on pp. 11, 13, 18).

[32] C. Timm, *Vielteilchentheorie kondensierter Materie (lecture notes)* (2014) (cit. on pp. 11, 12).

[33] L.V.Keldysh, "Diagram Technique for Nonequilibrium Processes", Journal of Experimental and Theoretical Physics **20**, [Online; accessed 30. Dec. 2019], 1018 (1964) (cit. on p. 11).

[34] J. Rammer and H. Smith, "Quantum field-theoretical methods in transport theory of metals", Rev. Mod. Phys. **58**, 323–359 (1986) (cit. on pp. 11, 12).

[35] L. Gorkov, "On the Energy Spectrum of Superconductors", Journal of Experimental and Theoretical Physics (1958) (cit. on p. 13).

[36] G. Eilenberger, "Transformation of Gorkov's equation for type II superconductors into transport-like equations", Z. Phys. A: Hadrons Nucl. **214**, 195–213 (1968) (cit. on pp. 13, 14).

[37] A. Larkin and Yu. N. Ovchinnikov, "Quasiclassical Method in the Theory of Superconductivity", Journal of Experimental and Theoretical Physics, [Online; accessed 13. Sep. 2019] (1968) (cit. on p. 13).

[38] M. Eschrig, "Scattering problem in nopnequilibrium quasiclassical theory of metals and superconductors: General boundary conditions and applications", Phys. Rev. B. **80**, 134511 (2009) (cit. on pp. 14–17, 29, 34, 93).

[39] T. Löfwander, M. Fogelström, and J. A. Sauls, "Shot noise in normal metal–d-wave superconducting junctions", Phys. Rev. B **68**, 054504 (2003) (cit. on pp. 15, 29).

[40] O. Shevtsov and T. Löfwander, "Spin imbalance in hybrid superconducting structures with spin-active interfaces", Phys. Rev. B **90**, 085432 (2014) (cit. on pp. 15, 43, 56, 64, 67, 74, 85).

[41] M. Håkansson, *Mesoscopic thin film superconductors - A computational framework* (2015) (cit. on p. 16).

[42] Matthias Eschrig, "Distribution functions in nonequilibrium theory of superconductivity and Andreev spectroscopy in unconventional superconductors", Phys. Rev. B. **61**, 9061 (2000) (cit. on p. 17).

[43] R. Grein, T. Löfwander, and M. Eschrig, "Inverse proximity effect and influence of disorder on triplet supercurrents in strongly spin-polarized ferromagnets", Phys. Rev. B **88**, 054502 (2013) (cit. on pp. 18, 38).

[44] J. W. Serene and D. Rainer, "The quasiclassical approach to superfluid 3He", Phys. Rep. **101**, 221–311 (1983) (cit. on p. 18).

[45] T. Tokuyasu, J. A. Sauls, and D. Rainer, "Proximity effect of a ferromagnetic insulator in contact with a superconductor", Phys. Rev. B **38**, 8823–8833 (1988) (cit. on pp. 21, 24).

[46] E. Zhao, T. Löfwander, and J.A. Sauls, "Nonequilibrium superconductivity near spin-active interfaces", Phys. Rev. B. **70**, 134510 (2004) (cit. on pp. 21, 23, 24, 43, 52, 64).

[47] D. Persson, O. Shevtsov, T. Löfwander, and M. Fogelström, "Spin-polarized currents and noise in normal-metal/superconductor junctions with Yu-Shiba-Rusinov impurities", Phys. Rev. B **94**, 155424 (2016) (cit. on pp. 28, 45).

[48] J. Linder, T. Yokoyama, and A. Sudbø, "Role of interface transparency and spin-dependent scattering in diffusive ferromagnet/superconductor heterostructures", Phys. Rev. B **77**, 174514 (2008) (cit. on p. 32).

[49] M. Eschrig and J. A. Sauls, "Charge dynamics of vortex cores in layered chiral triplet superconductors", New J. Phys. **11**, 075009 (2009) (cit. on p. 33).

[50] J. Clarke, "Experimental Observation of Pair-Quasiparticle Potential Difference in Nonequilibrium Superconductors", Phys. Rev. Lett. **28**, 1363–1366 (1972) (cit. on p. 33).

[51] M. Tinkham and J. Clarke, "Theory of Pair-Quasiparticle Potential Difference in Nonequilibrium Superconductors", Phys. Rev. Lett. **28**, 1366–1369 (1972) (cit. on p. 33).

[52] J. Sánchez-Cañizares and F. Sols, "Self-Consistent Theory of Transport in Quasi–One-Dimensional Superconducting Wires", J. Low Temp. Phys. **122**, 11–35 (2001) (cit. on pp. 42, 89).

[53] A.F. Andreev, "The thermal conductivity of the intermediate state in superconductors", Journal of Experimental and Theoretical Physics **19**, [Online; accessed 19. Nov. 2019] (1963) (cit. on p. 42).

[54] M. Büttiker, Y. Imry, R. Landauer, and S. Pinhas, "Generalized many-channel conductance formula with application to small rings", Phys. Rev. B **31**, 6207–6215 (1985) (cit. on p. 50).

[55] M. Büttiker, "Four-Terminal Phase-Coherent Conductance", Phys. Rev. Lett. **57**, 1761–1764 (1986) (cit. on p. 50).

[56] F. Sols and J. Sánchez-Cañizares, "Conductances in normal and normal/superconductor structures", Superlattices Microstruct. **25**, 627–638 (1999) (cit. on pp. 50, 61).

[57] W. J. Tomasch, "Geometrical Resonance in the Tunneling Characteristics of Superconducting Pb", Phys. Rev. Lett. **15**, 672–675 (1965) (cit. on p. 53).

[58] T. Wolfram, "Tomasch Oscillations in the Density of States of Superconducting Films", Phys. Rev. **170**, 481–490 (1968) (cit. on p. 53).

[59] D. Rainer and J. A. Sauls, "Strong coupling theory of superconductivity | Superconductivity: From Basic Physics to the Latest Developments", World Scientific, 45–78 (1995) (cit. on pp. 54, 90).

[60] T. Löfwander, R. Grein, and M. Eschrig, "Is CrO_2 Fully Spin Polarized? Analysis of Andreev Spectra and Excess Current", Phys. Rev. Lett. **105**, 207001 (2010) (cit. on p. 61).

[61] P. G. de Gennes and D. Saint-James, "Elementary excitations in the vicinity of a normal metal-superconducting metal contact", Physics Letters **4**, 151–152 (1963) (cit. on p. 63).

[62] A. Andreev, "Electron Spectrum of the Intermediate State of Superconductors", Journal of Experimental and Theoretical Physics **49**, [Online; accessed 7. Jan. 2020] (1965) (cit. on p. 63).

[63] T. Löfwander, V. S. Shumeiko, and G. Wendin, "Andreev bound states in high-Tc superconducting junctions", Supercond. Sci. Technol. **14**, R53–R77 (2001) (cit. on pp. 63, 64).

[64] M. Fogelström, "Josephson currents through spin-active interfaces", Phys. Rev. B **62**, 11812–11819 (2000) (cit. on p. 64).

[65] F. Hübler, M. J. Wolf, T. Scherer, D. Wang, D. Beckmann, and H. V. Löhneysen, "Observation of Andreev Bound States at Spin-active Interfaces", Phys. Rev. Lett. **109**, 087004 (2012) (cit. on p. 64).

[66] C. Richard and A. B. Vorontsov, "Heat transport in nonuniform superconductors", Phys. Rev. B **94**, 064502 (2016) (cit. on p. 72).

[67] S. Maekawa, S. O. Valenzuela, E. Saitoh, and T. Kimura, *Spin Current* (Oxford University Press, 2017) (cit. on p. 72).

[68] A. Martin and C. J. Lambert, "Self-consistent current-voltage characteristics of superconducting nanostructures", Phys. Rev. B **51**, 17999–18002 (1995) (cit. on p. 89).

[69] M. Sato and Y. Ando, "Topological superconductors: a review", Rep. Prog. Phys. **80**, 076501 (2017) (cit. on p. 90).

[70] P. Holmvall, A. B. Vorontsov, M. Fogelström, and T. Löfwander, "Broken translational symmetry at edges of high-temperature superconductors", Nat. Commun. **9**, 1–11 (2018) (cit. on p. 90).

[71] P. Holmvall, A. B. Vorontsov, M. Fogelström, and T. Löfwander, "Spontaneous symmetry breaking at surfaces of d-wave superconductors: Influence of geometry and surface ruggedness", Phys. Rev. B **99**, 184511 (2019) (cit. on p. 90).

[72] D. Niepce, J. Burnett, and J. Bylander, "High Kinetic Inductance NbN Nanowire Superinductors", Phys. Rev. Appl. **11**, 044014 (2019) (cit. on p. 90).

Acknowledgements

Last but not least, there's some people that deserve praise and my gratitude. I'd like to thank Tomas Löfwander for his supervision and patience with me and my never-ending questions. If professors got a krona for every question they have to answer ... The other seniors at AQP also deserves my thanks, be it for an open ear, randomly-timed encouraging words on the hallway exactly when you need it the most ("People are very interested in your work! " — Jaså!), or thorough questions during group talks.

Nastaran and Patric, thank you for being great officemates, listening to my complaints, and providing advice, it's been a pleasure sharing office with you. There's a long list of colleagues, past and present, that make AQP a nice and friendly place and provide countless interesting discussion topics, be it at fika breaks or during a course. Thanks to all of you!

Lastly, Jens Schulenborg deserves a shrine devoted to him at AQP for providing great thesis templates, who knows how many work hours this has saved already.